Department of Physics
University of Jyväskylä.
Research report No. 12/2015

Nuclear fission studies with the IGISOL method and JYFLTRAP

by
Dmitry Gorelov

Academic Dissertation
for the Degree of
Doctor of Philosophy

To be presented, by permission
of the Faculty of Mathematics
and Natural Sciences
of the University of Jyväskylä,
for public examination in Auditorium FYS 1
of the University of Jyväskylä
on December 22, 2015
at 12 o'clock noon

Jyväskylä, Finland
December 2015

Preface

... to my family dedicated.

About five years ago in cold winter I was warmly met at the Department of Physics in the University of Jyväskylä. Since that time I have became a member of the IGISOL team.

The present thesis is dedicated to the study of nuclear fission and includes only a part of the work, which has been carried out during the years 2010–2015 at IGISOL. Almost half of that time was occupied by construction and tuning of the IGISOL–4 facility. In addition to the experiments described in the thesis a huge variety of measurements have been done at IGISOL–4 since its commissioning. These measurements cover different research areas starting from material physics and ending up with γ-spectroscopy of radioactive nuclides. Being a member of the IGISOL team gave me a great opportunity to participate in such interesting and challenging experiments.

Some thesis results have been already published in several articles and conference proceedings and other results are going to be published soon. The list of articles is given in the introduction. This thesis combines these ideas together and presents them in connection to nuclear fission studies.

This work could not be possible without a decision made by Prof. Juha Äystö, who accepted me as a PhD student and who put me in touch with sailing. Special thank goes to Dr. Hekki Penttilä. He took the responsibilities of my supervisor and guided me through the jungles of experimental preparations and data analysis. I express my gratitude to Prof. Ari Jokinen for giving me opportunities to attend conferences and workshops. I'm very grateful to Prof. Valery Rubchenya and Prof. Konstantin Gridnev, who introduced me one day to the world of nuclear physics.

Special gratitude refers to Prof. Iain Moore for fruitful discussions on various topics related, and not related, to work, for different activities outside the laboratory and especially for a reference to "Camino", which changed all my life.

Separate thanks are addressed to Dr. Tommi Eronen and Dr. Veli Kolhinen for their deep knowledge and experience in operation and tuning the Penning trap, which they shared with me. Additionally I thank Dr. Veli Kolhinen for various help outside the laboratory and for the unique experience in ultra trail running. Thanks to Dr. Sami Rinta-Antila for useful discussions about details related to experiment preparations and for the memorable launch of a "jet rocket". I'm very grateful to Dr. Vasily Simutkin for his useful comments and advice related to the analysis of

some experimental data.

I express my gratitude to all present and past members of the IGISOL group, whom I know: Dr. Anu Kankainen, Dr. Annika Voss, Dr. Juho Rissanen, Dr. Antti Saastamoinen, Dr. Mikael Reponen, Dr. Volker Sonnenschein, Jani Hakala, Ilkka Pohjalainen, Jukka Koponen, Laeticia Caenete — for the always warm, friendly and nice atmosphere at work and out of working hours as well. Thanks to the team from the Uppsala University for an intensive cooperation and their useful help during several experimental runs.

I'm very grateful to all staff: administrative office and workshops — for friendly atmosphere, for their effective and professional support, which make the Department of Physics an excellent place for work and study.

Finally I thank my parents and brother for their patience and all kind of supports during my long period of study. I address deep gratitude to my wife María José and son Maxim, who encouraged me to go further even when my strength and motivation reached their limits.

Jyväskylä, December 2015
Dmitry Gorelov

Author

Dmitry Gorelov
Department of Physics
University of Jyväskylä
Finland

Supervisors

Dr. Heikki Penttilä
Department of Physics
University of Jyväskylä
Finland

Prof. Ari Jokinen
Department of Physics
University of Jyväskylä
Finland

Prof. Juha Äystö
Department of Physics
University of Jyväskylä
Finland

Reviewers

Dr. Pierre Delahaye
GANIL
France

Dr. Robert William Mills
Research Fellow for Nuclear Data
National Nuclear Laboratory
United Kingdom

Opponent

Prof. Andrei Andreyev
Department of Physics
University of York
United Kingdom

Abstract

Gorelov, Dmitry
Nuclear fission studies with the IGISOL method and JYFLTRAP
Jyväskylä: University of Jyvaskyla, 2015,
Department of Physics Research Report
ISBN 978-951-39-6449-8 (paper copy)
ISBN 978-951-39-6450-4 (pdf)
ISSN 0075-465X

Even though nuclear fission has been intensively studied since its discovery in 1938, there is no unique model or theory which describes all aspects of this phenomenon. Experimental measurements of nuclear fission product distributions still remains quite a challenging task for modern technologies.

In the present work nuclear fission is studied from the radioactive ion beam production point of view. Some models suggest that the neutron-induced fission can be more favorable for production of neutron-rich nuclides than the proton-induced fission.

The general idea of this thesis is to compare all aspects of both approaches in connection with the IGISOL method. A new technique to determine independent fission product yields was suggested for the comparison. This technique has been tested with the proton-induced fission of actinide targets at different energies. The independent yields of the fission of ^{232}Th induced by 25 MeV protons have been measured in this work. Although only relative independent yields can be obtained by this technique. An extraction of absolute values requires additional information such as the mass distribution. Despite this fact the technique is suitable to compare independent fission product distributions for isotopes of a specific chemical element.

To perform measurements with neutron-induced fission a neutron source and a gas cell have been made and experimentally tested. The neutron source has been designed for a proton beam with energy of 30 MeV and intensity of 100 μA. A thick Be target has been chosen to produce an intensive neutron beam. The neutron intensity has been measured by the activation method and at the 0° angle is equal to $3{\cdot}10^{10}$ neutrons/(s·sr·μA), which coincides with the simulated value and is in good agreement with other similar measurements.

The design of the gas cell has been chosen to be very similar to that for the proton-induced fission. It has quite a simple construction without any electric and radio-frequency electrodes. The gas volume of approximately 150 cm^3 provides an

evacuation time of about tens of milliseconds. Due to the low fission rate and high radiation background several collecting foils have been installed to estimate main parameters of the gas cell. Radioactive ions produced in the neutron-induced fission were implanted into these foils. Later foils have been placed at a low background station and γ-spectra have been measured by the HPGe detector.

Finally the independent fission yields for the neutron-induced fission could not be measured due to the very low radioactivity extracted from the gas cell. Main results of the work and probable further developments are discussed in the Summary.

Acknowledgements

The author thanks the rector of the University of Jyväskylä for the scholarship paid during the first year of my PhD education. The Graduate School in Particle and Nuclear Physics (GRASPANP) and the Doctoral Programme in Particle and Nuclear Physics (PANU) are acknowledged for the travel funding and possibility to participate in international schools and conferences.

The present work has been supported by the Academy of Finland under the Finnish Center of Excellence Programme 2006–2011 and 2012–2017 (Nuclear and Accelerator Based Physics Programme at JYFL), by the EU 7^{th} framework programme Fission-2010-ERINDA under the project No. 269499 and by the EU 7^{th} framework programme Fission-2013-CHANDA (project No. 605203). The work also has been done with the support of the Academy of Finland under the project 139382 ("Precision Fission Studies for Practical Needs").

Contents

1 Introduction

Since its discovery nuclear fission became widely used in various fields of science and human life. O. Hahn and F. Strassmann discovered nuclear fission in 1938. The report was published on the 6th of January 1939 [1]. Reference [2] is the English translation of that article. It is interesting to note that the Nobel prize for the discovery of a purely physical phenomenon was awarded as a chemistry prize [1].

In general, nuclear fission is a process where a heavy nucleus breaks up into two nuclei of comparable size. As a result, nuclides in the middle of the periodic system are produced. The neutron to proton ratio of resulting nuclei remains approximately the same as that of the initial system. Thus the produced isotopes have an excess of neutrons relative to the stable ones in the same mass region. These radioactive neutron-rich nuclei decay mainly by β^- decay. Hundreds of different radioactive neutron-rich species can be produced in the fission of one nuclide. This property of fission is utilized in the rare isotope beam facilities (RIB facilities) [4] for fundamental research nuclear matter.

Nuclear fission is considered into a key process in the nucleosynthesis of medium and heavy nuclei and as an important part of the description of the evolution of stars and galaxies [5, 6, 7, 8]. Therefore some astrophysical hypotheses are tightly connected to the knowledge about nuclear fission.

A classical explanation of the process was given by L. Meitner and O. Frisch [9]. They realized that due to the Coulomb repulsion two nuclei formed in fission have to acquire a total kinetic energy of about 200 MeV. This suggestion was quickly confirmed experimentally by O. Frisch [10]. Due to this huge energy release nuclear fission was immediately brought into use as an effective source of energy production. Nowadays nuclear fission data are very important for various nuclear-energy related applications.

In this thesis nuclear fission is studied from the radioactive ion beam production point of view. Information on the fission yields of neutron-rich nuclides is very important for the research programmes of rare isotope beam (RIB) facilities around the world [4] and particular for the experiments at the IGISOL facility of the Accelerator Laboratory of the University of Jyväskylä (JYFL). A detailed survey of the research conduct at the IGISOL facility was published in "An IGISOL portrait" [11, 12].

[1] Otto Hahn received the prize in December of 1945, but it was the prize of the previous year – 1944. It happenned because none of the nominations met the suitable criteria and the prize of the 1944 year was reserved until the following year [3].

Data obtained during the present work can be utilized for both further development of nuclear fission models and nuclear energy-related applications.

Radioactive beams from nuclear reactions were produced by the Ion Guide Isotope Separator On-Line (IGISOL) technique. This method developed in the early 1980s is nowadays utilized at facilities around the world. The central idea of the technique is to slow down and thermalize ions from nuclear reactions in gas. Then the ions are extracted from the gas cell and guided by a system of electrodes to a mass separator [13]. Detailed description of the evolution and developments of the IGISOL technique can be found in the paper [14].

A novel technique developed at JYFL was employed in this work to characterize the fission process of actinide targets. The uniqueness of the method consists of using a Penning trap (JYFLTRAP) as a precise mass filter. The selected ions are counted by a multichannel plate (MCP) detector, which provides a very high detection sensitivity [15]. Such a technique allows identification of identify individual nuclides by their masses rather than by decay properties. Sometimes it is possible to distinguish ground and isomeric states. In the case of long lived nuclei with low intensities the direct counting of ions can be the only way to determine the amount of nuclides produced in a nuclear reactions.

Nuclear fission is a very rich process and it has many different aspects. In the scope of the present work only proton- and neutron-induced (p- and n-induced) fission are considered within the constraints of the IGISOL technique. Definitions and terms, which are important for further reading and understanding, are given in Chapter 2. Detailed background of nuclear fission and the main characteristics of the process can be found in classic works by N. Bohr and J. A. Wheeler [16], R. Vandenbosch and J. R. Huizenga [17], and in the anthology edited by C. Wagemans [18]. The main concept of the work together with the initial assumptions are presented in the same chapter. Chapter 3 introduces the method which has been used to probe the yields of the radioactive nuclides in the p-induced fission of ^{232}Th. The experimental technique, data analysis and results of the measurements are described in this chapter. Chapter 4 is dedicated to the neutron source, which has been designed and constructed for the new IGISOL facility. This chapter contains a brief description of the source, its design and construction. An activation method has been used to test the neutron source on-line. Data obtained in this test are presented in Chapter 4. Chapter 5 summarizes the main results of the thesis and gives some possible perspectives for further research and developments related to nuclear fission and the IGISOL method at JYFL.

The main results of the work have been partially reported in the following publications:

1. **D. Gorelov**, T. Eronen, A. Jokinen, J. Hakala, A. Kankainen, P. Karvonen, V. S. Kolhinen, J. Koponen, I. D. Moore, H. Penttilä, K. Peräjärvi, I. Pohjalainen, B. Rakopoulos, J. Reinikainen, M. Reponen, S. Rinta-Antila, J. Rissanen,

V. A. Rubchenya, A. Saastamoinen, A. Solders, A. Voss and J. Äystö, Independent yields in proton-induced fission of ^{232}Th, to be submitted...

2. **D. Gorelov**, H. Penttilä, A. Al-Adili, T. Eronen, J. Hakala, A. Jokinen, A. Kankainen, V.S. Kolhinen, J. Koponen, M. Lantz, A. Mattera, I.D. Moore, I. Pohjalainen, S. Pomp, V. Rakopoulos, J. Reinikainen, S. Rinta-Antila, V.A. Rubchenya, V. Simutkin, A. Solders, A. Voss and J. Äystö, Developments for neutron-induced fission at IGISOL–4, submitted to Nuclear Instruments and Methods B Proceedings.

3. H. Penttilä, **D. Gorelov**, V-V. Elomaa, T. Eronen, U. Hager, J. Hakala, A. Jokinen, A. Kankainen, P. Karvonen, I.D. Moore, J. Parkkonen, K. Perjrvi, I. Pohjalainen, S. Rahaman, S. Rinta-Antila, J. Rissanen, V.A. Rubchenya, A. Saastamoinen, V. Simutkin, T. Sonoda, C. Weber and J. Äystö, Independent isotopic yields in 25 MeV and 50 MeV proton-induced fission of ^{nat}U, submitted to European Physical Journal A.

4. H. Penttilä, **D. Gorelov**, V-V. Elomaa, T. Eronen, J. Hakala, A. Jokinen, A. Kankainen, P. Karvonen, M. Lantz, A. Mattera, I.D. Moore, J. Parkkonen, S. Pomp, S. Rahaman, S. Rinta-Antila, J. Rissanen, V.A. Rubchenya, I. Ryzhov, V. Simutkin, T. Sonoda and J. Äystö, Independent isotopic product yields in 25 MeV and 50 MeV charged particle induced fission of ^{238}U and ^{232}Th, Nuclear Data Sheets 119 (2014) 334.
doi: 10.1016/j.nds.2014.08.092

5. H. Penttilä, J. Äystö, V.-V. Elomaa, T. Eronen, **D. Gorelov**, U. Hager, J. Hakala, A. Jokinen, A. Kankainen, P. Karvonen, T. Kessler, I.D. Moore, S. Rahaman, S. Rinta-Antila, V. Rubchenya and T. Sonoda, Independent fission yields with JYFLTRAP, European Physical Journal Special Topics 150 (2007) 317–318.
doi: 10.1140/epjst/e2007-00335-0

6. **D. Gorelov**, T. Eronen, J. Hakala, A. Jokinen, A. Kankainen, V.S. Kolhinen, M. Lantz, A. Mattera, I.D. Moore, H. Penttilä, I. Pohjalainen, S. Pomp, M. Reponen, S. Rinta-Antila, V.A. Rubchenya, A. Saastamoinen, V. Simutkin, A. Solders, V. Sonnenschein, and J. Äystö, Measuring independent yields of fission products using a penning trap, Bull. Rus. Acad. of Sci.: Phys. 79 (2015) 869-871.
doi: 10.3103/S1062873815070114
(Original Russian text: D. Gorelov et al., published in Izvestiya Rossiiskoi Akademii Nauk. Seriya Fizicheskaya, 2015, Vol. 79, No. 7, pp. 963966.)

7. M. Lantz, **D. Gorelov**, A. Mattera, H. Penttilä, S. Pomp, D. Rados and I. Ryzhov, Design of a neutron converter for fission studies at the IGISOL facility, Physica Scripta T150 (2012) 014020.
doi: 10.1088/0031-8949/2012/T150/014020

8. T. Eronen, V.S. Kolhinen, V.-V. Elomaa, **D. Gorelov**, U. Hager, J. Hakala, A. Jokinen, A. Kankainen, P. Karvonen, S. Kopecky, I.D. Moore, H. Penttilä, S. Ra-

haman, S. Rinta-Antila, J. Rissanen, A. Saastamoinen, J. Szerypo, C. Weber and J. Äystö, JYFLTRAP: a Penning trap for precision mass spectroscopy and isobaric purification, European Physical Journal A 48 (2012) 46.
doi: 10.1140/epja/i2012-12046-1

9. A. Al-Adili, K. Jansson, M. Lantz, A. Solders, **D. Gorelov**, C. Gustavsson, A. Mattera, I.D. Moore, A.V. Prokofiev, V. Rakopoulos, H. Penttilä, D. Tarrio, S. Wiberg, M. Österlund and S. Pomp, Simulations of the fission-product stopping efficiency in IGISOL, European Physical Journal A 51 (2015) 59.
doi: 10.1140/epja/i2015-15059-2

10. **D. Gorelov**, J. Hakala, A. Jokinen, V.S. Kolhinen, J. Koponen, I.D. Moore, H. Penttilä, I. Pohjalainen, M. Reponen, S. Rinta-Antila, V. Sonnenschein, A. Voss, A. Al-Adili, M. Lantz, A. Mattera, S. Pomp, V. Rakopoulos, V. Simutkin, A. Solders and J. Äystö, Isomeric yield ratios of fission products measured with the JYFLTRAP, Acta Phys. Pol. B 45 (2014) 211.
doi: 10.5506/APhysPolB.45.211

2 Nuclear Fission studies with the IGISOL method

2.1 Nuclear fission

The fission of a nucleus is an extremely complex phenomenon. Right after the discovery of nuclear fission N. Bohr and J. Wheeler proposed a theoretical description of the process [16]. A fissile nucleus is considered as an incompressible liquid drop with uniformly distributed electrical charge over the volume. In the liquid drop model (LDM) the total energy of a nucleus consists of three components:

$$E = E_{vol} + E_{surf} + E_{Coul}, \tag{2.1}$$

where E_{vol} is a volume energy, E_{surf} is a surface energy and E_{Coul} is a Coulomb energy.

The excitation energy of the nucleus induces deformations of the spherical shape. Due to the incompressibility assumption the volume energy E_{vol} remains the same for the deformed and spherical nucleus. At small deformations the surface tension of nuclear matter compensates the Coulomb repulsion of protons. In this case the deformation potential energy can be defined as a difference of the surface and Coulomb terms between deformed and spherical shapes:

$$E_{def}(\alpha) = E_{surf}(\alpha) + E_{Coul}(\alpha) - E_{surf}(0) - E_{Coul}(0), \tag{2.2}$$

where α is a parameter of arbitrary deformation and $E_{Coul}(0), E_{surf}(0)$ are the Coulomb and surface energies of a spherical nucleus, respectively.

Qualitatively the dependence of the potential energy on the arbitrary deformation is shown in figure 2.1. The solid line represents a typical potential energy of the charged liquid drop. In the case of small deformations the surface energy increases faster than the Coulomb energy decreases and tends to preserve spherical shape of the compound nucleus. When the deformation is large enough the interplay of surface tension and the Coulomb force tends to divide the compound nucleus and leads the system to a scission point. At the scission point the two fragments are separated one from each other. The saddle point corresponds to the critical deformation of unstable equilibrium. At this point a compound system can decay via fission process or return to the ground state emitting neutrons or γ-rays.

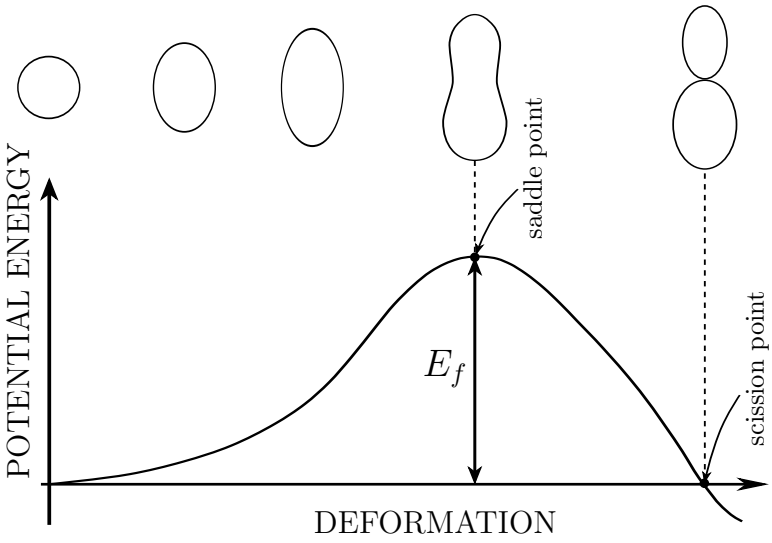

Figure 2.1: Schematic illustration of the fission barrier and the evaluation of the compound nucleus from spherical shape to scission point.

A fissility parameter $x = \Delta E_{Coul}/\Delta E_{surf}$ represents stability of a spherical nucleus against fission. According to the liquid drop model an atomic nuclei with the fissility parameter $x \geqslant 1$ can not exist in nature since they would immediately decay via spontaneous fission.

For small axially symmetric deformations from the spherical shape the radius vector can be written as an expansion of Legendre polynomials:

$$R(\theta) = R_0 \left[1 + \sum_{n=1}^{\infty} \alpha_n P_n(cos\theta) \right]. \tag{2.3}$$

Taking into account only the largest term on quadrupole deformation α_2 the fissility parameter will be

$$x = \frac{E_{Coul}(0)}{2E_{surf}(0)}. \tag{2.4}$$

Details of the mathematical transformations can be found in [19].

The simplified version of the Weizsäcker's semi-empirical mass formula offered by Bethe [20] gives the following expressions for the Coulomb and surface terms of the

total energy for a spherical nucleus[1]:

$$E_{Coul}(0) = \frac{3e^2}{5r_0}\frac{Z^2}{A^{1/3}} \qquad \text{and} \qquad E_{surf}(0) = \gamma A^{2/3}, \tag{2.5}$$

where $r_0 = 1.4$ fm, $\gamma = 14$ MeV and in cgs system units $e^2 = 1.44$ MeV·fm [16]. Finally the fissility parameter x yields

$$x = \frac{3e^2}{10r_0\gamma}\frac{Z^2}{A}. \tag{2.6}$$

From equation 2.6 it is possible to calculate the critical ratio $(Z^2/A)_{limit} \approx 45.4$. For example, the fissility parameter of the $^{239}_{92}$U nucleus is about 0.78, which is quite close to the critical value.

An important characteristic of the compound nucleus system is the fission barrier. The fission barrier height is a difference of the potential energy of deformed nucleus at the saddle point and spherical nucleus. In figure 2.1 E_f denotes the height of the fission barrier. More detailed description of the compound nucleus deformation allows development of an expression for the fission barrier height [16]:

$$E_f \approx \frac{98}{135}\gamma A^{2/3}(1-x)^3. \tag{2.7}$$

Numerical value of the fission barrier for $^{239}_{92}$U compound nucleus equals $E_f \approx 4.2$ MeV. The experimentally determined fission barrier of $^{239}_{92}$U compound nucleus is 6.34 MeV [22, 23].

According to classical mechanics a compound nucleus system can overcome the fission barrier if excitation energy is larger than the barrier height. In quantum mechanics there is non-szero probability to penetrate the barrier. This probability defines the lifetime of a nucleus against spontaneous fission from the ground state. Bohr and Wheeler in [16] estimated the lifetime against spontaneous fission and got about $\sim 10^{22}$ years, that exceeds the experimental value of $\sim 10^{16}$ years for $^{238}_{92}$U [24, 5].

The simple liquid drop model describes the general properties of the nuclear fission for actinide nuclei relatively well. Despite this success the liquid drop model has several contradictions to the experimental observations. The model predicts spherical shape for all nuclei in the ground state. Neither asymmetric mass division of fission fragments can be explained by the liquid drop model. These effects can be explained using the microscopic nuclear structure. The macroscopic liquid drop model and microscopic properties of the nucleus were combined by Strutinsky in his method of "shell corrections" [25].

[1] The original Weizsäcker's formula of the total energy of atomic nucleus can be found in reference [21].

The microscopic effects in the "shell correction" method are considered as a small deviations from the liquid drop model energy:

$$E = E_{LDM} + \sum_{p,n}(\delta U + P), \tag{2.8}$$

where P is a residual interaction and δU represents the "shell correction". The "shell correction" in Strutinsky's method is defined as a difference of the discrete single-particle energies E_ν summed over all occupied states ν and the energy of continuously distributed nucleon states up to chemical potential $\tilde{\lambda}$ with :

$$\delta U = U - \tilde{U}, \tag{2.9}$$

where energies for discrete states and continuous level distribution $\tilde{g}(E)$ are respectively:

$$U = \sum_{\nu} 2n_\nu E_\nu \qquad \text{and} \qquad \tilde{U} = 2\int_{-\infty}^{\tilde{\lambda}} E\tilde{g}(E)dE. \tag{2.10}$$

The "shell correction" can change the liquid drop fission barrier in such way that the shape of a nucleus in the ground state becomes deformed. The first minimum (I) in figure 2.2 corresponds to the ground state. Also the second minimum (II) can

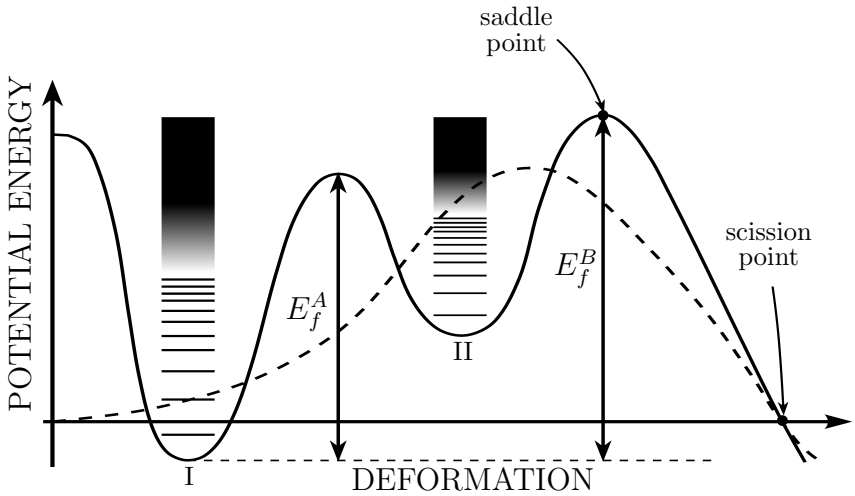

Figure 2.2: Schematic illustration of the fission barrier with "shell correction". Dashed line represents the liquid drop fission barrier.

be formed due to strong shell effects in the compound system. The presence of the

second minimum explains the existence of the spontaneous fission isomers discovered in 1962 [26, 27]. The double-humped structure of the fission barrier affects the evolution of the system towards saddle point. Experimentally it can be seen in the energy dependence of cross-sections for fission induced by nuclear reactions.

Larger deformation leads to the compound system from the saddle point to the scission point (see figures 2.1 and 2.2). In binary fission two fragments are formed nearby the scission point. Three fragments can also be produced in one fission event. It is called the ternary fission. The probability of ternary fission is significantly less than that of binary fission. It accounts for several light charged particles per thousand binary fissions, see [17, 18] and references therein. Thus in the thesis only binary fission is considered.

A distinctive feature of nuclear fission is that the combination of fission fragments is not unique after scission point although the initial conditions of the fissile system are the same. This means that the main parameters of fission fragments, such as masses, charges, kinetic and excitation energies etc., are distributed around certain values. Probably this happens because nuclear fission is a dynamical process wherein individual and collective motions of nucleons strongly influence each other.

The mechanism of fission fragment formation is a very complex process and it is still far from a detailed understanding. For better consideration it is useful to describe the time scale of nuclear fission. Figure 2.3 demonstrates the time evolution of the compound system after it has passed the outer saddle point. The given time

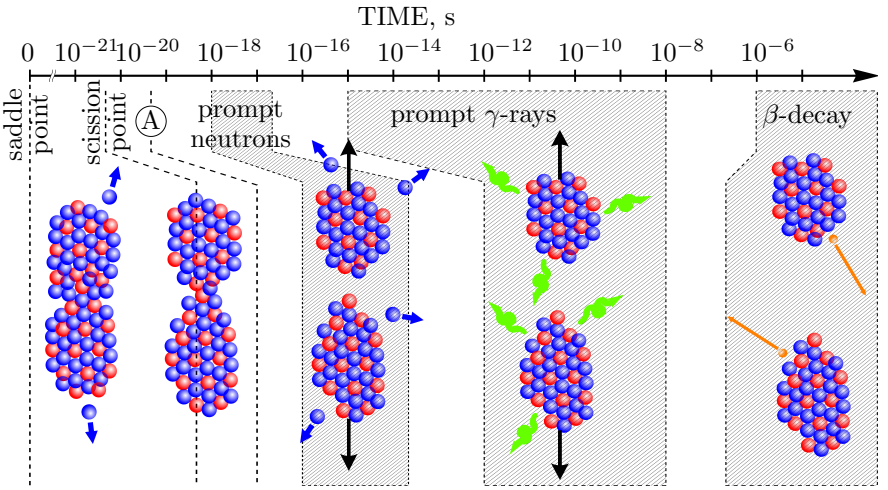

Figure 2.3: Time scale of nuclear fission. Point "A" defines the moment when the fission fragments have been accelerated up to 98 % of their total kinetic energy.

intervals are estimations that in addition to experimental observations have to rely on models and various assumptions. Details can be found in reference [28].

It is possible to see, that the fragments are formed during a relatively short time, less than about 10^{-20} s, when the system descends from the saddle to the scission point. At the scission point primary fission fragments are formed. According to [17] the term ***primary fission fragments*** means that the nuclear species formed have yet to emit any prompt neutrons. After less than 10^{-19} s both fragments are accelerated up to 98 % of their total kinetic energy. These highly excited primary fission fragments evaporate prompt neutrons and emit prompt γ-rays. After prompt de-excitation these fragments are referred to as ***primary fission products***. When at least one β-decay occurs then the primary fission products become ***secondary fission products***. In general primary or secondary fission products or their combination are named ***fission products***. Fission products are mostly β-active and in some cases the β-decay is accompanied by the so-called ***delayed neutron emission***.

The primary fission fragment distributions differ from the fission product distributions due to emission of neutrons and photons. The Coulomb barrier prevents emission of charged particles from the excited nucleus. Thus the probability for protons or another charged particles to be evaporated is significantly less than that for neutrons. This means that the charge distribution practically doesn't change during de-excitation of primary fission fragments. All in all, it is possible to say that the charge distribution reaches the equilibrium state faster than the mass distribution.

It is useful to mention here several general properties of the charge distribution. As proposed by Wahl in [29] the nuclear charge distribution of fission fragments for fixed isobaric chain A can be approximated by a Gaussian function:

$$\tilde{p}(Z)|_A = \frac{1}{\sqrt{2\pi\sigma_Z^2(A)}} exp\left[-\frac{(Z(A)-\bar{Z}(A))^2}{2\sigma_Z^2(A)}\right], \tag{2.11}$$

where $\bar{Z}(A)$ is the average charge and $\sigma_Z(A)$ is the dispersion. $\tilde{p}(Z)|_A$ represents smoothed charge distribution which is moderated by an odd-even effect. Due to this effect the yields of even charge numbers are enhanced compare to odd ones. The dispersion $\sigma_Z(A)$ is insensitive to the excitation energy of the compound nucleus for energies less than about 40 MeV [17, 30].

According to the "unchanged charge distribution" (UCD) [31] a primary fission fragment with mass number A should have the charge $Z_{UCD} = A \cdot Z_{CN}/A_{CN}$. The pair (A_{CN}, Z_{CN}) refers to the fissile system at the scission point. The charge deviation ΔZ is defined as:

$$\Delta Z = (\bar{Z} - Z_{UCD})_H = (Z_{UCD} - \bar{Z})_L, \tag{2.12}$$

where indexes H and L designate the heavy and light fragments, respectively. Usually the absolute value of the charge deviation does not exceed 1 unit $|\Delta Z| \leqslant 1$.

The parameter $\sigma_Z^2(A)$ of the continuous distribution slightly differs from the dispersion $\sigma^2(Z)|_A$ of the discrete charge distribution due to data binning that can be corrected using Sheppard's correction [32]:

$$\sigma^2(Z)|_A = \sigma_Z^2(A) + \frac{1}{12}, \tag{2.13}$$

where

$$\sigma^2(Z)|_A = \langle \{Z(A) - \bar{Z}(A)\}^2 \rangle. \tag{2.14}$$

In the same way as the charge distributions, the isotopic distributions of the primary fission fragments for a given element Z can be approximated by a Gaussian function. The isotopic mass dispersion can be written:

$$\sigma^2(A)|_Z = \langle \{A(Z) - \bar{A}(Z)\}^2 \rangle. \tag{2.15}$$

In [33] it was shown that with some assumptions the ratio of these dispersions equals to the square of the mass to charge ratio of the compound nucleus:

$$\frac{\sigma^2(A)|_Z}{\sigma^2(Z)|_A} = \left(\frac{A_{CN}}{Z_{CN}}\right)^2. \tag{2.16}$$

The most important characteristic of the nuclear fission is the mass distribution. The fission process is accompanied by a neutron emission, which influences on the final mass distributions. Experimental measurements and model estimations, for example [34, 35, 36], demonstrated that about 80–90 % of all neutrons are emitted from accelerated fission fragments, so-called post-scission neutrons. The rest of the neutrons are evaporated from the compound nucleus during evolution of the system to the scission point. These neutrons are called pre-scission neutrons. The heavy fragments emit about $\sim$ 30 % less neurons than the light ones. An increase of excitation energy of the compound nucleus causes more intensive pre-scission neutron emission.

An experimental study of the fission product mass distributions clearly demonstrates the key role of the nuclear shell structure in the fission phenomenon. The most obvious example is an asymmetry of fission product mass distribution in the low energy neutron-induced or spontaneous fission of actinide nuclei. The mass asymmetry of fission products depends on the excitation energy and initial mass number of the fissile system. The former effect can be illustrated by figure 2.4. In the case of ^{235}U the fission product yields around symmetric division of the compound nucleus $A_{CN}/2 = 118$ increases almost two orders of magnitude with increasing of the neutron energy from about 0.025 eV of thermal neutrons to about 14 MeV of high energy neutrons. This is the most obvious and visible change in the fission product mass distribution with the raise of excitation energy. As mentioned in [30] minor variations of the mass distribution exist as well. For example, the width of the distribution becomes larger, the fine structure disappears and the average mass of the

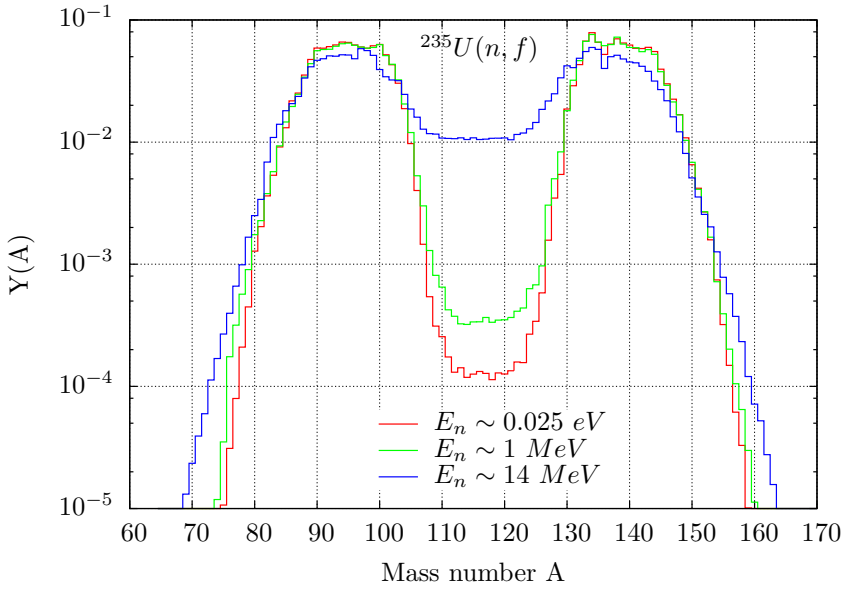

Figure 2.4: The fission product yields $Y(A)$ of the neutron-induced fission of ^{235}U. Evaluated data are taken from [37]. Yields are normalized to 2.0. Red line represents yields for fission induced by thermal neutrons, green — neutrons with fission energy spectrum, blue — high energy neutrons. Definitions of the neutron energy terms are given in [37].

light peak preserves its position whilst the heavy group shifts towards smaller mass numbers with increasing excitation energy. This means that the neutron evaporation becomes more active for the heavy group of fragments than for light ones at higher excitation energies. Probably such behaviour can be interpreted as a reduction of the shell effect in the compound nucleus and in the fission fragments, see details in [17] and recent explanation in [38].

Another important attribute of the fission product mass distributions is shown in figure 2.5. The fission product yields $Y(A)$ refer to the fission of various actinide materials induced by neutrons with fission spectrum energies [37]. One can see that with an increase of the compound nucleus mass number the position of the light group of fission products shifts towards higher masses while the heavy one stays near the same place. This dependence is typical and can be observed for other projectile particles, in other energy ranges and for spontaneous fission as well. It seems that this tendency also related to the nuclear shell structure. Mass numbers of

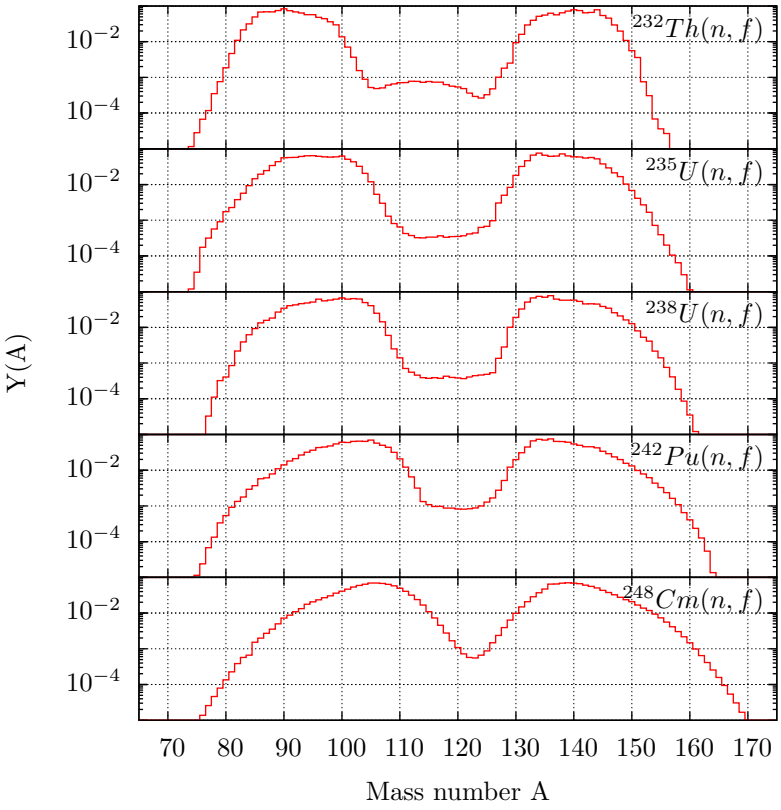

Figure 2.5: The fission product yields $Y(A)$ of the fast neutron-induced fission of various actinide nuclei. Evaluated data are taken from ENDF-349 data library [37].

heavy fission products are mainly distributed around A ∼130–145, what corresponds to the closed shells Z=50 and N=82.

2.2 Theoretical description of the fission product yields

As shown above nuclear fission demonstrates the tight connection between collective and individual properties of nucleons in a nucleus. Various models have been suggested to combine both types of interactions and to explain nuclear fission. The fission yield measurements at the IGISOL facility have always been closely associated to model development. A particular goal of the model development has been the ability to estimate the fission product yields that are available from the experiments.

A model developed by Valery Rubchenya has been used at IGISOL and is used also in this work. The approach and the underlying assumptions of this model are briefly described below. More details of the model can be found in [39, 40].

Previously it was considered that the fission process begins when a compound nucleus passes the saddle point. Usually in the real situation a nuclear reaction precedes the fission. Figure 2.6 schematically illustrates the fission phenomenon induced by a light particle. It represents different stages of the induced fission,

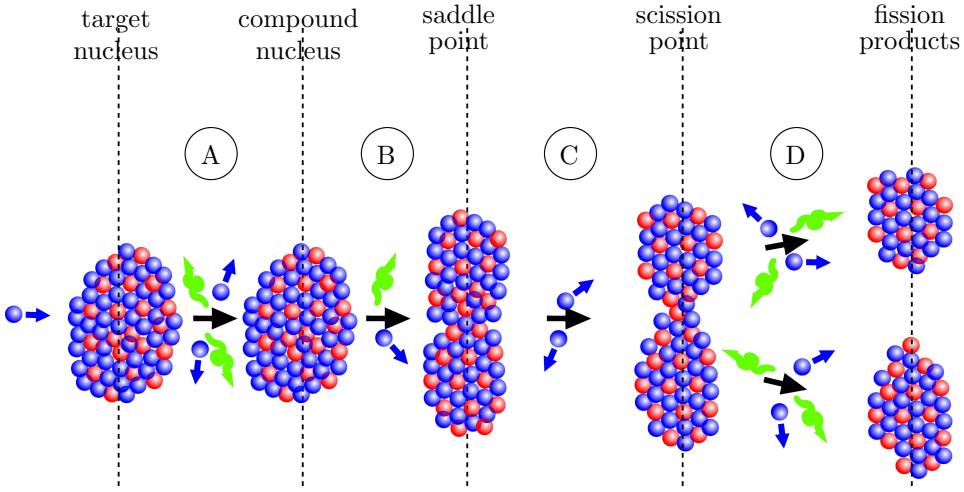

Figure 2.6: Schematic representation of the model, which is used to describe fission product yield distributions. Letters A, B, C and D refer to the processes, which describe the evolution of the system at different stages.

which are included in the theoretical model. The calculation of the fission product formation cross-sections includes description of a nuclear reaction, the fission process itself and de-excitation of the primary fission fragments.

The nuclear reaction stage begins from interaction of a projectile particle with a target nucleus and leads to the formation of a thermal equilibrium of the compound nucleus. This state is reached via emission of light particles in a pre-equilibrium process (A). As a result distributions of the mass number A_{CN}, proton number Z_{CN}, excitation energy E^*_{CN} and spin J_{CN} can be calculated for the ensemble of compound nuclei.

The evolution of the compound system towards the scission point defines the fission process and consists of two stages (B and C). The first stage (B) corresponds to the transition from the thermal equilibrium to the saddle point. During this stage a cascade of decay light particles or γ-rays can be emitted. The time-dependent statistical model [41] describes the characteristics of the process. Stage (C) refers

to the descent from the saddle to the scission point. Nuclear friction is considered as a mechanism of energy dissipation. A characteristic time of this stage is about $\tau \sim 5 \cdot 10^{-21}$ s and this is used as a parameter [40]. Even though this time is rather short, the model takes into account emission of neutrons and γ-rays during this period.

At the end of stage (C) the compound nucleus divides into two fragments. Configuration of the system at the scission point defines mass, charge and excitation energy distributions of the primary fission fragments, the so called pre-neutron distributions. During the next stage (D) the fission fragments release their excitation energy emitting neutrons and γ-rays. After which the fission fragments become fission products. The fission products then decay via emission of β-particles, delayed neutrons and γ-rays.

The FIPRODY code based on the described model was used to calculate the independent fission product cross-sections $\sigma(A, Z)$ for light particle induced fission of ^{238}U and ^{232}Th. In Chapter 3 the calculated yields will be compared with the experimental results.

2.3 Fission product yields' definitions

As it was mentioned before the term ***fission products*** refers to the nuclear species after emission of prompt neutrons and prompt γ-rays. On the contrary the term ***fission fragments*** is used before the emission of prompt neutrons [17]. The fission products decay mainly by emitting β-particles, γ-rays and so-called delayed neutrons. These decays change the mass and charge distributions of fission products. A clear definition of different kind of fission product yields allows comparison of experimental results obtained from various techniques and to compile those data in databases [42, 43, 44, 45]. In this work definitions of the fission product yields from [46] will be used.

Denoting a nuclide as (A, Z), where A is its mass number and Z is the proton number. The ***independent product yield*** $Y(A, Z)$ of this nuclide is the number of atoms with this given A and Z produced directly from fission before any radioactive decay. This definition does not distinguish isomeric and ground states. The independent yield $Y(A, Z)$ represents a sum over all long-lived excited states and ground state. It is customary for binary fission to normalize the independent yield to 2 per one fission event.

$$\sum_{A,Z} Y(A, Z) = 2. \tag{2.17}$$

This simply means that two products are formed in one event of the binary fission.

It is useful to choose the mass number A and the proton number Z as independent variables. When the fission products decay only via β-process without delayed neutrons the mass number remains the same. It means that the yield distribution

will evolve towards the low point of the β-stability valley along lines where the mass number is constant. This can be illustrated by figure 2.7. In the figure a part of the

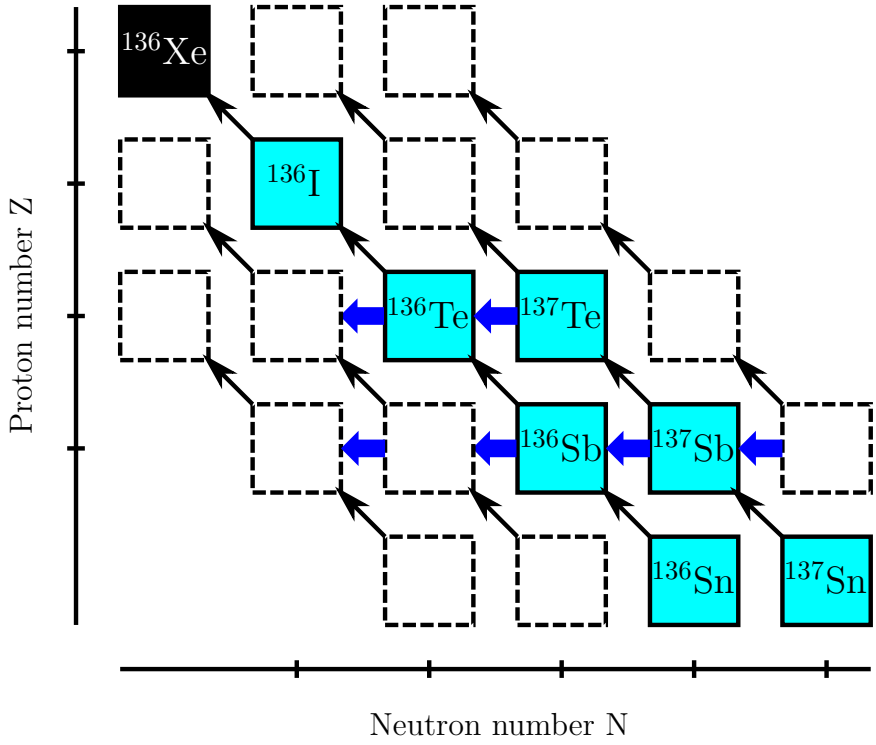

Figure 2.7: Illustration of decay paths of the primary fission products. Black arrows corresponds to the β^--decay and blue arrows represent the emission of delayed neutron.

chart of nuclides is shown. Black arrows are the β-transitions and blue ones represent delayed neutron emission. Black square ^{136}Xe is a stable nuclide and designates the valley of stability. For example, the independent yield of ^{136}Sb is the number of atoms produced in nuclear fission before ^{136}Sn and ^{137}Sn decays.

The ***cumulative yield*** $C(A, Z)$ specifies the total number of atoms of the nuclide (A, Z) produced directly in one fission and via decay of all precursors [46]. This definition is irrelevant to a moment in time. It simply means that the cumulative yield of the nuclide of interest equals to the sum of the independent yield of this nuclide and cumulative yields of all immediate precursors multiplied by certain branching

ratios. For example, the cumulative yield of ^{136}Sb will be:

$$C(^{136}Sb) = Y(^{136}Sb) + b_{\beta^-}C(^{136}Sn) + b_{\beta n}C(^{137}Sn), \tag{2.18}$$

where b_{β^-} is the β-decay branching ratio and $b_{\beta n}$ is the branching ratio of the β-delayed neutron emission. If, for example, tin isotopes are extreme nuclides of the isobaric chains, then their cumulative yields are equal to their independent yields $C(^{136}Sn) = Y(^{136}Sn)$ and $C(^{137}Sn) = Y(^{137}Sn)$.

Following [46] and [47] one should distinguish the total chain yield and the mass number yield. The ***mass number yield*** $Y(A)$ is the sum of all independent yields of a particular isobaric chain with mass number A:

$$Y(A) = \sum_{Z} Y(A, Z). \tag{2.19}$$

The ***total chain yield*** $Ch(A)$ equals to the cumulative yield of the last member of the isobaric chain A. For example, in the case of the mass number $A = 136$ the last nuclide in the chain is ^{136}Xe. The total chain yield is equal to the cumulative yield of the ^{136}Xe.

$$Ch(136) = C(^{136}Xe). \tag{2.20}$$

The difference between the total chain yield and the mass number yield consists of the effect of β-delayed neutrons [47]. The former yield is determined after emission of delayed neutrons and the latter one refers to the yield before delayed neutron emission. For mass numbers where nuclides don't emit delayed neutrons both yields coincide.

Some long-lived fission products such as ^{142}Ce, ^{144}Nd, $^{146-149}$Sm, and ^{150,152}Gd have half-lives greater than a million years and alpha decay. These decays change the post-decay mass distribution and this effect can be visible in experiments carried out on human timescale [42]. Such effect is not observable in relatively short on-line experiments with accelerator beams and thus it is ignored in the data analysis.

Details of experimental measurements of the fission yield by various techniques, their advantages and disadvantages can be found in [46].

2.4 Light particle-induced fission of ^{232}Th and ^{238}U

At the IGISOL facility the nuclear fissions of ^{232}Th and ^{nat}U are employed to produce neutron-rich radioactive ion beams. Natural U contains 99.27 % of the ^{238}U isotope. The cross-sections of light particle-induced fission of ^{235}U and ^{238}U are quite similar for ∼1–50 MeV incident energies.

The neutron-induced fission of ^{235}U does not have a significant contribution to the studied fission yields. This is because in the studies at IGISOL an ion guide specifically designed for the proton induced fission reaction is used, see chapter 4.5.

In this arrangement the target is so thin that the majority of fission neutrons escape from it. Some neutrons are produced by the stray beam hitting on the beam tube wall and collimators. However, the major source of neutrons is the beam dump about two meters downstream from the IGISOL target. The beam stop is made of pure aluminium. An upper limit estimate for the total cross-section of neutron producing reactions in the beam stop is ∼100 millibarn. The beam stop is surrounded by an iron moderator, which is shielded by concrete and boron loaded polyethylene. Only the directly backscattered neutrons can thus be considered significant. Rough estimations shows that 1 μA proton beam induces about $\sim 10^9$ fissions per second in the ^{nat}U target and produces about $\sim 10^{10}$ neutrons per second in the beam dump. If all those neutrons could be thermalized and could pass through the target, they induce about $\sim 10^7$ fissions per second, assuming a 600 barns cross-section for the neutron-induced fission and 0.7 % abundance of ^{235}U in the IGISOL target. This is already about 1 % of the proton-induced fission rate. If to take into account a geometrical factor, which is about 10^{-5} and includes size of fissile material and a distance from the beam dump to the target position, then the number of fissions per second induced by neutrons becomes seven orders of magnitude less than that induced by protons.

There is significant difference in the thermal and fast neutron-induced fission rate. The distribution of fission products from ^{nat}U is essentially that from ^{238}U. In the following, no difference is made between ^{238}U and ^{nat}U, even though natural uranium is used as a target material in all experiments.

Neither natural uranium nor thorium are highly radioactive before the irradiation with protons or deuterons. Both materials are quite inexpensive. The highest cost is the preparation of the targets with a required thickness. As opposition to the standard Isotope Separator On-Line (ISOL) technique [48, 49], wherein a thick target is used (more than 1 g/cm^2), in the IGISOL method a thin target is employed. The thin target means that the thickness of the material is about or less than the average stopping range of reaction products. In ISOL all reaction products are stopped in the target material and then diffuse outside, whereas in IGISOL the reaction products are stopped in the surrounding low pressure gas. A typical thickness of the fissile targets used at the IGISOL facility is ∼15 mg/cm^2.

Usually, a 25 MeV proton beam and ^{238}U, sometimes ^{232}Th, target, are used for production of neutron rich nuclei. The p- and d-induced fission cross-sections of ^{232}Th and ^{238}U in comparison with the neutron-induced fission cross-sections are given in figure 2.8. Data have been extracted from the Experimental Nuclear Reaction Database (EXFOR) [45] and smoothed by spline interpolation. The energy range 7–14 MeV is shown in an expanded scale insert to highlight the cross-section of the deuteron-induced fission of ^{232}Th, for which experimental data are given in only two works [50, 51].

It can be seen from the figure 2.8 that in the given energy range up to 50 MeV the known proton and deuteron cross-sections behave in a similar way. The maximum

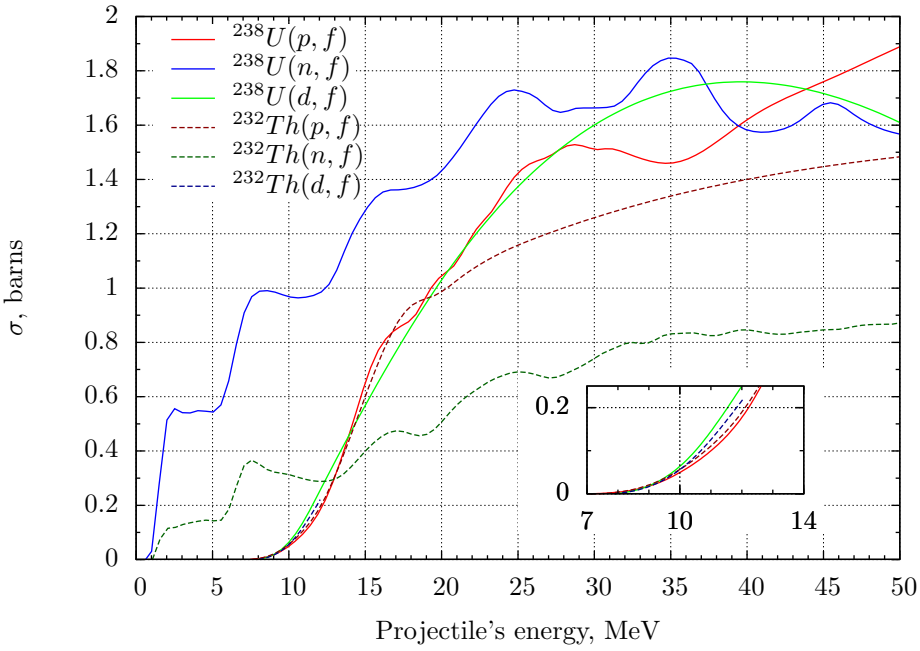

Figure 2.8: Cross sections for proton- , neutron- and deuteron-induced fission of ^{238}U and ^{232}Th extracted from the Experimental Nuclear Reaction Database (EXFOR) [45]. Solid lines represent reactions with the ^{238}U target and dashed lines — with the ^{232}Th target.

difference in absolute value is about 20–25 %. Up to around 28 MeV the two nuclides fission cross-sections are almost identical given either proton or deuteron irradiation and up to around 20 MeV the two nuclides cross-sections are similar.

The absolute values of neutron-induced fission cross-sections for ^{232}Th and ^{238}U differ by a factor of 2–3 in the presented energy range. The excitation functions of the n–induced fission of Th and U have a similar plateau structure. Such a structure is the result of additional contribution from a multi-chance fission. Figure 2.9 illustrates details of the multi-chance fission probabilities in the case of neutron-induced fission of ^{235}U [52].

The multi-chance fission happens when the compound system evaporates neutrons before decaying via fission. The excitation energy of the residual nucleus after n-emission is thus high enough for fission. The fission following neutron emission contributes to the total fission cross-section. The number of steps in the series of

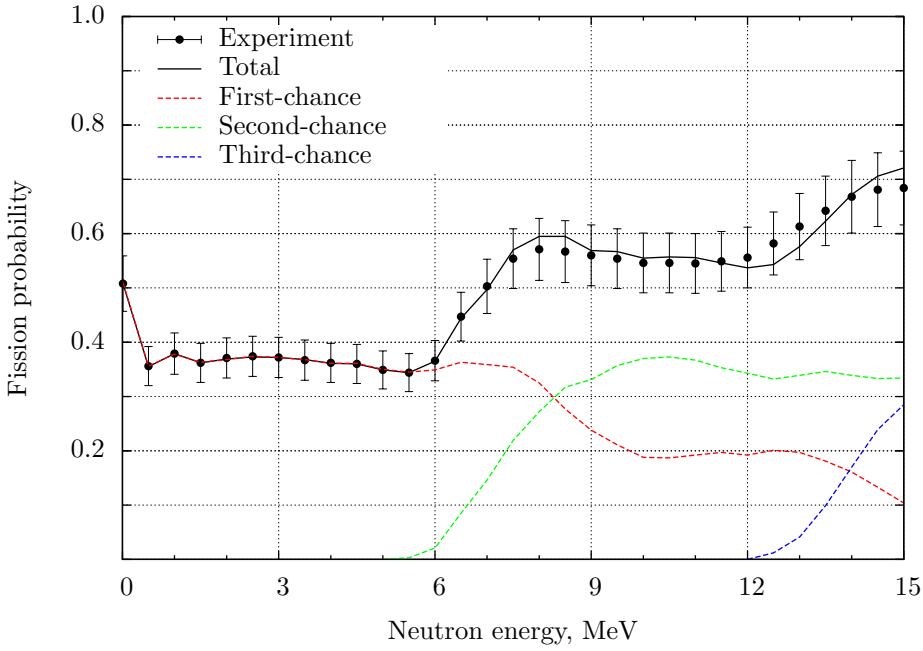

Figure 2.9: Multi-chance fission probabilities of the neutron-induced fission of ^{235}U. Lines refer to calculated multi-chance fission probabilities. Points represent ratios of experimental and calculated cross-sections. Details of calculations are given in [52],

neutron emission depends on the excitation energy of the initial compound nucleus.

The fission barrier of ^{235}U is lower than the neutron separation energy of ^{236}U. That's why the ^{235}U nuclei don't have a fissile threshold and can be fissioned by thermal neutrons with energy distributed around 0.025 eV. In figure 2.9 the fission probability in the 0–5 MeV range refers to the first-chance fission and equals to total fission probability of the excited nucleus of ^{236}U. Excitation energy in this case is approximately $E^*(^{236}U) = E_n + S_n(^{236}U)$. An increase of the neutron projectile energy increases probability of evaporating neutrons. If a neutron has been evaporated then the excitation energy of the remain ^{235}U nucleus equals:

$$E^*(^{235}U) = E_n - 2T, \tag{2.21}$$

where T is the temperature of the initial compound system. Typical nuclear temperature is about 0.5–1 MeV [17]. At a neutron energy about 6–9 MeV the excitation energy of $E^*(^{235}U)$ becomes close to its fission barrier and the system gets a second

chance for fission. The green dashed line in figure 2.9 shows the probability of the second-chance fission. Further increase of the neutron energy opens the possibility for the third-chance fission around 12–15 MeV. To be precise the third chance is given to the ^{234}U compound nucleus. The total fission probability is given as a sum over all chances:

$$P^{tot}(n,f) = P(n,f) + P(n,n'f) + P(n,n'n''f) + ..., \tag{2.22}$$

where $P(n,f)$, $P(n,n'f)$ and $P(n,n'n''f)$ are first-, second- and third-chance fission probabilities respectively.

It is possible to see from figure 2.8 that increasing projectile energy up to 50 MeV increases reaction cross-section. At the same time more excited compound systems are produced. Figure 2.9 demonstrates that at higher projectile energies of neutrons the second-and third-chance fission dominates on the first-chance fission. It means that at higher projectile energies more pre-scission neutrons are evaporated.

Previously, on page 14 and 15 it was mentioned that the probability of the symmetric fission — a process where two fission products with similar mass are generated — increases with increasing incident neutron energy. The number of evaporated neutrons from fission fragments is also larger at higher excitation energies. In some cases the incident particle energy can be an additional parameter to optimize the product yield with certain mass number.

In the aspect of production of neutron rich nuclides it is necessary to consider two important factors. First of them is the total fission cross-section and the second one is the independent fission product yield. Due to properties of the fission usually the two parameters are in contradiction.

In figure 2.10 the calculated independent yields of Sn isotopes are shown for three different projectiles. The FIPRODY computer code [40] has been used to calculate independent yields for the fission of ^{238}U. The neutron energy of 10 MeV has been chosen due to fact that the excitation function of the n-induced fission of ^{238}U at 10 MeV has a second plateau, where the absolute cross-section is about 1 barn (see figure 2.8). Excitation energy is quite low so that the compound system has only two chances for fission.

It can be seen that the distribution of Sn isotopes is shifted 2–3 mass units towards neutron-rich side in the neutron induced fission. Choosing a projectile particle and incident energy it is possible to increase the yield of neutron-rich isotopes more than two orders of magnitude.

^{135}Sn is the most neutron-rich tin isotope available at the IGISOL facility, whose mass has been measured [53]. The ^{135}Sn isotope has been produced in 25 MeV p-induced fission of ^{238}U. If we define the independent yield $\sim 10^{-8}$ (black arrow in figure 2.10) as a production limit of the IGISOL facility, then the contours in figure 2.11 can be plotted.

The independent yields have been calculated by the FIPRODY code [40]. The area inside contours represents the independent product yields of light particle-induced

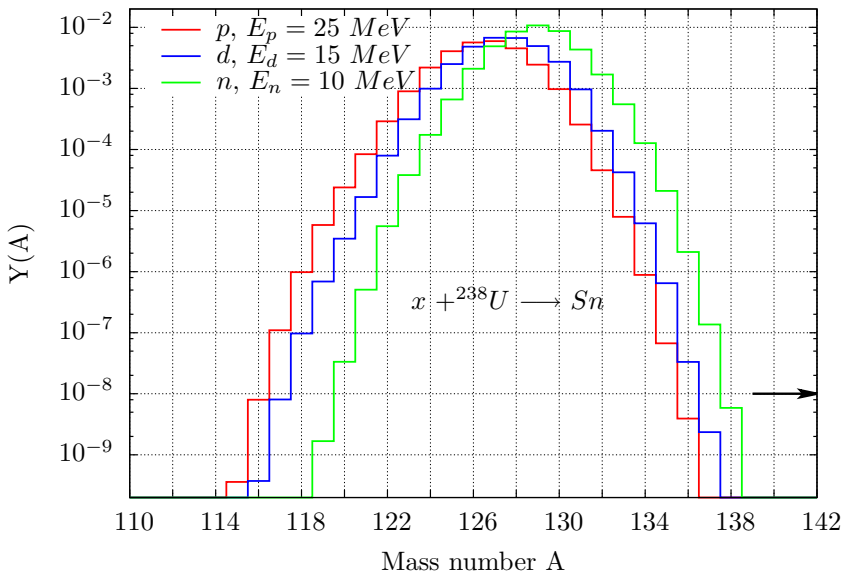

Figure 2.10: The calculated independent yield of Sn isotopes produced in p- (red line), d- (blue line) and n-induced (green line) fission of ^{238}U at 25, 15 and 10 MeV incident energies respectively.

fission of ^{238}U, which are larger than about 10^{-8}. Here, the total yield of fission products is normalized to 2.0. Information about natural abundance, proton and neutron drip lines has been taken from Nubase2012 [54]. Figure 2.11 demonstrates that the production limit for the n-induced fission is shifted on 1–2 neutron numbers towards more neutron-rich nuclides compare to the p-induced reaction.

It is worth of noting that the IGISOL technique with the neutron-induced fission has been already tested experimentally at JYFL [55]. The neutrons with the average energy about 20 MeV were produced by irradiation of a thick carbon target with 50 MeV deuterons. It was shown that the yield distributions shift towards more neutron-rich isotopes in the fission induced by neutrons.

2.5 Separation of fission products with IGISOL

The light particle-induced fission at low incident energies is an effective way to produce radioactive isotopes for fundamental research and applications. Fission products from the proton-induced fission of ^{238}U and ^{232}Th are widely utilized at IGISOL

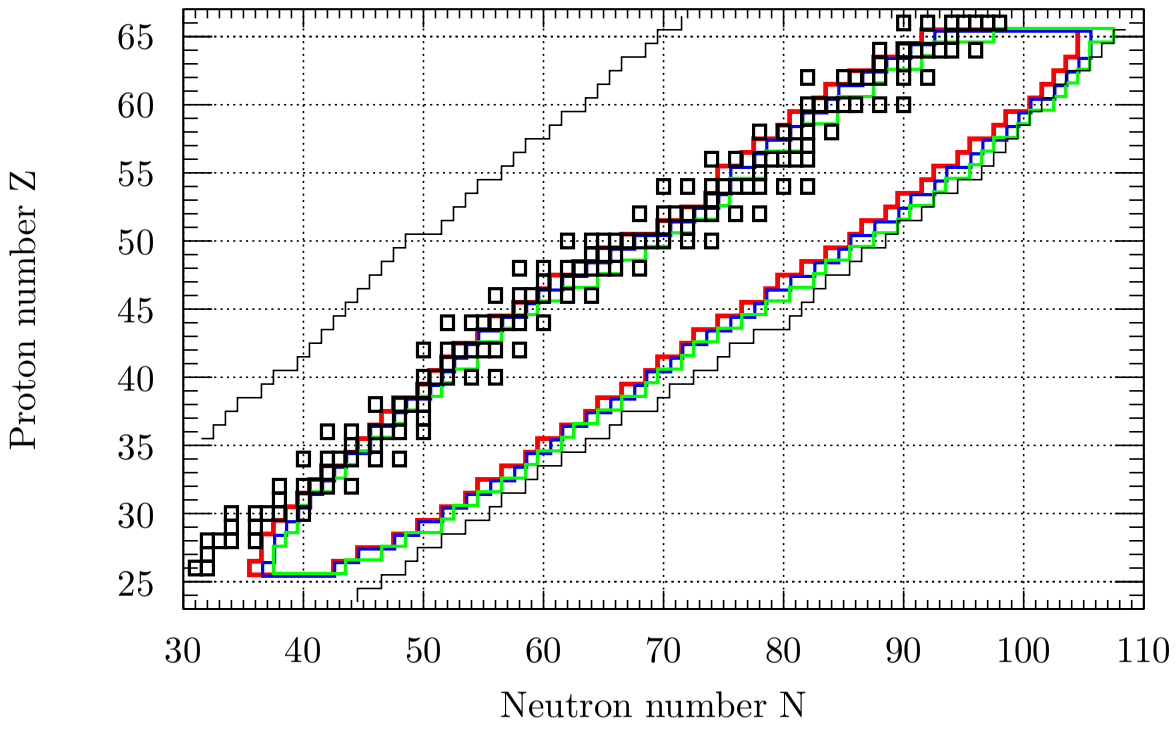

Figure 2.11: The 10^{-8} level contours of the independent fission product yields, calculated for p- (red line), d- (blue line) and n-induced (green line) fission of ^{238}U at 25, 15 and 10 MeV incident energies respectively. Black squares and lines refer to naturally occurring nuclides, proton and neutron drip lines respectively.

for atomic and nuclear structure studies. Figure 2.12 represents the schematic layout of IGISOL–4. The Ion Guide Isotope Separator On-Line (IGISOL) technique provides access to radioactive ions. Mass separated ion beams are delivered to the JYFLTRAP area equipped with various experimental apparatuses. One of them is the double Penning trap (JYFLTRAP), which is exploited for high-precision measurements.

In the IGISOL technique the reaction products are stopped in a noble buffer gas, typically helium. The initially high charge state of the ions produced in the nuclear reaction is lowered due to collisions with helium atoms. As a result the reaction products acquire the most probable charge +1. Then ions are flushed out from the gas cell (the ion guide) (1) with the gas flow and directed to the mass separator (5) by radio-frequency and electrostatic elements, (2) and (3, 4) respectively, as shown in figure 2.12. A differential pumping system allows efficient removal of a relatively high gas load from the target chamber whilst keeping a good vacuum in the beam line. Finally electrostatic elements in the beam switchyard (6) distribute the mass separated beams into three lines, equipped with experimental setups. The slowest element in the system is the ion guide (1) with the mean delay time of the order of some tens of milliseconds. This time is required to evacuate the whole volume of the gas cell. Therefore the ion guide constrains the capability of the IGISOL method to measure properties of short lived nuclides.

Due to its delay time within the IGISOL technique one deals with fission products. Assuming that the fraction of the fission products with half-lives less than several milliseconds is rather small, then the mass separated beam contains mainly the fission products after emission of the prompt neutrons and γ-rays but before any radioactive decay and hence emission of delayed neutrons.

The most important component of the IGISOL technique is the ion guide (1) (figure 2.12). Its schematic view in the case of the proton-induced fission is presented in figure 2.13. The light blue arrow shows the primary proton beam and the red one indicates the extracted radioactive ions. The target (2) of 15 mg/cm^2 thickness is positioned so that its surface is at a 7° angle with respect to the primary beam axis, see figure 2.13. Such a position increases the effective thickness of the target to 120 mg/cm^2 while the real thickness is kept sufficient small. If the target is too thick, most of the fission products cannot escape the target. If the target is too thin, the products leave the target at such high energy that only small fraction is stopped in the buffer gas. An appropriate real thickness is thus of the order of the fission product stopping range in the target.

The key element of the IGISOL technique is the buffer gas, typically He, which slows down the fission products. The buffer gas also cools the target. The fissile material is placed in the gas volume (green area on the scheme). Havar® windows (1) and (5) isolate the gas volume from the vacuum of the target chamber. Projectile particles pass through the whole ion guide and directly interact with the buffer gas creating plasma. The nickel foil (4) of 0.9 mg/cm^2 thickness separates the volume

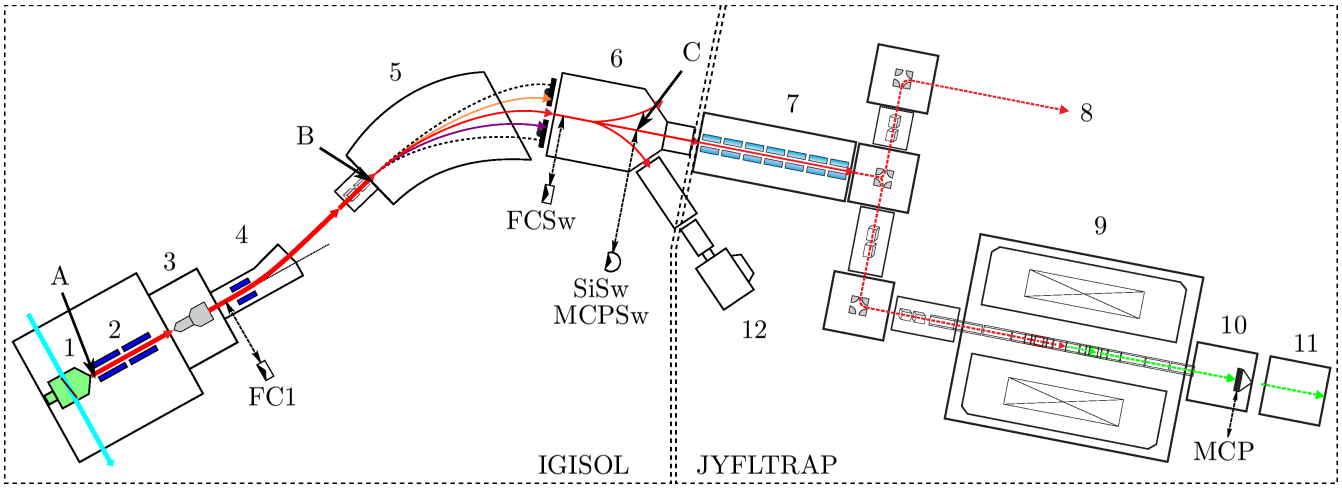

Figure 2.12: Schematic layout of IGISOL–4, ground floor. 1 — gass filled ion guide with a target; 2 — sextupole ion guide (SPIG); 3 — vacuum chamber with extraction electrodes; 4 — beam bending plates; 5 — dipole magnet; 6 — switchyard; 7 — radio frequency quadrupole (RFQ) cooler-buncher; 8 — beam line towards a laser spectroscopy setup; 9 — superconducting magnet with the double Penning trap (JYFLTRAP); 10 — diagnostic chamber with a Faraday cup and a microchannel plate (MCP) detector; 11 — post-trap spectroscopy setup; 12 — β-γ spectroscopy setup; FC1 and FCSw are faraday cups. SiSw — silicon detector. MCPSw and MCP are detectors based on microchannel plates. Positions A, B and C are explained in Chapter 4.

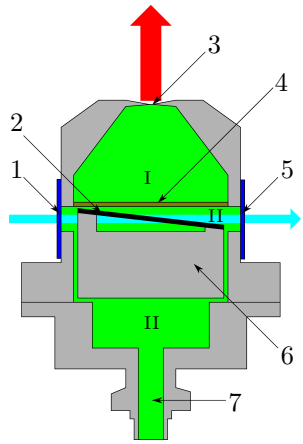

Figure 2.13: The ion guide for proton-induced fission. 1 — front havar window; 2 — fissile target; 3 — extraction nozzle; 4 — Ni separation foil; 5 — back havar window (havar® is a non-magnetic cobalt alloy that can be made into high strength foils); 6 — target holder; 7 — He gas inlet.

(I), where fission products are stopped and then extracted, from the volume (II), where the plasma is created by the primary beam.

An essential design parameter of the gas cell is the size of the volume (I), see figure 2.13. It affects both the extraction time and stopping efficiency. The extraction time is required to evacuate the whole gas volume (I). The stopping efficiency defines the fraction of fission fragments which are stopped inside the buffer gas. Fission fragments have a broad kinetic energy distribution. One part of the fission fragments can not escape the target due to low kinetic energy. Another part has too high kinetic energy and directly implants into walls of the ion guide. Only particles with appropriate energy are thermalized in the gas volume. To be precise an absolute value of stopping efficiency is individual for each nuclide and depends on the mass and proton number of the nuclide.

Not all ions stopped in gas can be extracted from the ion guide. Charge exchange reactions in the buffer gas and interactions with walls lead to ion losses. The extraction efficiency is defined as a fraction of ions which can be extracted from the gas cell. The total efficiency of the ion guide equals to product of the stopping and extraction efficiencies.

The typical inner volume of the proton-induced fission ion guide is about 100 cm^3. It allows relatively quickly, in some tens milliseconds, extraction of the fission product ions. At the same time the model calculations [56] shows that the stopping efficiency of the ion guide is approximately mass independent for fission products and on

average amounts to 1 %. The extraction efficiency reduces the total efficiency of the gas cell. The measured total efficiency of the ion guide for proton-induced fission was about 0.02 % for particular the ^{112}Rh fission product [13]. Since that time the IGISOL facility has been significantly improved. The main modification has been done on the ion extraction side. The recent measurements at the new IGISOL–4 equipped with SPIG showed an increase in the total efficiency of the ion guide for proton-induced fission up to 0.1 % for ^{112}Rh.

The total efficiency can be improved by redesigning the construction of the ion guide. Increasing the gas volume does not alone solve the problem. A larger volume leads to longer evacuation time and hence to greater ion losses due to charge exchange reactions.

2.6 Neutron-induced fission

As shown in section 2.4 the independent yield of neutron-rich nuclides is higher for neutron-induced fission. It was decided to utilize this effect for production of neutron-rich isotopes at the IGISOL facility. A schematic view of the setup is shown in figure 2.14. The proposed idea became possible due to the new accel-

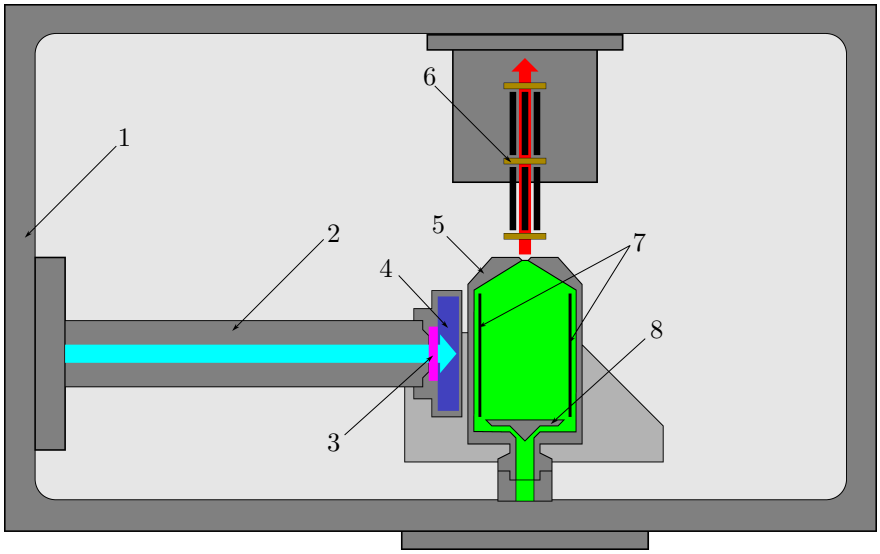

Figure 2.14: The idea of the project. 1 — target chamber; 2 — beam line; 3 — beryllium (Be) target; 4 — cooling water; 5 — fission ion guide; 6 — sextupole ion guide (SPIG); 7 — fissile targets; 8 — gas diffuser.

erator MCC30/15, which is supposed to provide high intensity beams of protons or deuterons.

The light blue arrow represents the primary proton beam. It penetrates through the 5 mm thick beryllium (Be) target (3) and stops inside cooling water (4). The thick Be target allows the utilisation of the full energy of the protons to create the maximum neutron flux. The negative side is that the neutron spectrum becomes broad, almost white. Neutrons created in the nuclear reaction ^{9}Be(p,n)^{9}B interact with fissile targets (7) placed inside the ion guide (5) filled with the He buffer gas (green area) at the pressure of about 300 mbars. The fission products escaping the targets are slowed down by the gas and extracted as a low energy radioactive beam (red arrow). The sextupole ion guide (SPIG) serves to guide ions further to the mass separator. Diffuser (8) provides a laminar flow of the gas. The vacuum in the target chamber (1) is kept at the level of 10^{-2}–10^{-1} mbar.

At first glance it might look like that this idea does not have a practical application due to losses in the conversion of protons into neutrons. Only one neutron is emitted in 1 steradian at the 0° angle per 200 projectile protons of 30 MeV energy in the thick Be target. Table 2.1 summarizes rough estimations for the extracted number of ^{136}Sn ions. The column "Factor" is the ratio of a parameter related to n-induced

Table 2.1: Comparison of the proton-induced and neutron-induced fission of ^{238}U for production of ^{136}Sn ions at the IGISOL–4 facility. * means that estimations have been made for geometry in figure 2.14.

Parameter	Proton-induced fission of ^{238}U	Neutron-induced fission of ^{238}U*	Factor
Proton beam intensity, μA	10	100	10^{1}
Beam on fissile target particles/s	10^{14} protons	**10^{12}** neutrons	**10^{-2}**
Fissions/s in the target	$\sim 10^{10}$	$\sim 10^{7}$	10^{-3}
Independent yield of ^{136}Sn	$\sim 10^{-9}$	$\sim 10^{-6}$	10^{3}
Ion guide			
stopping efficiency, %	1	**1**	**1**
extraction efficiency, %	10	**10**	**1**
Extracted beam of ^{136}Sn, ions/s	$\sim 10^{-2}$	$\sim$**10^{-2}**	**1**

fission to the same parameter of the p-induced fission. The values marked in bold can be improved by a redesign of the gas cell.

The fission cross-section for the neutron beam is averaged over the energy interval 1–30 MeV and equal about 1 barn. It is almost the same as for the proton-induced reaction. Additionally to the conversion factor the effective thickness of the target for proton-induced fission is 10 times larger than for the neutron-induced one. Such a geometrical factor is possible due to the size of the beam. The proton beam has a well focused spot about 5 mm across, but the neutrons are emitted into the 4π solid angle. This feature can be used to increase the surface of the fissile target in case of the neutron-induced fission.

As a result the fission rate in the target for proton-induced fission is three orders of magnitude larger than the rate for neutron-induced reaction. The independent yield of ^{136}Sn has an opposite ratio according to calculations on the model [39, 40], see figure 2.10. Finally the amount of extracted ^{136}Sn ions is approximately the same for proton-induced and neutron-induced fission.

In the case of n-induced fission the full intensity of the proton beam available from the MCC30/15 cyclotron [57] can be utilized to produce radioactive beams. The stopping efficiency and extraction efficiency of the ion guide can be improved using different approaches. A large gas volume together with radiofrequency and electrostatic fields can significantly increase these parameters. At the present time there are several facilities employing these techniques, for example CARIBU [58] and at the GSI gas catcher [59].

The advantage of the neutron-induced fission is the high independent fission yields for neutron-rich nuclides. It is important to note that the isotopic distributions are shifted to the neutron-rich side of the nuclear chart (see for example figure 2.10). This means that a separated isobaric chain contains less contaminants close to the line of stability. Also the neutron beam does not create ionization in the buffer gas.

The equipment for the neutron-induced fission consists of two parts: a neutron source and an ion guide designed for the neutron beam. A detailed description of the neutron converter is presented in Chapter 4. It includes a choice of materials, features of the construction and results from neutron field measurements. A brief explanation of the ion guide design and some results of testing are summarized in Chapter 4.

This work focuses on the measurement of independent fission product yields. A unique method developed at the IGISOL group is based on the counting of individual atoms separated by JYFLTRAP and does not relay on decay properties of a nuclide. This method is self-sufficient and has been studied separately [15, 60, 61, 62]. In the frame of this thesis it was decided to use such techniques and compare independent yields of fission products from proton- and neutron-induced reactions. In this way it is possible to measure experimentally the shift of an isotopic distribution for a chosen element, for example Sn, and say how far away from the stability line neutron-rich nuclides can be produced.

To verify the method the independent fission products' yields were measured in the fission of ^{232}Th induced by 25 MeV protons. The result of the measurement

together with the description of the method is given in Chapter 3 of the present work. The yield measurement for the neutron-induced fission require more time for preparation and will be measured in the future.

3 Fission product yield measurements

Information about the fissile system at the scission point can be obtained from the fission fragment or product distributions. Many experimental methods have been developed to measure characteristics of fission fragments and products since the discovery of nuclear fission. These techniques varies from photographic emulsions and β- or γ-decay spectroscopy of chemically separated elements up to multiparameter measurements in inverse kinematics. Advantages and limitations of those techniques are comprehensively described in the report [46] and in reviews [63, 30, 64, 65].

Experimental methods to determine the independent yields have to be sufficiently quick so that the short-lived nuclides can be detected. Such requirements limit the amount of techniques, which can be applied for independent yields determination.

Initially, the radiochemical methods were applied for independent yields measurements. In these methods fission products with proton number Z were extracted from the irradiated samples by chemical reactions. Then the absolute activity of the extract was counted by detecting either β-, γ- or X-ray radiations. Several fast radiochemical techniques were developed to be able determine also the yields of the short-lived nuclides [66, 67, 68]. In some cases it was even possible to separate isomeric and ground states by radiochemistry [69]. However, the conversion of the determined absolute activity to the yields depends on decay properties of fission products, which are not always well known.

Classical mass spectrometry can be utilized for independent yields determination as well. In this case the irradiated target has to be coupled to an ion source to provide a quick transfer of the fission products between them. Classical ion sources can be chemically selective due to different ionization properties of elements. This can be utilized to choose "Z" of the measured nuclides and the independent yields can be obtained by mass scanning and ion counting [70, 71]. Another approach of the classical mass spectroscopy for fission yield measurements employs γ-counting of mass separated ions. Each nuclide has a unique nucleonic structure, which defines the spectrum of emitted γ-rays. The gamma emission after the mass separation typically follows the β-decay of the fission product. Some γ-decaying isomers are long-lived enough to become mass separated before their decay. The decay of the fission products can then be identified by the associated gamma transitions. The main issue of classical mass spectroscopy is the absence of a universal ion source, which can produce ions of all kinds of chemical elements.

In fission, all elements from nickel to holmium are produced. A traditional ISOL ion source that came relatively close to cover this region was the integrated target-

ion source at the OSIRIS on-line mass separator facility [72] in Studsvik, Sweden. All elements could be extracted from the ion source, with the exception of yttrium, zirkonium, niobium, molybdenium, technetium, ruthenium and rhodium. The efficiency was, however, different for different elements. The yields from the ion source depend on the desorption and diffusion properties of different elements, as well as on the half-life of the radio-isotope [73, 74]. With careful calibration, the yields from the separator could be converted to fission yields.

In principle, the direct γ-spectroscopy of the fissioning target could also be applied for the determination of independent yields. However, the complex γ-ray spectrum of unseparated fission products sets a technical challenge because of the simultaneous presence of the statistical, prompt yrast and β-delayed gamma rays. It would also cause difficulties in the data analysis relying on the decay characteristics of the nuclides.

A different approach to determine the independent yields is employed in experiments with unstopped fission products. Techniques based on registration of kinetic energies and velocities of both fission products are widely used to study their energy and mass distributions. It is assumed that fission is a binary process. The mass conservation for the primary fragments before prompt neutron evaporation can be written as:

$$M_F = M_L^* + M_H^*, \tag{3.1}$$

where M_F is mass of the fissioning system, M_L^* and M_H^* are masses of the light and heavy fragments before the evaporation of prompt neutrons, respectively. The momentum conservation in the system of the fissioning nucleus gives:

$$M_F = M_L^* v_L^* = M_H^* v_H^* \qquad \text{or} \qquad E_L^*/E_H^* = M_H^*/M_L^*, \tag{3.2}$$

If the mass of the fissioning system M_F is known, then the masses M_L^*, M_H^* can be obtained from the measured v_L^* and v_H^* ($2v$-method) or E_L^* and E_H^* ($2E$-technique). However, only the fission product's velocities (v_L, v_H) and energies (E_L, E_H) can be measured experimentally, i. e. after the prompt neutron emission. Thus the employment of equations 3.1 and 3.2 requires certain assumptions.

Another approach to obtain mass distributions of fission fragments is based on the simultaneous measurement of energy and velocity ((E, v)-method) or energy and momentum ((E, p)-method) of one fission fragment. The mass of a fission fragment can be extracted from equations:

$$E = Mv^2/2 \qquad \text{or} \qquad E = p^2/2M, \tag{3.3}$$

where E is the energy, M is mass and p is momentum of the fission fragment. A simultaneous measurement of both velocities and energies ($(2v, 2E)$-method) allows determination of the independent masses of both fission products and can obtain more details about the nuclear fission event.

The more challenging task is the nuclear charge identification. Methods to determine the nuclear charge Z of the fission products are based on the interaction of fast heavy ions with the electronic shells of the atoms in the stopping material. The ionization curve of the heavy ion, slowed down in a detector material, carries information on its charge. A so-called "Bragg" ionization chamber is capable of profiling the energy release from the decelerating fission product which allows determination of the nuclear charge of fission products. The ΔE–E method is also widely used for the measurement of nuclear charge. The energy loss ΔE of heavy ions in an absorber of given thickness depends on both their kinetic energy E and nuclear charge Z. Thus the measurement of ΔE and E allows determination of the nuclear charge. With this method the nuclear charge can be identified for elements with $Z \lesssim 45$ due to the relatively low kinetic energy of fission fragments.

For the studies of unstopped fission products, fission fragment recoil spectrometers that employ the (E, v)-method by electromagnetic separation, can reach a superior mass resolving power. The analysis however becomes complicated, since the mass yield is split between several charge states, each representing different m/q. Such spectrometers include the already closed HIAWATHA [75] at the The University of Illinois Advanced Teaching Research Isotope General Atomic (TRIGA Mark II) reactor in the Urbana campus (shut down 1998) and Lohengrin [76, 77] at the Institut Laue-Langevin (ILL) in Grenoble (still running). The target at both these separators was (is) positioned in the high neutron flux close to the reactor core.

A more compact solution is a spectrometer based on time-of-flight and fission product energy measurement without any electromagnetic elements. In this method it is also technically less challenging to build a two-arm construction needed for $(2v, 2E)$-techniques. The Cosi-van-tutte spectrometer [78] at ILL has pioneered these techniques. More contemporary (or future) apparatus for measuring fission products include FALSTAFF (Four Arm cLover for the STudy of Actinide Fission Fragments) spectrometer [79], to be installed in the Neutrons for Science (NFS) facility in SPIRAL2, employing $2v$-technique to determine the pre-neutron evaporation (fragment) mass, and (E, v)-method for the determination of the post-neutron evaporation (product) masses, as well as $(2v, 2E)$-spectrometers SPIDER (SPectrometer for Ion DEtermination in fission Research) in Los Alamos National Laboratory [80, 81, 82], STEFF (The SpectromeTer for Exotic Fission Fragments [83]) and VERDI (VElocity foR Direct particle Identification) constructed for the Joint Research Centre IRMM, Geel, Belgium [84].

Detailed description of the methods related to unstopped fission fragments can be found in [63, 30, 64, 65] and references therein.

A relatively new method for independent yields determination in fission is inverse kinematics [85, 86]. The ^{238}U uranium beam accelerated to relativistic $\approx$1 GeV$*$A energies is fragmented in a beryllium target. The selected secondary beam is directed to a secondary target, where it is excited either via the Coulomb interaction or nucleon transfer. The modest excitation energy in the region of 10–25 MeV leads

to the fission of the selected fragment beam. The nature of the excitation can be impacted by the choice of the secondary target material. At the FRagment Separator (FRS) in GSI, Germany, where the technique has been developed, an active secondary target system has been developed to improve the resolution and selectivity of the system [86, 87, 88, 89]. The method has been adopted by other laboratories with relativistic heavy ion beams. The fission of heavy fragment beams is utilised at the facilites of VAMOS [90] in GANIL, France, and SAMURAI [91, 92] at RIKEN, Japan.

The main advantage of the technique is that the fission of numerous actinides, many of them very short-lived, can be systematically studied along the nuclear chart. Due to inverse kinematics the fissioning system has a relatively high kinetic energy. As a result, fission products are emitted in a narrow cone in the forward direction within the laboratory system and their kinetic energy is much higher than that from fission in normal kinematics. High kinetic energy of the fission products allows identification of their nuclear charge by the ΔE–E-method in a range Z =30–64 [93].

3.1 Independent yields with IGISOL method and JYFLTRAP

The IGISOL technique has been employed for fission yield measurements since the late 1980's. Examples of works done in Jyväskylä can be found in [94, 95, 96, 97, 55, 98, 99, 100]. The IGISOL technique has been used for yield surveys also in Sendai, Japan [101, 102, 103]. In all these works, γ-ray detection of mass separated fission products were utilised for identification and counting of the fission products.

The IGISOL technique as such is well suited to fission yield measurements. It differs from the classical mass separator ion sources in three important issues. First, the IGISOL technique is element independent in the sense that ions of all chemical elements can be produced. This is because the most important ionisation mechanism is the nuclear reaction. Because of differences of the first ionisation potential of elements, the efficiency of the ion guide is not necessarily the same for all elements. Even so, in the first approximation, the differences are however very small. Second, the ions extracted from the ion guide are primary ions from the nuclear reaction. Therefore, there is no other delay than what time is spent in flushing the ions out of the gas cell. The atoms do not need to diffuse through the target body. Target porosity or temperature do not influence the delay times. Third, unlike in a classical ion source, there is no significant accumulation and re-ionisation of the decay products. The rate of production of a particular ion in the IGISOL ion beam is directly proportional to its production cross section. The only known exception to this is discussed below.

It is reported in [104] that in the experiment with fission products at the Leuven IGISOL system, fission products were observed during the cyclotron beam off period. The origin of these ions was found to be the β-decay of isotopes that had been stuck on to the surface of the SPIG electrode rods. The β-decay recoil was sufficient to release them from the rod surface. In addition, the β^--decay automatically leads to formation of at least a singly charged ion. This effect was confirmed at IGISOL–3, as reported in [105]. The magnitude of the effect is less than 1 %. As the uncertainty of fission yield measurements due to other reasons remains above the level of a few per cent, the impact of such a small effect can be neglected.

The possible variation of the ion guide efficiency is someting with which one should be more concerned. This was acknowledged in early yield measurements at IGISOL by measuring the yields of the studied isotopes, in addition to atomic A^+ ion beams, in molecular monoxide $(A + 16)^+$ and hydroxide $(A + 17)^+$ beams [94, 95]. By introducing improved buffer gas purification techniques the intensity of the molecular beams was reduced to an insignificant level.

In several works both in Jyväskylä and in Sendai, Japan, not only the isotopic (A distribution of a certain nuclear charge Z) but also the isobaric (nuclear charge Z distribution of a certain mass number A) yield distributions were studied [94, 95, 55, 100, 102, 103]. Two things can be concluded from these works. The deduced isobaric Z distributions resembled quite universally a Gaussian distribution, as expected. This would not have been the case, if the efficiency of the ion guide had been radically dependent on the chemical properties of the ions. In addition, 25 MeV proton induced fission of ^{238}U was studied both in Jyväskylä [55] and in Sendai [102]. Although there was a significant difference between the size of gas volume of the ion guides utilised in the experiments, the deduced most probable charge Z_p and the width σ_Z of the isobaric distributions were in agreement.

It is possible to get around the chemical dependencies of the ion guide by measuring the isotopic yield distributions. When yields of two isotopes of the same element are compared, the chemical efficiency of the ion guide is expected to be the same. As an early example, the isotopic yield studies of Ni, Cu, Zn, Ga and Ge in the 25 MeV proton-induced fission of ^{238}U [97, 98] gave the first experimental indication of the existence of the so-called superasymmetric fission mode.

In principle, there is mass dependence in the stopping efficiency of the fission products in the gas volume of the ion guide, and therefore the total efficiency of the ion guide would be different for different isotopes of the same element. Some indication of the isotopic dependency of the ion guide efficiency was presented in [95], but any such effect has not observed experimentally since. The recent simulations of the ion guide performance [56] show that the nickel foil between the target volume and the stopping volume of the proton-induced fission ion guide, figure 2.13, slows down the fission products in a mass dependent way. The direction of these different mass dependencies is opposite. The net result is that the fraction of the fission products stopped in the gas volume is independent on the ion mass.

A new method to determine the independent yields has been developed at JYFL [15, 60, 61, 62]. It utilizes the capability of the IGISOL technique to produce a low energy ion beam of any chemical elements and a high mass resolving power of a Penninng trap. An identification of individual nuclides by their mass and counting ions by the MCP detector significantly distinguishes the proposed method from techniques mentioned above. The main advantage of the method is that the obtained yields do not depend on decay properties of the fission products, which are not well known for neutron rich isotopes. Decay loss corrections implemented in the data analysis procedure exceed 1 % only for nuclides with half-lives < 30 seconds. A high precision for the determination of nuclide masses is not needed for the measurements, because masses are used only to identify peaks in mass spectra.

The use of JYFLTRAP for fission product identification makes the issue of chemical efficiency of ion transmission more complicated. The gas cell environment is known to be a stage of rapid gas chemistry and ion exchange reactions. As an example, krypton ions tend to neutralise relatively easily in charge exchange reactions. The reason for this is the high first ionisation potential of krypton. The other example of ion sensitivity is yttrium that forms monoxide molecules with any impurity of oxygen in the gas cell.

In practice, however, the differences of the transmission efficiency through the RFQ — JYFLTRAP system between elements are very small. The isotopic fission yield distributions of 25 MeV proton-induced fission of ^{238}U have been determined with JYFLTRAP. From this experimental data it is possible to construct the isobaric nuclear charge distributions. These distributions typically have a gaussian shape. Moreover, the most probable charge Z_p and the charge distribution σ_Z are in agreement with the previous studies [55], [102], where the isotopes were identified with γ-ray spectroscopy. Exceptions of this were As and the aforementioned Kr.

3.2 Experimental technique

The separation of the fission products with the IGISOL technique in general was described in section 2.5. A brief review of the method is given together with a description of experiments for the determination of independent product yields in the fission of ^{232}Th induced by 25 MeV protons. Presented data were obtained during two experiments: in April 2010 at the IGISOL–3 facility and in April 2014 at IGISOL–4.

The design of the fission ion guide was the same in both experiments. The proton beam with intensity of 1 μA induced nuclear fissions in the 14 mg/cm^2 thick ^{232}Th target, located in the fission ion guide of the IGISOL facility [14, 106]. Ionized atoms of the fission products were formed in the nuclear fission. Some of the ions escaped the thorium target, passed the separation nickel foil and stopped in helium buffer gas. Due to charge exchange reactions the majority of the fission products end up with

the charge state 1^+. The helium flow transported ions out of the gas cell through a 1.2 mm in diameter exit nozzle. After the nozzle they were guided by a sextupole ion guide (SPIG) [107] towards extraction electrodes, which accelerate ions to an energy of $30q$ keV before magnetic separation. The dipole magnet with the mass resolving power $m/\Delta m \approx 500$ separated an isobaric chain with fixed mass number A. The mass separated continuous ion beam was injected in a radiofrequency quadrupole (RFQ) cooler-buncher [108], where ions were collected for several hundreds of milliseconds.

The whole cooler-buncher is installed on a high-voltage platform to decelerate $30q$ keV ions to the energy of ∼100 eV. The RFQ structure, figure 3.1, consists of

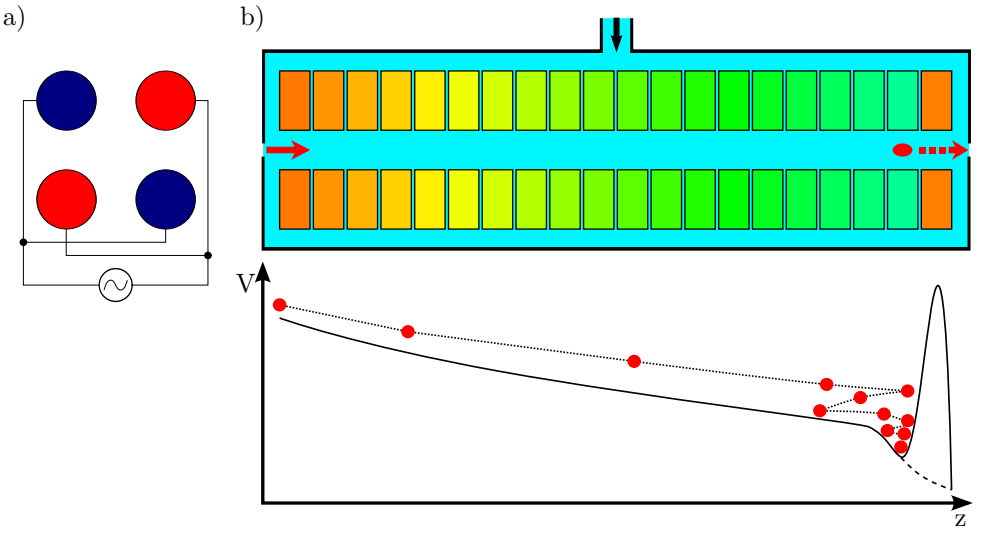

Figure 3.1: Principle scheme of the radiofrequency quadrupole (RFQ) cooler-buncher. a) is a connection diagram of four rods to the RF generator. b) rod segments in the gas volume with electrostatic potential along rods.

four segmented rods placed inside the helium buffer gas at a pressure of 0.1 mbar. The ions loose their energy in collisions with buffer gas atoms. Radiofrequency voltage with the same phase is applied to the opposite rods of a quadrupole and the neighbour rods have opposite phases, see figure 3.1(a). The RF field confines ions transverse to the beam axis. Cooled ions are collected in an electrostatic potential well created by the rod's segments along the beam direction, figure 3.1(b). The short bunches of ions with a duration of 10–15 μs are released to JYFLTRAP.

The JYFLTRAP setup consists of two cylindrical Penning traps located in the uniform 7.0 T magnetic field [109, 110]. The electrode structure of both traps is identical and it is shown in figure 3.2. The only difference is that the purification

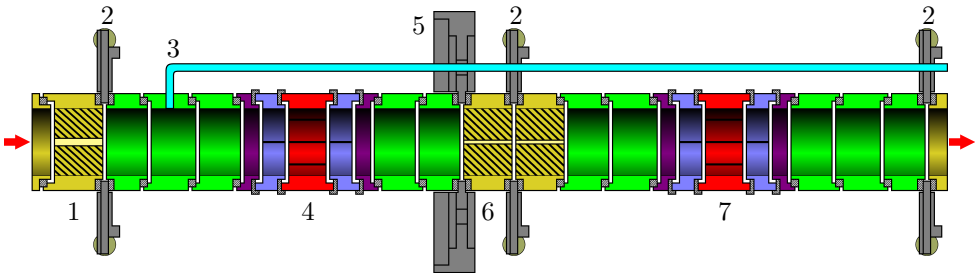

Figure 3.2: The electrode structure of JYFLTRAP placed in the uniform 7.0 T magnetic field. 1 — injection diaphragm of 4.0 mm in diameter, 2 — supports, 3 — gas feeding line, 4 — segmented ring electrode of the purification trap, 5 — pumping barrier, 6 — diaphragm of 2.0 mm in diameter at IGISOL–3 (1.5 mm in diameter at IGISOL–4), 7 — segmented ring electrode of the precision trap.

trap is filled with the helium buffer gas, while the second trap is kept under ultra high vacuum (10^{-9}–10^{-8} mbar). The pumping barrier (5) and the diaphragm (6) serve to separate traps' volumes. Only the first, so-called purification, trap was used in experiments described in the present work.

In general, the distinctive feature of a Penning trap to confine charged particles is the combination of a static quadrupolar electric field and a homogeneous magnetic field. The electrodes, shown in figure 3.2, form the quadrupole electrostatic field and they are used to move ions along the structure. A superconducting solenoid provides the 7.0 T magneic field with homogeneity of about 1 ppm in the volume of 1 cm^3 at the center of both traps. Technical deteail of JYFLTRAP can be found in [110] for IGISOL–3 and in [111] for the IGISOL–4 facility.

The motion of a trapped ion in the ideal Penning trap can be represented by three periodic eigenmotions. Figure 3.3 shows the trajectory of a charged particle in the Penning trap. One of them occurs along the lines of magnetic field with the frequency ν_z. The two circular motions happen in the plane transverse to the magnetic field, i.e. vector $\vec{B}$ in figure 3.3. The so-called magnetron motion with the orbit (1) has frequency ν_-, which is almost mass independent. The reduced cyclotron frequency ν_+ depends on the ion mass and describes their reduced cyclotron motion on the orbit (2). The cyclotron frequency of an ion in the ideal trap can be written as:

$$\nu_c = \nu_+ + \nu_- = \frac{1}{2\pi}\frac{q}{m}B, \tag{3.4}$$

where B is the magnetic field, q is the charge of the ion and m is its mass. In case of the real Penning trap with unharmonic fields the more general equation should be

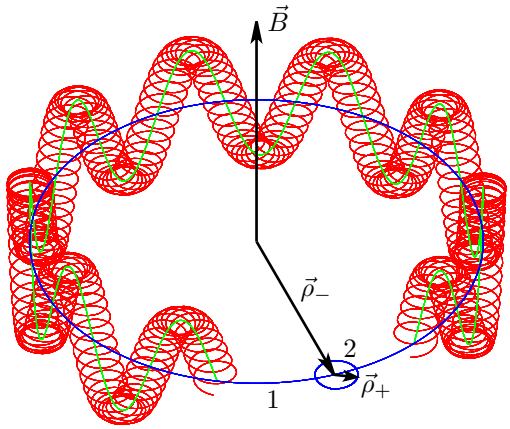

Figure 3.3: Ion's trajectory in the Penning trap. There are three eigenmotions: the axial motion along the magnetic lines $\vec{B}$ and two radial motions. 1 — orbit of the magnetron motion with the radius ρ_- and 2 — orbit of the reduced cyclotron motion with the radius ρ_+.

used [112, 113]:

$$\nu_c^2 = \nu_+^2 + \nu_-^2 + \nu_z^2. \tag{3.5}$$

The buffer gas in the trap acts on the ion as a viscous substance with a damping force proportional to velocity. Electrical and magnetic fields in the Penning trap are configured in a such way that the ion has a maximum total energy at the center of the trap. Collisions of the ion with atoms of the buffer gas reduce its energy of motion. As a result, the ion tends to move away from the trap center. Finally, ions will be lost due to an interaction with the trap electrodes.

To restrain the radial blow out of the ion cloud an external radiofrequency quadrupole field has to be applied. If the frequency of the external quadrupole field equals to the true cyclotron frequency 3.4, then the initial magnetron radius ρ_- will decrease while increasing the cyclotron radius ρ_+ until the magnetron motion is completely transformed to reduced cyclotron motion [114]. The energy of the reduced cyclotron

and axial motions dissipates in collisions with atoms of the buffer gas and ions are concentrated at the center of the Penning trap. Dependence of the true cyclotron frequency ν_c on the ion's mass, see equation 3.4, makes this technique mass selective.

The buffer gas cooling technique [114], briefly described above, is used to separate isobars and prepare a pure radioactive ion beams at the IGISOL facility [115, 116]. Manipulations with trapped ions are implemented by applying radiofrequency signals to the segmented ring electrodes (4) and (7), see figure 3.2. A diagram in figure 3.4 shows connections between segments and signal generators of the ring electrodes at JYFLTRAP. The central ring electrodes of JYFLTRAP have eight segments, which

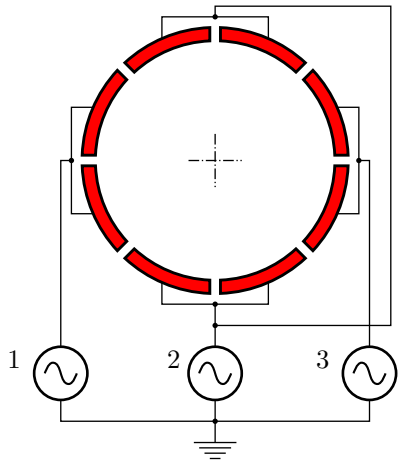

Figure 3.4: Connection diagram of the ring electrodes. 1 — generator for the dipolar excitation at the magnetron frequency ν_-, 2 — generator for the quadrupolar excitation at the cyclotron frequency ν_c, 3 — generator for the dipolar excitation at the reduced cyclotron frequency ν_+.

are interconnected to form four quadrants.

In a dipolar excitation the signal from a RF generator is applied to the opposite quadrants in such a way that the frequency and amplitude are the same, whereas the phase is opposite. A quadrupolar excitation means that the RF signal of the same frequency, amplitude and phase feeds opposite quadrants, while the signal on the two other quadrants differs from the first one by opposite phase. A simplified excitation scheme is used at JYFLTRAP [110]. In case of the dipolar excitation the RF generator is connected only to one quadrant, while static voltage is applied to others, see figure 3.4. Two generators (1) and (3) serve for the dipolar excitations on the magnetron frequency ν_- and the reduced cyclotron frequency ν_+, respectively. The quadrupolar excitation scheme at JYFLTRAP is simplified as well and it is

usually called a side-band excitation. It means that the RF signal from the generator (2) is applied to two opposite quadrants, while the other quadrants are kept under constant potential.

In the present work the independent fission yields were determined employing the isobaric mass separation technique [115, 116]. The next sequence of manipulations with trapped ions was implemented to obtain a single mass spectrum. The bunch of ions released from the RFQ cooler-buncher is injected into the purification trap through diaphragm of 4.0 mm in diameter, see figure 3.2. After an initial cooling period (∼100–150 ms) the dipolar excitation is initiated for about 10 ms at the magnetron frequency ν_-. Thus all ions independently on their masses see their magnetron radius increasing. The amplitude of the generator is adjusted in such a way that no ions can pass through the diaphragm (6) in figure 3.2. Immediately after the dipolar excitation, a quadrupolar excitation at the cyclotron frequency ν_c was activated for several hundreds milliseconds. Due to conversion of the magnetron motion to modified cyclotron motion and energy dissipation in collisions with atoms of the buffer gas the ions, whose mass satisfies equation 3.4, are centered in the trap. Then ions are extracted from the trap by changing electrostatic potential along the beam axis. Only the centered ions pass through the diaphragm (6) in figure 3.2, and can be detected by MCP, see figure 2.12. The diaphragm diameter, the buffer gas pressure, amplitudes and time duration of the RF signals define the mass resolving power of the purification trap. The mass spectrum is obtained by repeating the purification cycle at different cyclotron frequencies ν_c, while other parameters remains constant.

A typical dependence of the MCP's count rate on the cyclotron frequency ν_c of the quadrupole field, is shown in figure 3.5(b). It represents the mass spectrum collected for the isobaric chain $A = 121$. The typical mass resolving power of the method is about $m/\Delta m \sim 10^5$, which is usually sufficient to obviously separate nuclides of the same isobaric chain or sometimes even isomeric and ground states. Nevertheless, there are some cases, where higher mass resolving power is needed. Mainly it happens near the valley of beta stability. For example, stable ^{121}Sb and radioactive ^{121}Sn have a quadrupole frequency difference of 3.2 Hz, see figure 3.5(b). To distinguish them the mass resolving power has to be improved about three times. A high-resolution cleaning technique can be employed for this purposes [117, 110]. This method has been already used at JYFLTRAP for the beam purification, but its implementation for the independent yield measurements requires further study.

In priciple, the combination of IGISOL and Penning trap techniques is a universal method to measure independent fission yields. However, in practice, gas impurities and charge exchange reactions complicate the absolute independent yield determination. To get around chemical effects relative measurements were performed instead.

It is assumed that different isotopes of the same element have equal chemical properties and thus ion losses due to chemical reactions do not depend on the isotope mass numbers. As a result, the isotopic fission yield distributions were measured by

this method relative to the yield of a reference isotope. For an optimal reference it is required that the mass peak is completely separated from other elements and isomeric states, the half-life of the reference isotope should be well known and its yield should be close to the maximum of the isotopic yield distribution. In the case of several references obtained distributions were scaled to reconstruct the whole isotopic yield distributions.

The IGISOL facility was tuned to select the isobaric chain A_{ref} containing the reference isotope and JYFLTRAP was set to scan a frequency range across all elements of the chain. The same settings were prepared for a measured isobar A_{mes}. An automatic control provided quick switching between the reference isobar A_{ref} and the measured one A_{mes}. This was used to eliminate uncertainties related to all time dependent instabilities of the setup. Measurements were organized in a way that the reference mass spectrum was collected for a few times scanning the quadrupole frequency. This took several minutes. Then the targeted mass spectrum was accumulated during the few scan cycles and the measurement again was switched back to the reference ones. The process was continuing until sufficient statistic was obtained in the peaks of interest. Yield ratios were extracted in the off-line analysis of the measured mass spectra.

3.3 Data analysis

Mass spectra of the targeted A_{mes} and the reference A_{ref} isobars were stored event by event. Each event includes a global time stamp, quadrupole frequency of the RF generator, time-of-flight (TOF) of ions and number of counts registered by MCP. TOF is determined between the signal to extract ions from the trap and the MCP signal.

A cyclotron frequency calibration together with atomic masses taken from the mass evaluation [54] allowed identification of the mass peaks.

In principle, all ions extracted from the purification trap have the same energy and thus their TOF depends on the mass. In practice, the detected ions of the same isobaric chain A form one main peak in the time-of-flight distribution. This peak is used to reduce random noise of the MCP detector. Figure 3.5(a) contains the TOF distribution obtained for the A=121 isobar. Shaded area between dashed lines is a TOF gate, which is applied to the events. The mass spectrum of the sorted events is shown with the shaded histogram in figure 3.5(b). The unshaded histogram represents raw data. The difference between raw and sorted data corresponds to the background and which is shown in figure 3.5(c).

The number of counts in a mass peak was used to determine the ion intensity of nuclides after the trap. One can see from figure 3.5(b) that sorting data within the TOF condition is an efficient way to reduce background. As a result, the background subtraction is not needed in futher data analysis. In these experiments one cycle,

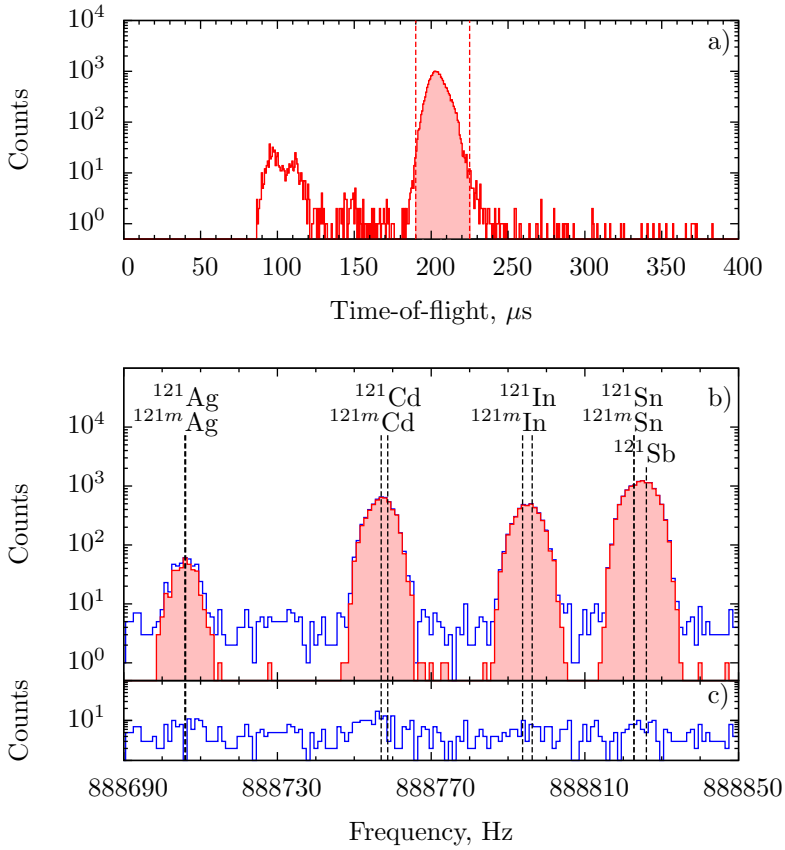

Figure 3.5: Background reduction by sorting data with time-of-flight gates. a) TOF spectrum with gates (shaded area between dashed lines). b) Quadrupole frequency spectra of the $A = 121$ isobaric chain. Shaded histogram represents data sorted with the TOF condition and unshaded histogram refers to raw data. c) Background spectrum obtained as a difference between raw and sorted data.

from production of radioactive nuclides in fission until they were registered by the MCP, took about 400–900 ms. For some short-lived species this time is comparable with their half-life. That is the reason why a radioactive decay loss correction was applied to the ion intensities. The independent fission yields were obtained from the corrected intensities.

The most time consuming stages between production and detection are the col-

lection of ions in the RFQ cooler and their separation in the Penning trap. It is assumed that ions are accumulated in the cooler during t_c with the constant production rate N_0/t_c, where N_0 is the number of ions extracted from the ion guide. After a bunch of ions is released from the RFQ cooler only ions whose decay happens in the trap are lost. Equation 3.6 is used to correct the number of ions N, detected by the MCP,

$$N_0 = N \times \psi(\lambda, t_c, T_t) \tag{3.6}$$

with correction function

$$\psi(\lambda, t_c, T_t) = \frac{\lambda t_c}{(1 - e^{-\lambda t_c})e^{-\lambda T_t}}, \tag{3.7}$$

where λ is the decay constant of the nuclide, t_c is time in the cooler and T_t is the time in the Penning trap. It is important to note that the population of daughter nuclei via β-decay, taking place in the RFQ cooler and in the trap, is not included in the data analysis. The main reason is that the ions after the β-decay obtain the charge state 2^+ and their frequencies differ from ones given by equation 3.4. Thus such ions are separated by the Penning trap and do not impact to the intensity of mass peaks of 1^+ ions.

The uncertainty of corrected mass peak intensities $\Delta N_0/N_0$ is given by equation:

$$\frac{\Delta N_0}{N_0} = \sqrt{\left(\frac{\Delta N}{N}\right)^2 + \left(\frac{\Delta\psi(\lambda)}{\psi(\lambda)}\right)^2}, \tag{3.8}$$

here $\psi(\lambda)$ is defined by equation 3.7, but the single argument λ emphasizes that the correction function's uncertainty depends only on the half-life of a nuclide and its uncertainty. According to [60] the correction function's uncertainty is approximated by symmetric intervals relative to the average value and is calculated as follows:

$$\Delta\psi(\lambda) = \psi(\lambda - \Delta\lambda) - \psi(\lambda), \tag{3.9}$$

where $\Delta\lambda$ is uncertainty of the half-life λ. Both values λ and $\Delta\lambda$ are calculated from half-lives taken from the evaluation of nuclear properties [54].

Another type of yield corrections is related to unresolvable mass peaks. Unresolvable mass peaks can contain different elements or an isomeric and ground states of a same element. The first case usually happens for nuclides close to the beta stability line, where the mass difference between nuclides is relatively small. These cases are individually discussed together with the independent yields further in the text.

When an isomeric and ground states can not be resolved different half-lives of isomeric and ground state lead to different decay corrections. The correction is bigger for shorter half-lives and smaller for longer ones. In this case the independent yield is calculated for two ultimate situations: when all events in the peak are associated

with the ground state and then with the isomeric state. The resultant yield equals the average of the calculated values. The difference between the average and limit value is added to the total uncertainty as a systematic component. The resulting uncertainty is relatively big in situations, where half-lives of both states are close to the length of the purification cycle and half-lives significantly differ from each other.

Some yield distributions were measured with respect to several reference isotopes. In such cases overlapping yields have to behave in a similar way. They only differ by a scaling factor. To normalize both sets the scaling factor is calculated as an average of the individual scales of overlapped yields. After such normalization a weighted average yield is calculated for the overlapped yields. The same normalization procedure is used to obtain final yields from the data measured at the IGISOL–3 and IGISOL–4 facilities.

3.4 Independent yields in the p-induced fission of ^{232}Th

The independent yields measured in two experiments (April 2010, IGISOL–3 and April 2014, IGISOL–4) on 25 MeV proton-induced fission of ^{232}Th are summarized in tables 3.1–3.26. Results are presented as isotopic yield distribution of a given chemical elements. All yields are given as a fraction of the reference isotope's yield. The yield of a reference isotope is equal to 1.0 with an uncertainty calculated according to equation 3.8, in case of a single reference and equals to a weighted average with appropriate uncertainty, if yields were obtained relative to different references.

Experimental data cover the range of nuclear charges from Z=32 (germanium) to Z=57 (lanthanum). Some isotopic distributions were measured only at the IGISOL–3 facility and some of them only at IGISOL–4. In principle, the ion counting technique allows measurement of the fission yields of long lived and even stable nuclides. Some stable isotopes can be produced directly in the fission. However, in the last experiments at IGISOL–4 it was found that there are stable isotopes, which come from another sources. For example, mass peaks of ^{116}Sn, ^{118}Sn, ^{119}Sn and ^{120}Sn isotopes are clearly separated (mass peak of ^{117}Sn can contain tiny amount of events related to ^{117}In and ^{117m}In) and their measured yields nicely follow a natural abundance pattern, see figure 3.6. The vertical axis represents the relative yields of stable Sn isotopes per 1 % of their natural abundances. Isotopes ^{116}Sn–^{120}Sn have the same ratios, whereas for ^{122}Sn and ^{124}Sn the ratios deviate from this value. It can be explained by the production of those iostopes directly in the fission. In addition, mass peaks of ^{122}Sn and ^{124}Sn isotopes can not be clearly separated from ^{122}Sb, ^{122}Te and ^{124}Sb, respectively.

The stable isotopes of one element can seriously disturb the isotopic distributions of other elements. It is supposed that the huge amount of stable ions creates a space charge in the Penning trap. Due to the space charge the operation of the Penning trap becomes unstable and obtained yields strongly depend on settings of

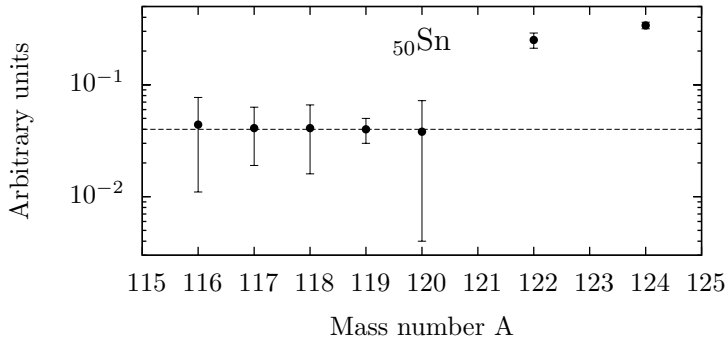

Figure 3.6: Yields of stable Sn isotopes. A ratio of the relative yields of stable Sn isotopes to their natural abundances is plotted on the vertical axis.

the trap. The space charge affects the whole isobaric chain injected in the trap and usually reduces yields. Thus such an effect should be visible in isotopic distributions of different elements. For example, the yields of germanium and arsenic isotopes with mass numbers A=79 and 81 are reduced compare to yields obtained from the gaussian fits. This can happen due to presence of the ^{79}Br and ^{81}Br stable isotopes. A similar effect was observed in experiments at IGISOL–4 on proton-induced fission of natural uranium [118].

The origin of all stable nuclides is not clearly understood yet. To be visible in mass spectra an atoms of the stable nuclides has to be ionized and pass several separator's stages. In principle, the fraction of yields related to natural abundance can be subtracted from the measured values. All cases, which deviate from a gaussian approximation and require further detailed analysis, are commented in the tables below. Some mass peaks were so close that it was possible to resolve them only by a fit. This fit procedure impacts to the total uncertainty of the yield, but it was not included in the present data analysis. General estimations allow to conclude that all measured yields are a proiri precise to the 12 % level.

Germanium and Arsenic

As was mentioned above the yields of ^{79}Ge and ^{81}Ge are reduced compare to the gaussian fit. Also these values from the IGISOL–4 measurements are almost two times larger than those obtained at IGISOL–3. In the experiment at IGISOL–4 the reference was ^{80}Ge and data were normalized to it. It is not clear why the yield of ^{82}Ge in the IGISOL–4 experiment is only half of the yield from IGISOL–3. The yields of ^{79}As, ^{81}As and ^{82}As behave very similar to the corresponding isotopes of germanium.

Table 3.1: Relative isotopic yields of $_{32}$Ge.

Nuclide	Yield	IGISOL–3 yield	IGISOL–4 yield	Comments
^{76}Ge	0.166±0.010	0.166±0.010		
^{77}Ge	0.644±0.034	0.644±0.034		
^{78}Ge	1.655±0.058	1.655±0.058		
^{79}Ge	1.101±0.050	1.034±0.052	2.104±0.202	Reduced by ^{79}Br.
^{80}Ge	3.161±0.087	3.161±0.136	3.161±0.113	
^{81}Ge	1.025±0.034	1.000±0.035	1.876±0.201	Reduced by ^{81}Br.
^{82}Ge	1.980±0.084	2.118±0.091	1.144±0.223	Need to check.
^{83}Ge	0.509±0.029	0.509±0.029		
^{84}Ge	0.057±0.010	0.057±0.010		

Table 3.2: Relative isotopic yields of $_{33}$As.

Nuclide	Yield	IGISOL–3 yield	IGISOL–4 yield	Comments
^{78}As	0.062±0.006	0.062±0.006		
^{79}As	0.117±0.011	0.114±0.011	0.376±0.104	Reduced by ^{79}Br.
^{80}As	0.937±0.034	0.937±0.043	0.937±0.056	
^{81}As	1.145±0.026	1.000±0.028	1.999±0.068	Reduced by ^{81}Br.
^{82}As	3.280±0.061	5.638±0.196	3.027±0.064	Need to check.
^{83}As	5.584±0.165	5.584±0.165		
^{84}As	2.201±1.105	2.201±1.105		
^{85}As	0.283±0.011	0.283±0.011		
^{86}As	0.093±0.011	0.093±0.011		

Selenium and Bromine

^{80}Se and ^{82}Se are stable isotopes with natural abundances of 49.9 and 8.9 %, respectively. In principle, the yield of ^{82}Se isotope produced in fission can be obtained by a subtraction of the natural component. The yield of ^{85}Se is lower than the gaussian fit would suggest. From the another side, the yield of ^{85}Br is in the right position. This case has to be analysed more carefully. The bromine isotopic distribution has been measured only at IGISOL–3.

Table 3.3: Relative isotopic yields of $_{34}$Se.

Nuclide	Yield	IGISOL–3 yield	IGISOL–4 yield	Comments
^{80}Se	0.891 ± 0.013		0.891 ± 0.013	Stable (49.9 %).
^{81}Se	0.059 ± 0.004		0.059 ± 0.004	
^{82}Se	0.324 ± 0.009	0.324 ± 0.330	0.324 ± 0.009	Stable (8.9 %).
^{83}Se	0.964 ± 0.013	0.964 ± 0.013		
^{84}Se	1.385 ± 0.018	1.385 ± 0.018		
^{85}Se	1.000 ± 0.013	1.000 ± 0.013		Need to check.
^{86}Se	0.764 ± 0.009	0.764 ± 0.009		
^{87}Se	0.308 ± 0.007	0.308 ± 0.007		
^{88}Se	0.104 ± 0.004	0.104 ± 0.004		

Table 3.4: Relative isotopic yields of $_{35}$Br.

Nuclide	Yield	IGISOL–3 yield	IGISOL–4 yield	Comments
^{82}Br	0.312±0.317	0.312±0.317		Contain ^{82}Se.
^{83}Br	0.100±0.003	0.100±0.003		
^{84}Br	0.342±0.007	0.342±0.007		
^{85}Br	1.006±0.010	1.006±0.010		
^{86}Br	1.463±0.011	1.463±0.011		
^{87}Br	1.574±0.015	1.574±0.015		
^{88}Br	1.165±0.008	1.165±0.008		
^{89}Br	0.303±0.004	0.303±0.004		Reduced by ^{89}Y.
^{90}Br	0.166±0.005	0.166±0.005		
^{91}Br	0.041±0.002	0.041±0.002		

Krypton and Rubidium

Both isotopic distributions were measured only at the IGISOL–3 facility. One can clearly see that the yield of ^{89}Kr significantly differs from the yields of the gaussian fit. The same reduction is present for ^{89}Br, see table 3.4. In addition, a similar effect was observed in the experiment on proton-induced fission of uranium [118]. One possible reason could be that the yields are suppressed by stable ^{89}Y via the space charge effect in the Penning trap.

The nature of the enhanced yield of ^{96}Rb is not understood and requires an additional analysis.

Table 3.5: Relative isotopic yields of $_{36}$Kr.

Nuclide	Yield	IGISOL–3 yield	IGISOL–4 yield	Comments
^{86}Kr	0.255±0.006	0.255±0.006		
^{87}Kr	0.529±0.010	0.529±0.010		
^{88}Kr	1.000±0.010	1.000±0.010		
^{89}Kr	0.446±0.008	0.446±0.008		Reduced by ^{89}Y.
^{90}Kr	0.879±0.014	0.879±0.014		
^{91}Kr	0.459±0.006	0.459±0.006		
^{92}Kr	0.203±0.005	0.203±0.005		

Table 3.6: Relative isotopic yields of $_{37}$Rb.

Nuclide	Yield	IGISOL–3 yield	IGISOL–4 yield	Comments
^{89}Rb	0.395±0.006	0.395±0.006		
^{90}Rb	0.678±0.008	0.678±0.008		
^{91}Rb	0.633±0.006	0.633±0.006		
^{92}Rb	1.000±0.010	1.000±0.010		
^{93}Rb	0.863±0.011	0.863±0.011		
^{94}Rb	0.422±0.008	0.422±0.008		
^{95}Rb	0.188±0.006	0.188±0.006		
^{96}Rb	0.644±0.031	0.644±0.031		Need to check.
^{97}Rb	0.044±0.006	0.044±0.006		

Strontium and Yttrium

The isotopic distributions of strontium and yttrium were measured only at IGISOL–3. The yield of ^{96}Y includes yields of the ground and isomeric states with the energy difference of $\Delta E = 1.140$ MeV [119]. The mass resolving power of the purification trap was sufficient to separate them and measure yields independently. The isomeric yield ratio obtained for ^{96}Y is $R(\mathrm{Y}_{i.s.}/\mathrm{Y}_{g.s.}) = 0.66 \pm 0.02$.

Table 3.7: Relative isotopic yields of $_{38}$Sr.

Nuclide	Yield	IGISOL–3 yield	IGISOL–4 yield	Comments
^{89}Sr	0.025±0.002	0.025±0.002		
^{90}Sr	0.120±0.004	0.120±0.004		
^{91}Sr	0.416±0.008	0.416±0.008		
^{92}Sr	1.000±0.014	1.000±0.014		
^{93}Sr	1.419±0.022	1.419±0.022		
^{94}Sr	1.723±0.020	1.723±0.020		
^{95}Sr	1.535±0.016	1.535±0.016		
^{96}Sr	1.148±0.021	1.148±0.021		
^{97}Sr	0.561±0.019	0.561±0.019		
^{98}Sr	0.222±0.009	0.222±0.009		
^{99}Sr	0.037±0.006	0.037±0.006		

Table 3.8: Relative isotopic yields of $_{39}$Y.

Nuclide	Yield	IGISOL–3 yield	IGISOL–4 yield	Comments
^{94}Y	0.539±0.010	0.539±0.010		
^{95}Y	1.000±0.014	1.000±0.014		
^{96}Y	1.409±0.022	1.409±0.022		
^{97}Y	1.449±0.030	1.449±0.030		
^{98}Y	0.834±0.179	0.834±0.179		
^{99}Y	0.690±0.018	0.690±0.018		
^{100}Y	0.279±0.089	0.279±0.089		
^{101}Y	0.108±0.034	0.108±0.034		
^{102}Y	0.016±0.007	0.016±0.007		

Zirconium and Niobium

Mass number A=99 was skipped accidentally and thus there are no measured values for ^{99}Zr and ^{99}Nb isotopes.

Table 3.9: Relative isotopic yields of $_{40}$Zr.

Nuclide	Yield	IGISOL–3 yield	IGISOL–4 yield	Comments
^{94}Zr	0.022±0.001	0.022±0.001		
^{95}Zr	0.063±0.002	0.063±0.002		
^{96}Zr	0.245±0.005	0.245±0.005		
^{97}Zr	0.459±0.007	0.459±0.007		
^{98}Zr	1.000±0.012	1.000±0.012		
^{99}Zr				Not measured.
^{100}Zr	1.216±0.015	1.194±0.022	1.239±0.022	
^{101}Zr	0.783±0.010	0.782±0.017	0.784±0.012	
^{102}Zr	0.444±0.007	0.444±0.008	0.446±0.010	
^{103}Zr	0.137±0.004	0.139±0.005	0.133±0.007	
^{104}Zr	0.035±0.002		0.035±0.002	
^{105}Zr	0.007±0.001		0.007±0.001	

Table 3.10: Relative isotopic yields of $_{41}$Nb.

Nuclide	Yield	IGISOL–3 yield	IGISOL–4 yield	Comments
^{96}Nb	0.205±0.021	0.205±0.021		
^{97}Nb	0.020±0.002	0.020±0.002		
^{98}Nb	0.115±0.013	0.115±0.013		
^{99}Nb				Not measured.
^{100}Nb	0.612±0.059	0.612±0.059		
^{101}Nb	1.000±0.012	1.000±0.012		
^{102}Nb	1.141±0.201	1.141±0.201		
^{103}Nb	1.112±0.053	1.112±0.053		
^{104}Nb	0.599±0.046	0.532±0.110	0.613±0.051	
^{105}Nb	0.390±0.006	0.392±0.006	0.346±0.030	
^{106}Nb	0.092±0.018		0.092±0.018	

Molybdenum and Technetium

Masses lower than A=104 were not measured at IGISOL–4. At IGISOL–3 isotopes of molybdenum and technetium were out of the scanning frequency range. The yield of ^{106}Tc is reduced and require additional analysis. The experiment with the uranium target also shows a reduced yield of ^{106}Tc [118].

Table 3.11: Relative isotopic yields of $_{42}$Mo.

Nuclide	Yield	IGISOL–3 yield	IGISOL–4 yield	Comments
^{104}Mo	1.000±0.020		1.000±0.020	
^{105}Mo	0.929±0.018		0.929±0.018	
^{106}Mo	0.655±0.020		0.655±0.020	
^{107}Mo	0.311±0.012		0.311±0.012	
^{108}Mo	0.103±0.006		0.103±0.006	
^{109}Mo	0.025±0.004		0.025±0.004	

Table 3.12: Relative isotopic yields of $_{43}$Tc.

Nuclide	Yield	IGISOL–3 yield	IGISOL–4 yield	Comments
^{104}Tc	0.177±0.009		0.177±0.009	
^{105}Tc	0.522±0.022		0.522±0.022	
^{106}Tc	0.551±0.022		0.551±0.022	Need to check.
^{107}Tc	1.385±0.047		1.385±0.047	
^{108}Tc	1.001±0.028		1.001±0.028	
^{109}Tc	0.712±0.030		0.712±0.030	

Ruthenium and Rhodium

Rhodium isotopes were measured only at IGISOL–3 and their distribution is well approximated by the Gaussian function. However, the yields of ruthenium scatters around the gaussian fit. Also the difference between yields of the ^{108}Ru and ^{109}Ru isotopes changes from the measurements at IGISOL–3 to IGISOL–4. The majority of the ruthenium peaks are well separated in mass spectra and this fact confuses the situation more. Yields are presented as measured, but a more careful analysis of the raw data has to be done.

Table 3.13: Relative isotopic yields of $_{44}$Ru.

Nuclide	Yield	IGISOL–3 yield	IGISOL–4 yield	Comments
^{106}Ru	1.209±0.064		1.209±0.064	
^{107}Ru	0.759±0.051		0.759±0.051	
^{108}Ru	2.075±0.042	2.285±0.054	1.771±0.066	
^{109}Ru	1.973±0.049	1.871±0.053	2.637±0.135	
^{110}Ru	2.262±0.060	2.262±0.060		
^{111}Ru	2.109±0.074	2.109±0.074		
^{112}Ru	1.000±0.027	1.000±0.027		
^{113}Ru	0.365±0.082	0.365±0.082		
^{114}Ru	0.098±0.006	0.098±0.006		

Table 3.14: Relative isotopic yields of $_{45}$Rh.

Nuclide	Yield	IGISOL–3 yield	IGISOL–4 yield	Comments
^{108}Rh	0.056±0.004	0.056±0.004		
^{109}Rh	0.190±0.012	0.190±0.012		
^{110}Rh	0.490±0.028	0.490±0.028		
^{111}Rh	0.918±0.028	0.918±0.028		
^{112}Rh	1.000±0.043	1.000±0.043		
^{113}Rh	0.905±0.028	0.905±0.028		
^{114}Rh	0.560±0.023	0.560±0.023		
^{115}Rh	0.377±0.012	0.377±0.012		
^{116}Rh	0.139±0.013	0.139±0.013		

Palladium and Silver

It should be noted that ^{113}Pd has a ground state with a half-life of 93 ± 5 s and an isometic state with an energy difference of 81.1 keV and half-life 0.3±0.1 s [120]. The purification cycle of 0.86 s was longer than the half-life. It was assumed that after purification only ions of ^{113}Pd in their ground state can be detected. Thus the yield of ^{113}Pd refers to ions in the ground state. Large error bars of the ^{116}Pd yield are due to statistical uncertainty of ^{118}Pd, which was a reference. Silver isotopes were measured in both experiments and there is no contradiction between the overlapping values.

Table 3.15: Relative isotopic yields of $_{46}$Pd.

Nuclide	Yield	IGISOL–3 yield	IGISOL–4 yield	Comments
^{110}Pd	0.034±0.002	0.034±0.002		
^{111}Pd	0.184±0.005	0.184±0.005		
^{112}Pd	0.398±0.009	0.398±0.009		
^{113}Pd	0.710±0.013	0.710±0.013		
^{114}Pd	0.915±0.023	0.915±0.023		
^{115}Pd	1.000±0.022	1.000±0.022		
^{116}Pd	0.904±0.090		0.904±0.090	
^{117}Pd	0.376±0.009	0.376±0.009	0.376±0.042	
^{118}Pd	0.149±0.014		0.149±0.014	
^{119}Pd	0.045±0.008		0.045±0.008	

Table 3.16: Relative isotopic yields of $_{47}$Ag.

Nuclide	Yield	IGISOL–3 yield	IGISOL–4 yield	Comments
^{113}Ag	0.159±0.005	0.159±0.005		
^{114}Ag	0.360±0.014	0.360±0.014		
^{115}Ag	1.000±0.028	1.000±0.028		
^{116}Ag	1.581±0.043	1.625±0.053	1.495±0.074	
^{117}Ag	2.045±0.066	1.973±0.084	2.160±0.106	
^{118}Ag	1.584±0.055		1.584±0.055	
^{119}Ag	0.897±0.042		0.897±0.042	
^{120}Ag	0.414±0.045		0.414±0.045	
^{121}Ag	0.168±0.031		0.168±0.031	

Cadmium and Indium

The yields of cadmium and indium were measured at the IGISOL–4 facility. The yields of Cd are well approximated by the gaussian function. ^{118}In could not be separated from ^{118}Sn, which is stable. From the whole isotopic distribution of In it is possible to assume that the yield ^{118}In is negligible.

Table 3.17: Relative isotopic yields of $_{48}$Cd.

Nuclide	Yield	IGISOL–3 yield	IGISOL–4 yield	Comments
^{117}Cd	0.458±0.024		0.458±0.024	
^{118}Cd	0.948±0.015		0.948±0.015	
^{119}Cd	1.344±0.016		1.344±0.016	
^{120}Cd	1.370±0.022		1.370±0.022	
^{121}Cd	1.043±0.022		1.043±0.022	
^{122}Cd	0.614±0.031		0.614±0.031	
^{123}Cd	0.262±0.009		0.262±0.009	
^{124}Cd	0.105±0.004		0.105±0.004	
^{125}Cd	0.022±0.002		0.022±0.002	
^{126}Cd	0.006±0.001		0.006±0.001	

Table 3.18: Relative isotopic yields of $_{49}$In.

Nuclide	Yield	IGISOL–3 yield	IGISOL–4 yield	Comments
^{118}In	0.872±0.034		0.872±0.034	Contains stable ^{118}Sn.
^{119}In	0.154±0.005		0.154±0.005	
^{120}In	0.439±0.018		0.439±0.018	
^{121}In	0.806±0.035		0.806±0.035	
^{122}In	1.216±0.230		1.216±0.230	
^{123}In	1.000±0.047		1.000±0.047	
^{124}In	0.716±0.038		0.716±0.038	
^{125}In	0.408±0.069		0.408±0.069	
^{126}In	0.198±0.031		0.198±0.031	
^{127}In	0.063±0.014		0.063±0.014	
^{128}In	0.024±0.004		0.024±0.004	

Tin

The yields of magic tin isotopes are difficult to measure with the Penning trap. Mass difference between nuclides is rather small and presence of stable isotopes adds some complications to the data analysis. The yields of tin isotopes were measured only at IGISOL–4. Stable isotopes are marked in the comments and their natural abundance is given in round brackets. One can see in figure 3.6 that the yields of ^{116}Sn–^{120}Sn isotopes nicely follow a pattern of natural abundances. The yields of ^{122}Sn and ^{124}Sn isotopes do not match that pattern, because they are partially produced in fission. The fission yields of those isotopes were obtained by subtraction of the component related to the naturally abundant atoms. In addition, ^{121}Sn and ^{122}Sn can not be resolved from the stable ^{121}Sb and ^{122}Te isotopes, respectively. Mass peaks of ^{123}Sn and ^{123}Sb were so close that only the gaussian fit allowed to distinguish them.

The ground and isomeric states of ^{128}Sn have energy difference of about 2.1 MeV [121]. They were resolved using a purification trap. The isomeric yield ratio obtained for ^{128}Sn is $R(Y_{i.s.}/Y_{g.s.}) = 0.79 \pm 0.03$.

Table 3.19: Relative isotopic yields of $_{50}$Sn.

Nuclide	Yield	IGISOL–3 yield	IGISOL–4 yield	Comments
^{121}Sn	6.972±0.146		6.972±0.146	Contains ^{121}Sb.
^{122}Sn	0.973±0.033		1.163±0.039	Stable (4.63 %) & Contain ^{122}Te.
^{123}Sn	1.193±0.028		1.193±0.028	Contains ^{123}Sb.
^{124}Sn	1.723±0.020		1.960±0.023	Stable (5.79 %).
^{125}Sn	1.717±0.023		1.717±0.023	
^{126}Sn	2.420±0.033		2.420±0.033	Contains ^{126}Sb.
^{127}Sn	1.552±0.026		1.552±0.026	
^{128}Sn	0.994±0.011		0.994±0.011	
^{129}Sn	0.583±0.012		0.583±0.012	
^{130}Sn	0.333±0.010		0.333±0.010	
^{131}Sn	0.111±0.007		0.111±0.007	
^{132}Sn	0.038±0.004		0.038±0.004	

Antimony

There are two stable antimony isotopes ^{121}Sb and ^{123}Sb with natural abundances 57.21 % and 42.79 %, respectively. It was assumed that ^{121}Sb is not produced in the fission and the fission yield of ^{123}Sb was obtained by subtraction of the fraction of the naturally abundant atoms. ^{122}Sb was included in the mass scan, but no ions were detected. Numbers associated to this isotope represent the upper limit of the yield.

The mass resolving power was enough to separate ground and isomeric states of ^{129}Sb, which have the energy difference of ΔE=1.8513 MeV [122]. The isomeric yield ratio obtained for ^{129}Sb is $R(\mathrm{Y}_{i.s.}/\mathrm{Y}_{g.s.}) = 0.77 \pm 0.02$.

Table 3.20: Relative isotopic yields of $_{51}$Sb.

Nuclide	Yield	IGISOL–3 yield	IGISOL–4 yield	Comments
^{121}Sb			1.575±0.023	Stable (57.21 %).
^{122}Sb	0.012±0.012		0.012±0.012	
^{123}Sb	0.114±0.001		1.292±0.012	Stable (42.79 %).
^{124}Sb	1.336±0.014		1.336±0.014	
^{125}Sb	0.461±0.006		0.461±0.006	
^{126}Sb	1.466±0.017		1.466±0.017	Contains ^{126}Sn.
^{127}Sb	8.472±0.088		8.472±0.088	Contains ^{127}Te & ^{127}I.
^{128}Sb	1.007±0.008		1.007±0.008	
^{129}Sb	1.137±0.013		1.137±0.013	
^{130}Sb	0.906±0.012		0.906±0.012	
^{131}Sb	0.755±0.015		0.755±0.015	
^{132}Sb	0.369±0.010		0.369±0.010	

Tellurium

Unfortunately, tellurium isotopes do not follow the pattern of natural abundances. Thus corrections due to stable isotopes can not be applied. In addition to stable isotopes, mass peaks of ^{127}Te, ^{130}Te and ^{132}Te can not be resolved from isotopes of Sb and I.

Table 3.21: Relative isotopic yields of $_{52}$Te.

Nuclide	Yield	IGISOL–3 yield	IGISOL–4 yield	Comments
^{124}Te	0.007±0.001		0.007±0.001	Stable (4.74 %).
^{125}Te	0.049±0.002		0.049±0.002	Stable (7.07 %).
^{126}Te	0.067±0.002		0.067±0.002	Stable (18.84 %).
^{127}Te	4.271±0.053		4.271±0.053	Contains ^{127}Sb & ^{127}I.
^{128}Te	0.300±0.004		0.300±0.004	Stable (31.74 %).
^{129}Te	0.605±0.011		0.605±0.011	
^{130}Te	1.126±0.012		1.126±0.012	Stable (34.08 %) & Contains ^{130}I.
^{131}Te	1.146±0.015		1.146±0.015	
^{132}Te	1.978±0.024		1.978±0.024	Contains ^{132}I.
^{133}Te	1.000±0.020		1.000±0.020	
^{134}Te	0.590±0.021		0.590±0.021	
^{135}Te	0.123±0.005		0.123±0.005	
^{136}Te	0.035±0.003		0.035±0.003	

Iodine

Yields of iodine isotopes follow quite well the gaussian fit. The only one exception is ^{132}I, whose mass peak can not be resolved from ^{132}Te.

Table 3.22: Relative isotopic yields of $_{53}$I.

Nuclide	Yield	IGISOL–3 yield	IGISOL–4 yield	Comments
^{131}I	0.414±0.014	0.414±0.014		
^{132}I	1.696±0.041	1.696±0.041		Contains ^{132}Te.
^{133}I	1.000±0.018	1.000±0.018		
^{134}I	0.948±0.011	1.074±0.031	0.931±0.011	
^{135}I	0.769±0.009	1.812±0.027	0.769±0.009	
^{136}I	0.324±0.005	0.308±0.007	0.337±0.006	
^{137}I	0.166±0.003	0.161±0.004	0.172±0.004	
^{138}I	0.048±0.002	0.048±0.002		
^{139}I	0.015±0.001	0.015±0.001		
^{140}I	0.000±0.000	0.000±0.000		

Xenon

Stable isotopes of xenon are present in the buffer gas and this makes the yield determination rather complicated. In addition, peaks of ^{129}Xe and ^{136}Xe can not be distinguished from ^{129}I and ^{136}Cs, respectively. The contribution of naturally occured isotopes to the total yields were estimated with an assumption, that ^{128}Xe was not produced in the fission. Then the yields which are proportional to the natural abundances were calculated for other stable isotopes and subtracted from the total yields. These yields are presented in the "Yields" column of the table. ^{133}Xe was not distinguished from stable ^{133}Cs. However, it was assumed that a contribution due to natural abundance is negligible. The yield of this isotope produced in the fission is also small, if extrapolated from the isotopic distribution of cesium.

Table 3.23: Relative isotopic yields of $_{54}$Xe.

Nuclide	Yield	IGISOL–3 yield	IGISOL–4 yield	Comments
^{128}Xe	0.014±0.001		0.014±0.001	Stable (1.91 %).
^{129}Xe	0.081±0.004		0.275±0.012	Stable (26.4 %) & Contains ^{129}I.
^{130}Xe	0.026±0.001		0.056±0.003	Stable (4.07 %).
^{131}Xe	0.152±0.005	0.316±0.017	0.302±0.015	Stable (21.23 %).
^{132}Xe	0.374±0.016	0.571±0.030	0.571±0.040	Stable (26.91 %).
^{133}Xe	0.673±0.027	0.673±0.027		
^{134}Xe	0.907±0.017	0.979±0.052	0.984±0.019	Stable (10.44 %).
^{135}Xe	1.250±0.013	1.441±0.043	1.230±0.014	
^{136}Xe	1.760±0.017	1.709±0.027	1.926±0.025	Stable (8.86 %) & Contains ^{136}Cs.
^{137}Xe	1.042±0.008	1.000±0.012	1.081±0.011	
^{138}Xe	0.802±0.008	0.882±0.014	0.768±0.009	
^{139}Xe	0.374±0.005	0.358±0.005	0.410±0.008	
^{140}Xe	0.144±0.003	0.144±0.003		
^{141}Xe	0.039±0.002	0.039±0.002		
^{142}Xe	0.010±0.001	0.010±0.001		
^{143}Xe	0.000±0.000	0.000±0.000		

Cesium

The isotopes of cesium with $A < 137$ were not measured in both experiments. The yields of others are well approximated by the gaussian fit.

Table 3.24: Relative isotopic yields of $_{55}$Cs.

Nuclide	Yield	IGISOL–3 yield	IGISOL–4 yield	Comments
^{137}Cs	1.094±0.010	1.000±0.012	1.285±0.017	
^{138}Cs	1.454±0.011	1.333±0.020	1.512±0.014	
^{139}Cs	1.693±0.012	1.651±0.015	1.776±0.021	
^{140}Cs	1.307±0.008	1.286±0.011	1.330±0.011	
^{141}Cs	0.955±0.007	0.966±0.009	0.936±0.012	
^{142}Cs	0.387±0.008	0.387±0.008		
^{143}Cs	0.139±0.003	0.139±0.003		
^{144}Cs	0.020±0.002	0.020±0.002		
^{145}Cs	0.003±0.001	0.003±0.001		

Barium

In the case of barium there are two stable isotopes ^{137}Ba and ^{138}Ba. However, both of them are produced in the fission. Thus a component related to the natural abundance can not be estimated. Mass peaks of all isotopes were well separated in experiments at IGISOL–3 and IGISOL–4. Only the ^{140}Ba isotope was distinguished from ^{140}La by fitting with the fixed positions of both peaks. The frequency difference of these peaks was 6.2 Hz, whereas the full width at half maximim (FWHM) was about 8 Hz. However, intensity of the ^{140}La is expected to be about 100 times less then that of ^{140}Ba.

Table 3.25: Relative isotopic yields of $_{56}$Ba.

Nuclide	Yield	IGISOL–3 yield	IGISOL–4 yield	Comments
^{137}Ba	0.030±0.002		0.030±0.002	Stable (11.23 %).
^{138}Ba	0.167±0.004		0.167±0.004	Stable (71.69 %).
^{139}Ba	0.349±0.005	0.323±0.009	0.359±0.006	
^{140}Ba	0.666±0.006	0.700±0.011	0.648±0.008	
^{141}Ba	0.990±0.014	1.000±0.019	0.980±0.020	
^{142}Ba	1.258±0.017	1.258±0.017		
^{143}Ba	0.795±0.008	0.795±0.008		
^{144}Ba	0.450±0.012	0.450±0.012		
^{145}Ba	0.135±0.006	0.135±0.006		
^{146}Ba	0.058±0.003	0.058±0.003		

Lanthanum

Lanthanum is an element with the highest nuclear charge Z, which was measured in both experiments. The area of the ^{140}La peak was estimated from the gaussian fit, because its mass peak was overlapped with ^{140}Ba.

Table 3.26: Relative isotopic yields of $_{57}$La.

Nuclide	Yield	IGISOL–3 yield	IGISOL–4 yield	Comments
^{140}La	0.145±0.004		0.145±0.004	
^{141}La	0.232±0.011	0.232±0.011	0.232±0.018	
^{142}La	0.479±0.013	0.479±0.013		
^{143}La	0.990±0.015	0.990±0.015		
^{144}La	1.125±0.024	1.125±0.024		
^{145}La	1.029±0.026	1.029±0.026		
^{146}La	0.670±0.023	0.670±0.023		

3.5 Comparison of experimental yields and theoretical calculations

Despite the fact that the measured yields are relative and represent isotopic distributions of individual elements these data contain important parameters of the fission product distributions such as a width and a position of the maximum yield. An absolute yield or cross-section of one isotope allows to normalized the whole distribution and obtain absolute yields of the isotopic chain.

Another method to obtain absolute yields is described below. The idea is based on an unfolding procedure. Measured isotopic distributions have fixed widths and positions of the maximum yields, whereas their amplitudes are unknown. Multiplication of those distributions by some normalization factors and summing over mass numbers should result in the mass distribution. In reverse the normalization coefficients can be determined from known mass and isotopic distributions.

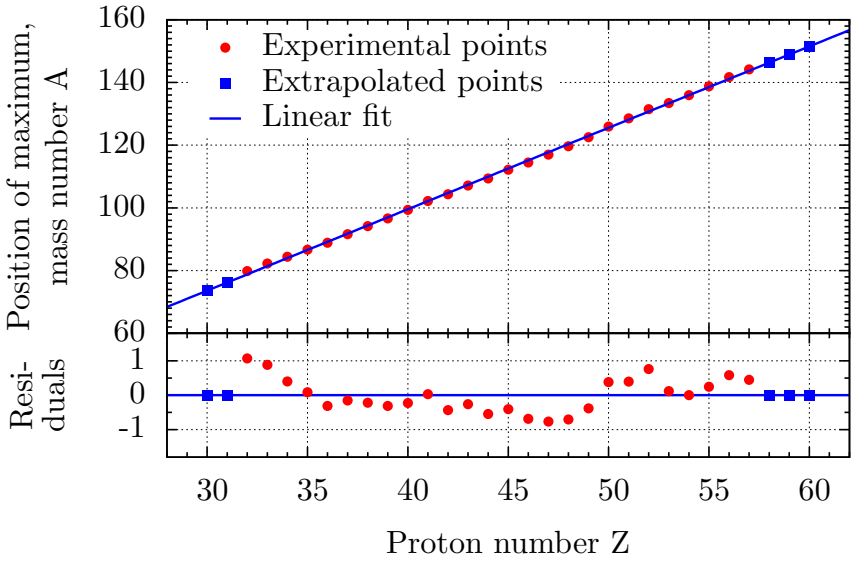

Figure 3.7: Position of an isotopic distribution's maximum as a function of proton number Z. Dots are data taken from fits of experimental points. Solid line is a linear fit, which allows to obtain centroid's positions of extrapolated functions. Extrapolated points are snown by squares.

There are several experimental methods, briefly described in this chapter, which allow the measurement of the mass distributions. A mass distribution of fission

products from the fission of ^{232}Th induced by 25 MeV protons was calculated with the PYF code [123], which is based on systematically analysed experimental data [124, 125]. In that work the $2E$-method was used to study mass and energy distributions of fission products from proton-induced fission of ^{232}Th and ^{238}U at projectile energies of 10.3–30.0 MeV.

The independent fission product yields measured at IGISOL cover intervals of nuclear charges Z =32–57 and mass numbers A =76–146. All suspicious yields commented in the yield tables are not taken into account in this analysis. Experimental values were fitted by the Gaussian functions. Centroids and widths were used to unfold the mass distribution. To reproduce properly the mass distribution nearby edges of the set of experimental gaussian functions have to be expanded. Linear dependence of the maximum's position on proton number Z was used to estimate the centroid's position of the extrapolated functions, see figure 3.7. Widths of extrapolated functions were taken equal to the widths of functions with the lowest and highest Z. The new set of functions cover regions of Z =30–60 and mass numbers A =73–152. The mass distribution was defined in the interval A =75–152.

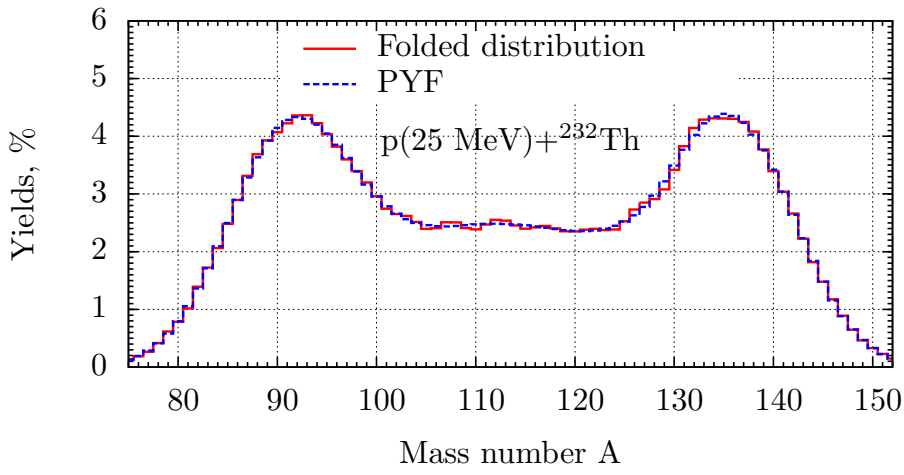

Figure 3.8: Mass distributions of fission products from the p(25 MeV)+^{232}Th reaction after neutron emission. Solid line is a folded distribution and dashed line is an initial distribution calculated with the PYF code. Total sum of yields equals to 200 %.

SPUNIT algorithm, which is typically used to unfold neutron spectra, was applied to obtain the normalization coefficients. The same algorithm was applied to unfold

neutron spectra in Chapter 4 of the present work. The program code based on ROOT libraries [126, 127] was written to process the data. At the beginning of iterations all amplitudes of the gaussian distributions were equal to 1.0. The procedure was stopped, when changes of these amplitudes became less than 1 %.

Sum of all isotopic distributions with adjusted amplitudes at certain mass number has to reproduce the mass distribution. In figure 3.8 one can see that folded mass distribution, solid line, and initial mass distribution, dashed line, calculated with the PYF code [123] are almost identical. As a result, coefficients obtained from such a procedure allows normalization of the experimental data and scaling them to absolute yields. Unfortunately, only mass and energy distributions can be extracted from the PYF code.

Experimentally determined independent fission product yields can be compared with theoretical values calculated using the model described in [40]. The experimental mass distribution and calculated one are shown in figure 3.9. One can see that

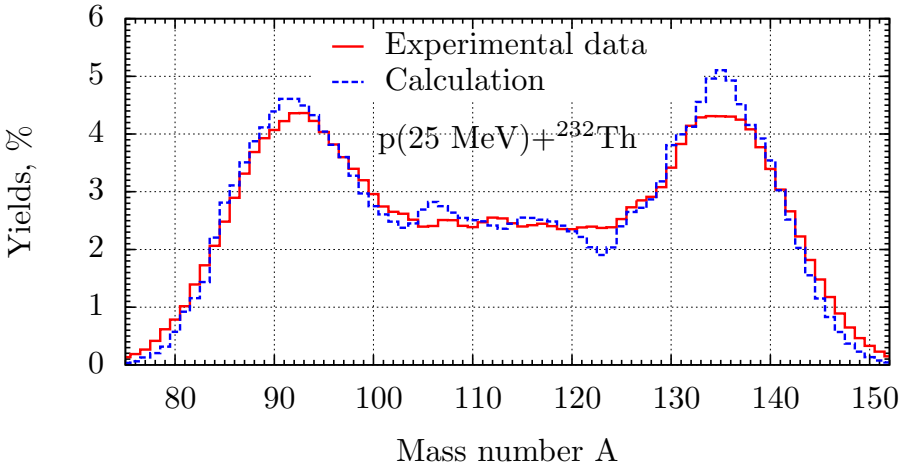

Figure 3.9: Mass distributions of fission products from the p(25 MeV)+^{232}Th reaction. Solid line is an experimental distribution and dashed line is calculated with the FIPRODY code. Both distributions are normalized to 200 %.

the calculation relatively well reproduces the mass distribution. Positions of both asymmetric peaks coincide and yields in the central region have almost the same values.

More detailed comparison of experimental and theoretical independent fission product yields are given in figures 5.2–5.27, which are placed in the Appendix. Ex-

perimental points in figures are real measured values multiplied by factors determined from the unfolding procedure. Squares connected by solid lines are calculated independent fission product yields. Circles are experimental values fitted by the gaussian function, which is shown by a dashed line.

In general, calculated independent yields reproduce measured values relatively well. Absolute values have the same order of magnitude. Only germanium isotopes are exceptions. Their measured yields differ from calculated values almost by factor of three. One possible reason of this can be due to unfolding of the mass distribution. A maximum of the germanium distribution A=80 is situated at the edge of the mass distribution. The isotopic distributions with Z=30 and 31 were extrapolated to properly unfold mass yields. One can see on the residual plot in figure 3.7 that positions of germanium and arsenic maximums have almost one mass unit difference compare to the fit value. It means that Z=30 and 31 distributions are shifted towards light masses. As a result, the normalization coefficient has to be higher to reproduce the mass distribution. Theoretical widths of isotopic distributions in many cases are close to experimental ones. The majority of calculated distributions are shifted towards lower mass numbers, which could be due to an overestimation of evaporated neutrons.

4 Neutron source for IGISOL

The advantages of the neutron-induced fission for production of neutron-rich nuclides have been discussed in section 2.6. To optimise the yield and neutron richness of the fission products, it would be ideal to have a neutron source emitting about 7–8 MeV neutrons within a narrow energy interval. The total fission cross-section reaches a second plateau at these energies (see figure 2.8). In this region, the first-chance fission cross-section has not yet decreased, as it does in higher energies (see figure 2.9). The second-chance fission has a comparable contribution to the total fission cross-section. It means that the second-chance fission has an impact into the total fission cross-section. In addition, less neutrons are emitted in the formation of the compound nucleus than at higher energies, and the relatively low excitation energy of the compound nucleus is not sufficient to evaporate a significant amount of pre-scission neutrons. The 7–8 MeV neutrons are thus close to the optimal compromise between the production cross-section and neutron richness of the products.

To produce a sufficient amount of neutron-rich species the intensity of the source should be as high as possible. Additionally, it is desirable that neutrons are emitted in a narrow cone. The experimental environment provides some constraints which limit the choice of materials, designs and constructions.

In 2010–2013 the IGISOL facility was moved and rebuilt next to the MCC30/15 cyclotron for the purpose to fully employ the intense light ion beams from it. Therefore, the possibility to use MCC30/15 to produce neutrons for fission work and other studies was extensively studied. Main characteristics of the cyclotron are presented in [57]. According to specifications, MCC30/15 is capable of delivering a 18–30 MeV proton beam of 100 μA intensity and the 9–15 MeV deuterons with 50 μA of beam intensity. Internal accelerated beam intensities (i. e. beam inside the cyclotron before extraction) exceeding 140 μA for 30 MeV protons and 60 μA for 15 MeV deuterons have been measured [128]. The beam properties of MCC30/15 constrained the design of the proton-to-neutron converter, which is called the neutron source for short. Additional requirements were vacuum tightness, operation on the high voltage platform and compactness. Also it was important to fully stop the primary beam inside the neutron source.

4.1 Design & Construction

A huge number of neutron sources have been designed and constructed since the discovery of the neutron by James Chadwick in 1932 [129]. In addition to being beta decaying particles with a lifetime of 887.7±1.2[stat]±1.9[syst] s [130], free neutrons cannot be accelerated. There are basically two method for production of energetic neutron beams. Either the neutron beam is produced from the break-up of an accelerated projectile such as deuterium, consisting of a relatively loosely bound neutron, or generated in a nuclear reaction whereby a considerable amount of the energy of the projectile is tranfered to the emitted neutron. Both technniques have been employed at IGISOL in the past [55, 100]

In the prototype development neutron fluxes from a proton and deuteron irradiation of thick targets were compared for various materials. The thick target means that a stopping length of protons and deuterons in the material is equal or less than the thickness of the target. Beryllium (Be) has been chosen as an optimal variant. Heavy elements such as tungsten (W) and lead (Pb) were rejected due to their relatively high Coulomb barrier, which is about ∼20 MeV. This means that only almost half of the initial energy can be utilized for the neutron production. Moreover the neutron flux is smaller than for light materials like lithium (Li) or beryllium. Carbon ^{12}C does not have a high Coulomb barrier, but the threshold for the (p, n) reaction is equal to 19.6 MeV. Elements from the iron region also have smaller neutron flux than in reactions of protons or deuterons with Li or Be. Additionally the long lived radioactive nuclides like ^{60}Co can be produced by neutron activation of such target material. This creates a high activity which remains after irradiation.

From the neutron production point of view ^{7}Li and ^{9}Be have quite similar properties. But their physical properties are completely different. In some cases the low melting point T=180°C of ^{7}Li can be an advantage, for example for high intensity neutron sources with liquid targets [131]. On the contrary ^{9}Be fits better the construction of solid state targets. Also high hardness, good thermal conductivity and low chemical reactivity of beryllium with water make this material ideal for a water cooled neutron source.

The proton beam and the ^{9}Be target has been chosen as a primary combination for the neutron production at IGISOL. The design of the neutron source for the IGISOL facility is based on the construction developed for the Low Energy Neutron Source (LENS) at Indiana University [132].

A schematic view of the IGISOL neutron source is presented in figure 4.1. The primary proton beam (shown by blue arrow) produces neutrons via nuclear reactions within the beryllium target (3). The cooling water is in direct contact with the beryllium target for the most effective transfer of the heat from the target and this allows a high proton beam intensity. A closed cooling system whose water circulation is separated from the main cooling system of the accelerator laboratory provides 7 l/min water flow at 6 bars pressure. This is sufficient to remove a power of 3 kW

created in the neutron source by 30 MeV protons with an intensity of 100 μA. As schematically shown in figure 4.1, the proton beam is allowed to pass the beryllium target (3) and stop in the cooling water (4). The reason for this arrangement is that in [133] it was discovered that high intensity proton beam builds up hydrogen in the target bulk. The diffusion coefficient of hydrogen in beryllium is eight orders of magnitude less than for example in copper. This cause damage of the beryllium material. To avoid this failure projectile particles are stopped in the cooling water.

Positioning the neutron source inside the vacuum chamber is reflected in the design, see figure 4.1. The o-rings (2) are used to seal the water volume (4) from the vacuum both in the cyclotron beam line and the IGISOL vacuum chamber. Direct proton beam interaction with cooling water causes ionization and thus increases its conductivity. Since the neutron source is operated on a 30 kV high voltage platform, the resistivity of the water in the cooling loop has to be maintained. A de-ionizing filter in the cooling water circulation is employed for this purpose.

A 5.0 mm thick beryllium target was chosen to be used in the neutron source prototype with the 30 MeV proton beam. The manufacturing tolerances for the beryllium target are $\pm$0.5 mm. This thickness is enough to slow down protons to 11 MeV, see figure 4.2(a). The dashed line shows energy dependence of protons if it is assumed that after 5 mm they continue to move in beryllium. The solid line has been calculated for the combination of beryllium and water. Figure 4.2(b) represents energy deposition by protons in the different layers. It can be seen from figure 4.2(c)

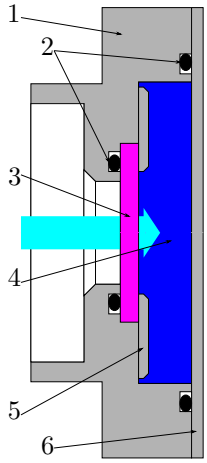

Figure 4.1: The scheme of the IGISOL neutron source. 1 — the main block, 2 — viton o-rings, 3 — beryllium target, 4 — cooling water, 5 — mounting washer, 6 — back flange.

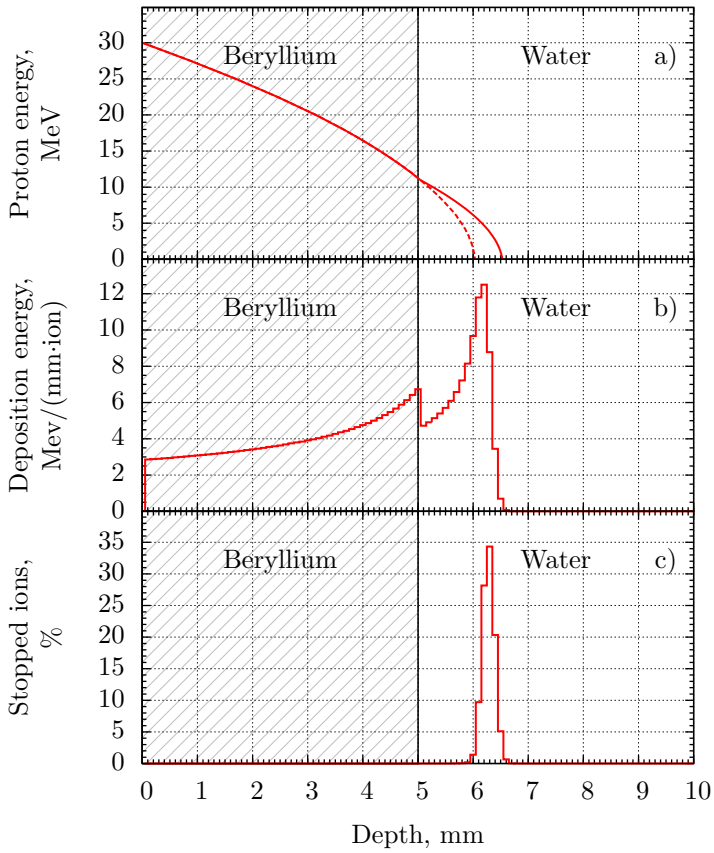

Figure 4.2: Proton distributions with depth in materials of the neutron source: a) is the dependence of the proton energy with the depth of materials; b) — the energy deposited by protons at different distances; c) shows a fraction of protons stopped at certain depth. All distributions have been calculated by the SRIM-2013 code [134].

that almost all protons, which do not have nuclear interactions with beryllium, are stopped in the water.

Protons with energy as high as 11 MeV also cause activation of the cooling water. The main activating nuclear reactions are $^{18}O(p,n)^{18}F$ and $^{14}N(p,\alpha)^{11}C$. The production of these nuclides was confirmed by a half-life analysis of the activity in the cooling water.

The amount of produced activity can be reduced by increasing the beryllium target

thickness so that the energy of the protons entering in the cooling water would be below the contaminating reaction threshold energy of ∼2.5 MeV. This would also optimise the neutron production. Since the threshold energies of the proton-induced reactions producing neutrons on ^{9}Be are 1.8–2.1 MeV, the fraction of energy of the protons leaving the neutron production target at energies higher than that is wasted. The cooling water activation, however, can not be entirely avoided nor the neutron production fully optimised because of the energy straggling of the slowed down protons, which is not shown in figure 4.2.

A clear drawback of the ^{9}Be target at energies above 13 MeV is the production of ^{7}Be via (p,t),(p,nd) and (p,2np) reactions. Threshold energies for these reactions are 13.4 MeV, 20.4 MeV and 22.8 MeV, respectively. Although the total production cross-section does not exceed 10 mbarn at any energy, because of the thick target the production rate of ^{7}Be with 100 μA proton beam is of the order of 10^{11} atoms/second. This will lead to 10 GBq ^{7}Be activity in about 3 days. The 53 day half-life of ^{7}Be is sufficiently short to reduce the activity of the used targets to tolerable level for disposal in 5 years, if the maximum activity is kept below 100 GBq. The most severe issue will clearly be the handling of irradiated targets, for which some kind of remote manipulation needs to be developed.

4.2 On-line test of the source

The first test with the neutron source took place in March of 2014. The main goal of the experiment was to measure energy and angular distributions of neutrons. Additionally it was possible to test the source in real conditions at the IGISOL facility.

The neutron source was installed inside the IGISOL target chamber. A scheme of the experiment is shown in figure 4.3. Space constrains limited choice of techniques suitable for the neutron measurements. The neutron activation method and the time-of-flight technique were employed. For the neutron activation analysis samples of aluminum (Al), nickel (Ni), cobalt (Co), indium (In) and bismuth (Bi) were placed in positions 1–4, see figure 4.3. The size of all samples was 25.0×25.0×1.0 mm.

In the present experiment the proton beam of 30 MeV, blue arrow in figure 4.3, was delivered by the MCC30/15 cyclotron. The neutron converter was electrically insulated and connected to an microamperemeter. The activation of the samples was done at a beam current of 1 μA. The samples were irradiated by neutrons for two and half hours. Figure 4.4 shows the stability of the primary beam on the neutron converter target during that time. Maximum deviation from the average current does not exceed 5%.

The experimental part of the activation method is rather simple: the activation of samples during a certain time period is followed by γ-counting. Then one attempts unfolding the neutron spectrum. While the activation and γ-counting of the samples

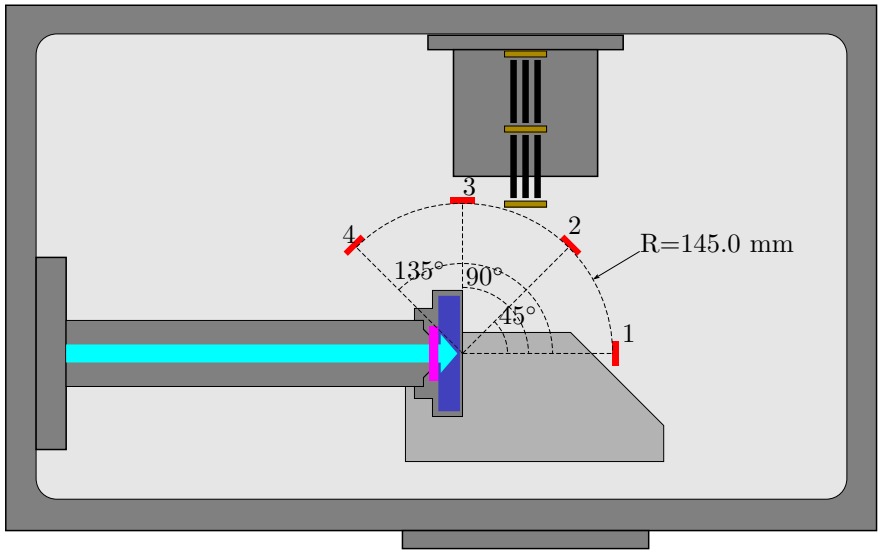

Figure 4.3: A schematic view of the experimental setup for the neutron measurement with the IGISOL neutron source. Activation foils were installed at positions 1–4.

is a straightforward, although a tedious process, the challenge of the measurement is the unfolding procedure. From the mathematical point of view the unfolding procedure is a so-called inverse problem, which does not have an unique solution. References [135, 136] contain detailed review about various unfolding methods, uncertainty analysis and their applications.

After irradiation samples were placed inside the low background lead castle and γ-quanta were registered by a high purity germanium (HPGe) detector. The order in which samples were measured and collection time of γ-spectra were chosen according to the half-lives of nuclides produced in neutron-induced reactions, see table 4.1.

As a result of γ-detection areas of γ-peaks for certain nuclides were obtained. In the general case the area $A(E_\gamma)$ under a peak E_γ is proportional to the integral over the neutron energy interval dE_n of the number of neutrons $dN(E_n)$ passed through the sample per time unit multiplied by a reaction cross-section $\sigma(E_n)$:

$$A(E_\gamma) = C \int \frac{dN(E_n)}{dt} \sigma(E_n) dE_n, \tag{4.1}$$

where C is the proportional coefficient is equal to:

$$C = n \times f(\lambda, T, t, \Delta t) \times b \times \varepsilon \times F_{DAQ}. \tag{4.2}$$

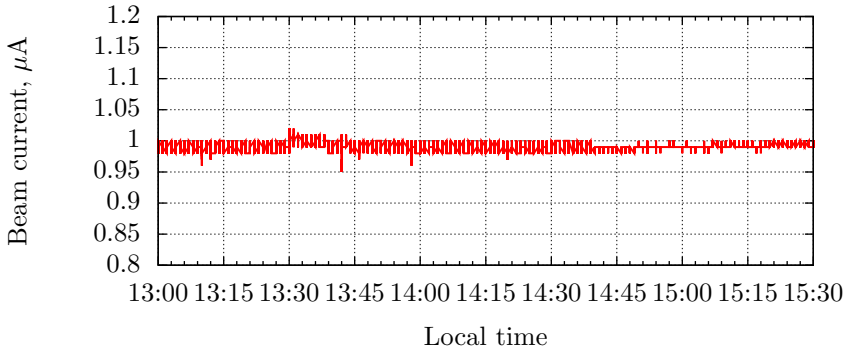

Figure 4.4: Beam current at the neutron converter target during a sample activation.

In equation 4.2 n defines number of atoms in the sample per 1 cm^2. The function $f(\lambda, T, t, \Delta t)$ refers to the fraction of nuclides with the decay constant λ, which are produced during time T and decay during the measurement time $t + \Delta t$. This function is given by equation:

$$f(\lambda, T, t, \Delta t) = \frac{1 - e^{-\lambda T}}{\lambda} e^{-\lambda t}(1 - e^{-\lambda \Delta t}). \tag{4.3}$$

The next multiplier b is the branching ratio of the γ-line E_γ of the nuclide. ε and F_{DAQ} account for the total efficiency of the HPGe detector and dead time of the data acquisition system, respectively.

For practical use it is convenient to replace the integral in equation 4.1 with a sum:

$$A(E_\gamma) = C \sum_i \frac{dN_i(E_n)}{dt} \sigma_i(E_n), \tag{4.4}$$

where i is the index of the certain neutron energy interval. Then $dN_i(E_n)/dt$ is the amount of neutrons with energies in the i^{th}-interval, which pass through an activated sample per time unit.

Reaction cross-sections $\sigma(E_n)$ were extracted from the EXFOR data base [45] and were divided on the same neutron energy intervals. The cross-section data is displayed in figure 4.5.

Equation 4.4 holds for each nuclear reaction used in the activation analysis separately. The equations are connected by the neutron flux that is the same for all targets. The aim of the activation analysis is to determine $dN_i(E_n)/dt$ from the system of equations with measured areas $A(E_\gamma)$ under γ-peaks and calculated coefficients C. This task can be solved by a unfolding procedure.

Table 4.1: Nuclear reactions, which have been accounted to determine neutron flux by the neutron activation method. Column "cross-section plot" refers to figure 4.5

Nuclide in a sample	Nuclear reaction	Product nuclide	$T_{1/2}$, hours	Cross-section plot
^{27}Al	(n, α)	^{24}Na	14.959	a)
^{58}Ni	(n, p)	^{58}Co	1700	b)
	(n, 2n)	^{57}Ni	35.6	c)
^{59}Co	(n, p)	^{59}Fe	1068.1	d)
	(n, 2n)	^{58}Co	1700	e)
	(n, α)	^{56}Mn	2.5785	f)
^{115}In	(n, n')	^{115m}In	4.486	g)
	(n, γ)	^{116m}In	0.905	h)
^{209}Bi	(n, 4n)	^{206}Bi	149.8	i)

In the present experiment 9 nuclear reactions were used to determine the neutron energy spectra. The spectrum was divided into 30 energy intervals with the step 1 MeV. This results in a system of 9 equations with 30 unknown variables which is the reason why it is not complete. To unfold the spectra a code based on the ROOT library [126, 127] was written. The solution of the system is determined by an iterative procedure, which is similar to the SPUNIT algorithm. A description of the method and references to original papers can be found in [135].

The iteration algorithm requires an initial spectrum. A white neutron spectrum in the energy interval from 0 to 30 MeV was used as a starting point. Iterations were stopped when the χ^2 per degree of freedom became close to 1, i.e. $\chi^2/n \approx 1$. The final solution depends on the initial spectrum. In this case it is not clear how to estimate the uncertainty of the result. There is a brief discussion in [136] about the uncertainty analysis for the iteration method, but there is no universal solution. Including uncertainty propagation in iterative algorithms adds extra parameters and makes these methods more complicated. This is the reason why in the present work the uncertainties of the final neutron spectra were not estimated. Nevertheless, the combined uncertainty of the experimentally determined coefficient values $A(E_\gamma)$ and C in the equation 4.4 does not exceed 10–15 %.

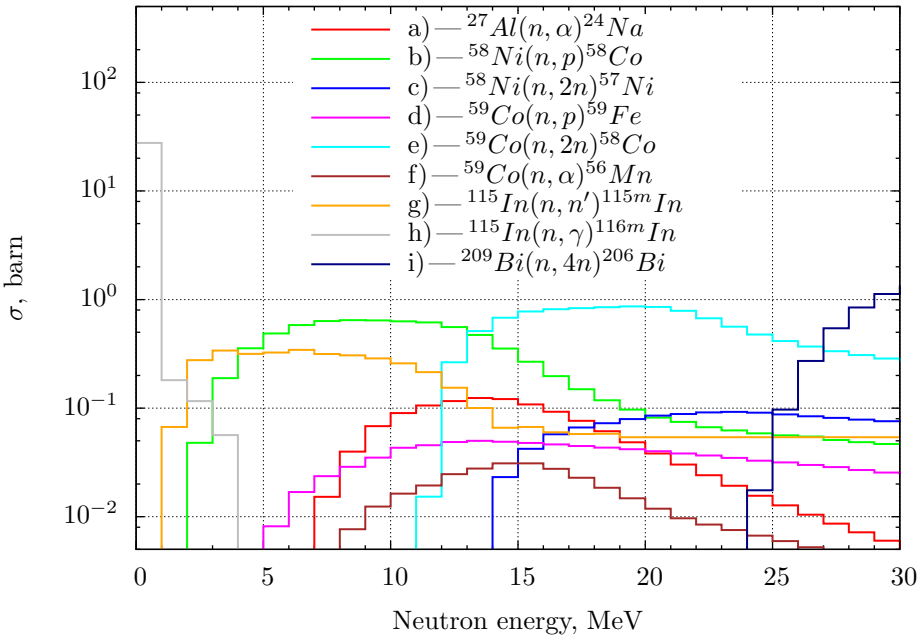

Figure 4.5: Neutron activation cross-sections extracted form the EXFOR data base [45].

4.3 Neutron yield distributions from the source

The neutron spectra from the Be neutron converter, see figure 4.1, were obtained by the activation analysis for 0°, 45°, 90° and 135° angles at the proton energy of 30 MeV. Additionally, the neutron spectra were calculated with the MCNPX code by Dr. Andreas Solders from Uppsala University. Both results are presented in figure 4.6.

In general, one can see relatively good agreement between experimental and calculated spectra for all angles. The main discrepancy exists at the low neutron energy region from 0 to 3 MeV. This can be explained as only one nuclear reaction ^{115}In(n, γ)^{116m}In covers the energy interval. The experimental data from EXFOR about this reaction channel is quite poor. Evaluated cross-sections for the isomeric state ^{116m}In production for example from ENDF or TENDL does not exist. Also the waiting time is very important for this reaction channel due to short half-life of ^{116m}In, which is equal to 0.905 hour. The shortest waiting time was about 1.5 hours.

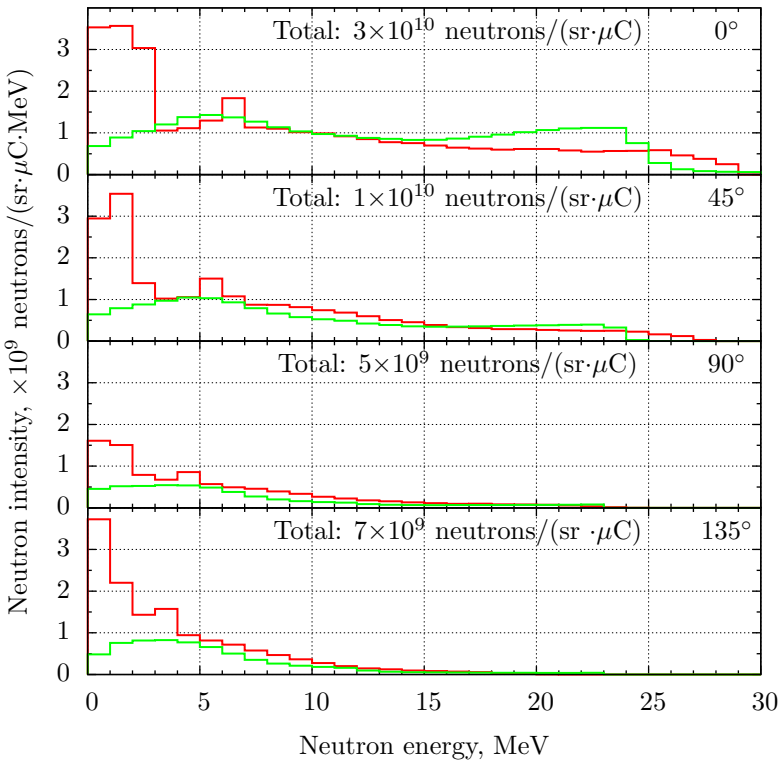

Figure 4.6: Neutron spectra at different angles from the neutron converter, figure 4.1, with the 5 mm thick Be target. Protons of 30 MeV energy were used for neutron production. The red line is calculated with the MCNPX code and green line is measured by the activation method. "Total" means the total number of neutrons summed over the whole spectrum measured by the activation method.

The neutron spectra have an almost constant intensity in the whole neutron energy interval. The reason of such a shape is the thickness of Be target. The thick target means that neutrons are produced by protons of all energies between 0 MeV and the primary beam energy, which is 30 MeV. Such an approach allows to get the maximum neutron intensity to be obtained.

Quasi-monoenergetic neutrons could be produced using a thinner beryllium target. The present construction of the neutron source allows to intall the Be target almost of any thicknesses, if the proton energy is not more than 30 MeV. In addition to the

neutron production, the beryllium target serves as the vacuum window. It separates volumes with the water pressure of 7 bar on one side and vacuum from another side. This condition limits the smallest thickness of the Be material. It might be possible to overcome this problem for example by using a thin beryllium target with a carbon beam stopper behind it, but the heat removal from the target cannot then be solved as efficiently as with a directly water-cooled beryllium target.

A deuteron beam can be utilized for the neutron production as well. Different energy losses of protons and deuterons require an adjustment of the beryllium thickness to properly stop the primary beam in water. The simple construction allows to manufacture several sources designed for certain type of projectile particles and energies.

Experimental measurements of neutron distributions from the thick Li and Be targets with proton and deuteron beams at several projectile energies can be found in [137, 138]. The comparison of the neutron intensities for proton and deuteron reactions on the thick Be target is given in table 4.2.

Table 4.2: The neutron intensities from the thick Be target for proton and deuteron reactions.

Reaction	Energy, MeV	Intensity at 0°, $\times 10^{10}$ neutrons/(sr·μC)	Reference
^{9}Be(p,n)	30	3	present work
	23.0	3.0	[137]
	23.0	2.8	[138]
^{9}Be(d,n)	23.0	11.8	[137]
	23.0	11.6	[138]
	14.8	3.8	[137]

As one can see the intensity measured in the present work is the same as the intensity from work [137], but projectile energies are different. This is due to the thickness of the Be target. In [137] protons and deuterons were fully stopped in the material. In the present work projectile particles pass through the target and enter the water still having 10 MeV of kinetic energy left, see figure 4.2.

The neutron intensity at 0° is ∼4 times higher for the deuteron-induced reaction than for the proton-induced one at the 23.0 MeV projectile energy. However at 14.8 MeV of deuteron energy the neutron intensity becomes almost the same as for 23.0 MeV protons. The comparison of the neutron intensities integrated over certain angles in [137] shows that the deuteron break-up reaction has an impact on the intensity mainly in the forward direction.

To conclude, the neutron source prototype was built and commissioned at the IGISOL facility. The neutron distributions were measured in the on-line experiment with a 30 MeV proton beam. The deduced neutron energy spectra are presented in figure 4.6.

The prototype was designed for a primary beam intensity up to 100 μA or total power 3 kW. Due to technical reasons the neutron source has thus far been tested only up to 10 μA primary beam intensity, i. e. one tenth of the nominal power.

The reaction ^{9}Be(p,n) seems currently to be the optimal solution for the neutron production if the source will be employed together with the MCC30/15 cyclotron [57], because the maximum energy and intensity of the proton beam is two times larger than for that of the deuteron one. On the other hand, the neutron yields measured for ^{9}Be(d,n) in [137] at 15 MeV suggest that the enhancement due to deuteron breakup in the forward angle could make this reaction competitive. In particular, the average energy of the breakup neutrons would be in the favoured energy regime of 7–8 MeV. Another advantage is that the threshold energy for ^{7}Be production via d-induced reactions is 17.5 MeV. ^{7}Be production in the neutron source target is among the most severe radiation protection issues in the beryllium neutron target. The technical challenges however include dealing with thinner beryllium targets due to the lower range of deuterium in beryllium and clearly lower deuterium beam intensities from MCC30/15 cyclotron as compared to proton beams.

4.4 Neutron-induced fission with IGISOL–4

A new ion guide was made to produce a radioactive ion beam of nuclides in the neutron-induced fission of ^{nat}U. It was decided to have a similar construction as the one, which is used in proton-induced fission experiments. To be able to have a meaningful comparison between the performance of the proton-induced and the neutron-induced fission ion guides, the stopping gas volume of the neutron-induced fission ion guide was kept sufficiently similar to that of proton-induced fission ion guide, in about 150 cm^3. The purpose was to minimise the possible impact of the evacuation efficiency to the observed yields.

Another important parameter is the thickness of the fissile target. Typically for proton-induced fission experiments at IGISOL a 14 mg/cm^2 thick natural uranium or thorium target is used. Calculations in [56] show that this thickness is an optimal one. If the target is too thin then fission products entering the gas volume from the target have too high kinetic energy and they are neutralized in interactions with the ion guide walls, if not implanted into them. In the case of a too thick target fission fragments can not escape the target. The ion guide for neutron-induced fission has been equipped with a pair of targets, which are identical to ones for proton-induced fission. The schematic cross-section of the ion guide designed for neutron-induced fission is shown in figure 4.7.

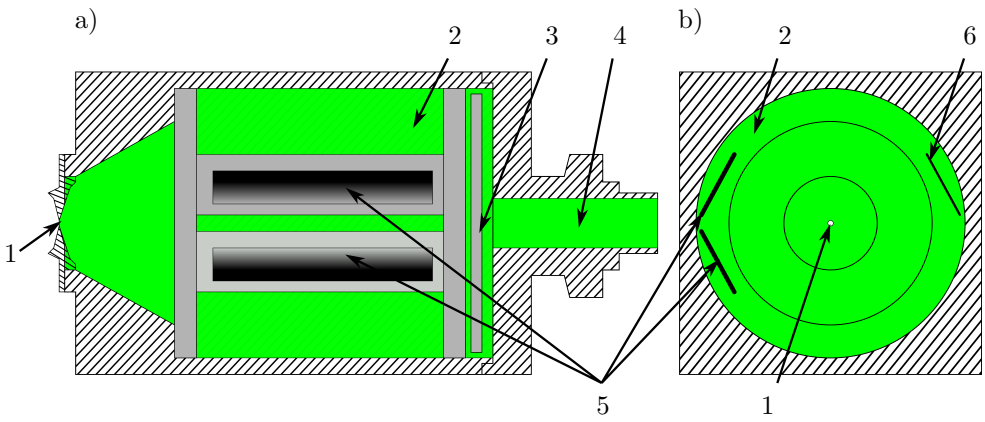

Figure 4.7: Schematic cross-section views of the ion guide designed for the neutron-induced fission: a) is a view from the neutron source side, b) — a view from the He gas inlet channel side. 1 — an extraction nozzle, 2 — He gas volume, 3 — a diffuser, 4 — He gas inlet, 5 — the 14 mg/cm^2 thick ^{nat}U targets, 6 — a Ti collecting foil.

This construction was tested during two short on-line experiments at the IGISOL facility in April and June 2015. The proton beam in both tests was delivered by the K130 cyclotron [139]. The ion guide was installed inside the target chamber as presented in figure 2.14 in both experiments. To maximize the solid angle covered by fissile material the ion guide for neutron-induced fission was equipped with two ^{nat}U targets (5), see figure 4.7, that were placed at one side of the ion guide as close as possible to the neutron source.

During the first experiment the primary proton beam intensity was kept at 1 μA. In this experiment only silicon detector (SiSw) and microchannel plate detector (MCPSw), see figure 2.12, were available to register β-activity and count individual ions. The faraday cup (FC1), see figure 2.12, was used to measure the total ion current extracted from the ion guide. The current of the mass separated ion beam was measured with the switchyard faraday cup (FCSw). An ion beam with a current of several nA was extracted from the ion guide and measured with FC1. After the dipole magnet (5) the current of the mass selected beam was less than one pA, but ions could be detected by a MCP detector. Beta particle counting with a silicon detector (SiSw) showed a rate that was less than one count per second above the background. The beam intensity was so low that it was impossible to obtain any beam further than the switchyard (6). In particular the low intensity, even of the stable ion beams, did not allow the beam to reach the spectroscopy setup (12).

An aluminum foil was installed in front of the extraction nozzle, position (A), to

check whether any radioactive species were produced in the neutron-induced fission. Ions extracted from the gas cell were directly implanted in the foil, which was put at a −300 V potential. After several hours implantation the foil was moved to a low background station where the possible γ-ray activity was searched with a planar Canberra BEGe 3025 high purity germanium detector. Gamma lines corresponding to the decay of long-lived fission products ^{95,97}Nb, ^{95,97}Zr and ^{141,143}Ce were observed. This confirmed that a beam of fission products was extracted from the ion guide.

The analysis of the mass spectra of the stable ion beams collected with the MCP detector in the switchyard (MCPSw) showed mass peaks corresponding to water molecules. The source of a water leak was never revealed for certain. A quick test with the proton-induced fission ion guide on the next day nevertheless showed that the yields from the knowingly reliable proton-induced fission ion guide were down by about a factor of ten.

For the second experiment in June the ion guide was equipped with a titanium foil (6), see figure 4.7, and an additional Si detector before the dipole magnet (5) was installed in position (B), figure 2.12. It was expected that the total beta activity of the unseparated beam of fission products would be sufficient to be measured with this silicon detector. The purpose of the titanium foil was to collect fission fragments, which escape the U target and pass through the buffer gas. The γ-ray activity of the titanium foils could then be measured off-line. The amount of fission products on the titanium foil was considered to be a measure of the amount of reaction products stopped on the walls of the neutron-induced fission ion guide.

In the on-line run in June the intensity of the beam extracted from the ion guide and measured with FC1 was not significantly higher than in the first experiment in April. This time, no sign of water molecules were observed in the mass spectrum. The silicon detector placed before the dipole magnet was used to monitor the extracted activity. Both total current and extracted beta activity were measured as a function of the primary proton beam current, which is expected to be directly proportional to the intensity of the neutron beam emitted from the beryllium neutron source. The correspondence between these is shown in figure 4.8. The total current extracted from the ion guide consists of the stable and radioactive ions. The count rate of the Si detector represents only radioactive decay of fission products.

It can be seen from figure 4.8, that the extracted current increases almost linearly with increasing primary beam current. The count rate of the Si detector at the lower intensity increases linearly but the last point around 11 μA much has a much higher count rate than expected on the basis of the low proton beam intensity. The count rate at this point was checked several times and the effect was reproduced, at least within that on-line test. During the experiment, 11 μA was the highest intensity available from the K130 cyclotron. No convincing reason for the sudden enhancement of the extracted activity as compared to the total current has been proposed. Increasing the proton beam intensity can in principle change the position,

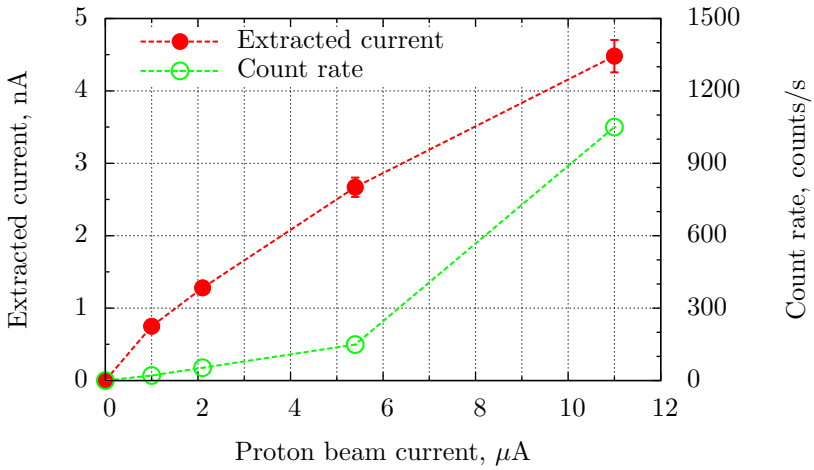

Figure 4.8: The dependence of total current extracted from the ion guide (red line) and a count rate of the Si detector (green line) on the proton beam intensity. All points were measured at 400 mbar of the buffer gas pressure. Error bars of the count rate includes only statistical uncertainty and they are smaller than the size of points.

shape and the intensity distribution of the proton beam spot on the neutron source target in such a way that the produced neutron beam covers more of the fissile target. However, if this is the case, the total extracted current should also be increased, since the gas is ionised by the fission products.

Another important characteristic of the ion guide is a gas pressure dependence of the extracted current and the count rate of the Si detector. Such curves are presented in figure 4.9. In this comparison, the behaviour of both curves is very similar. The dependence of the extracted ion current and the silicon detector count rate is almost linear up to 350 mbar. The point measured at 400 mbar deviates slightly but not significantly from this trend. More importantly, this deviation is similar for both current and count rate. It is also worth noticing that as compared with the ion guide designed for the proton-induced fission, the ion guide prototype for neutron-induced fission studies does not have a thin entrance windows for the proton beam. Therefore it does not have any limitations on the gas pressure due to the beam windows. The gas volume in the ion guide for n-induced fission is separated from the vacuum by aluminum walls of 2 mm thick at least.

The volume of the target chamber (1) in figure 2.14 serves as the first differential pumping stage of the mass separator. Evacuated from the fission ion guide (5) helium fills this volume. The beam line (2) isolates the low pressure helium in the

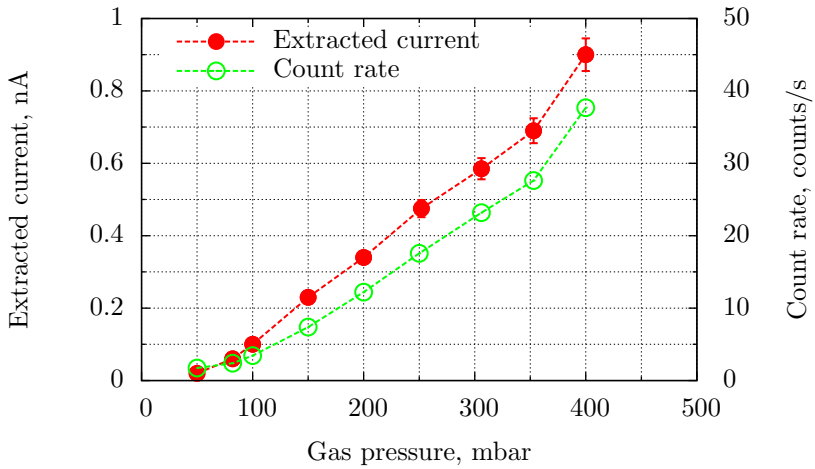

Figure 4.9: The total current extracted from the ion guide (red line) and a count rate of the Si detector (green line) depending on the He buffer gas pressure. All points were measured at 1 μA proton beam intensity. Error bars of the count rate includes only statistical uncertainty and they are smaller than the size of points.

target chamber (1) preventing its ionization by the primary beam, but it is not completely sealed. In typical conditions, the isolation is sufficient to maintain the primary beam line vacuum. The maxium pressure in the neutron-induced fission ion guide was almost two times higher than in any typically used ion guides. The target chamber pressure was also higher than usually. As a result, the pressure in the cyclotron beam line increased until critical value and limited the maximum gas pressure in the ion guide.

Despite the fact that the current of the mass separated ion beam was too low to measure with the faraday cup (FCSw), the MCPSw detector was used to select the mass number $A = 99$ and radioactivity was checked with the silicon detector (SiSw) at the switchyard (6). The spectrum in figure 4.10, solid line, clearly shows β-activity above the background, dashed line. The intensity of any mass separated beams after the dipole magnet was so low that it was impossible to transport the beam towards the spectroscopy station (12) and perform on-line measurements.

Another part of the test experiment is related to off-line measurements. To obtain the quantitative information about the ion guide it was decided to implant ions into a foil, placed in position (B), and use the low background station equipped with the germanium detector to search for long-lived γ-ray activity. A gamma ray spectrum of the implanted radioactive species is presented in figure 4.11(c). The strong ^{99}Mo

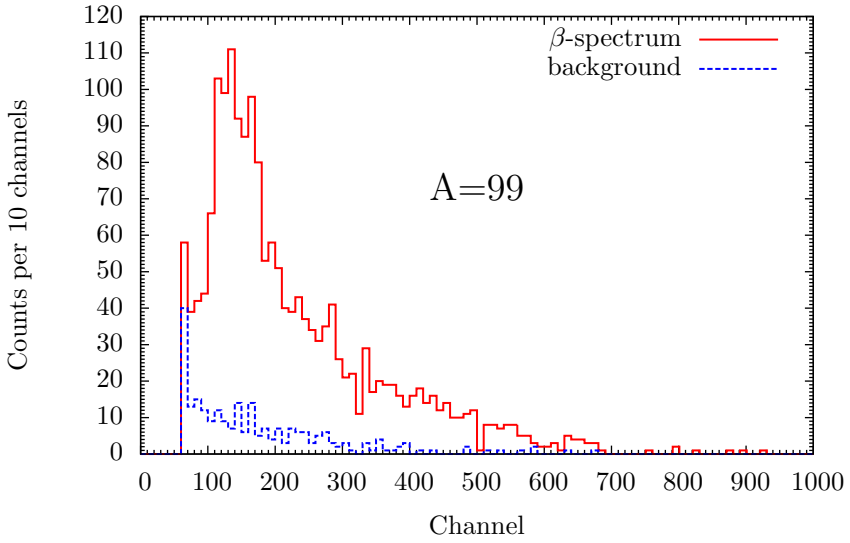

Figure 4.10: The β-spectrum of the separated $A = 99$ isobaric chain, collected during 500 seconds with the silicon detector (SiSw) at the switchyard (6). A proton beam intensity was 5 μA and the gas pressure 400 mbar. Solid line refers to the β-activity. Dashed line is a background, measured also 500 seconds with the radioactive beam blocked.

peak confirms that the β-spectrum in figure 4.10 is related to the β-activity of the isobaric chain $A = 99$. Similar spectra were collected for the uranium target (5), see figure 4.11(a), and the titanium foil (6), see figure 4.11(c).

The amount of fission products left in the targets and implanted in the collection foil could be estimated from the γ-ray intensities of the long-lived fission products. Their precursors decay with time after the neutron irradiation and the γ-rate of the long-lived species corresponds to their cumulative yield. The precise fission yield distributions for the wide neutron energy range is not known. The cumulative yields of long-lived nuclides in fast fission of ^{238}U from [37] were considered as a close approximation.

Obtained results are very preliminary and experimental data require detailed analysis, which is out of the scope of the present work. However, a brief checking of γ-spectra allows to estimate important parameters of the ion guide such as a fraction of fission products stopped in the ^{nat}U target, in walls and a fraction of extracted fission products.

The key point of these estimations is a number of neutron-induced fissions and

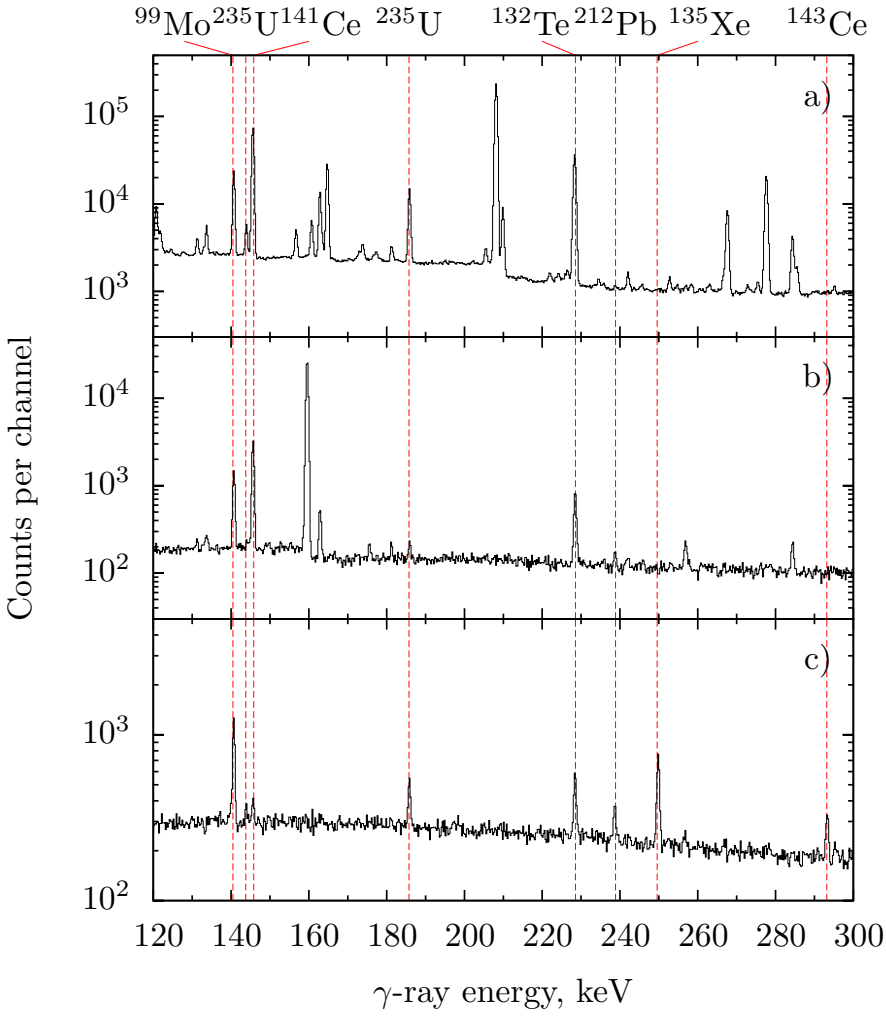

Figure 4.11: Gamma-ray spectra obtained from different samples. a) is the spectrum measured from the ^{nat}U target irradiated by neutrons. b) is the spectrum from the Ti foil, installed inside the ion guide. c) is the γ-ray spectrum from the aluminium foil in front of the silicon detector, position (B), collected during 18 hours immediately after 30 minutes of implantation. Spectra (a) and (b) were collected about 18 days after the neutron irradiation.

yields of nuclides, which are used for estimations. The calculation of the total amount of fissions is based on the measured neutron energy spectra from figure 4.6 together and on the neutron-induced fission cross-section of ^{238}U from the EXFOR database [45] and it results to about 10^{12} fissions in each target. If to assume that after 18 days of waiting time all precursors decay to their doughter nuclei, the amount of the ^{141}Ce, ^{103}Ru, ^{95}Zr and ^{95}Nb isotopes in the target should be about $5 \cdot 10^{10}$ atoms according to the cumulative yields of ^{238}U fission induced by fast neutrons [37]. The amount of those isotopes deduced from the γ-spectrum (figure 4.11(a)) is about $4 \cdot 10^{8}$. As a result, the fraction of the whole isobaric chain with mass numbers A=141, 103 and 95 stopped in the target is the order of 1 %.

The same estimations were done for the aluminium foil installed in position (B), see figure 2.12. Due to waiting time of about 18 hours before the γ-measurement the isotopes ^{135}Xe, ^{143}Ce, ^{133}I and ^{97}Zr with shorter half-lives were chosen to calculate extraction efficiency. In all these cases the fraction of isotopes observed on the aluminium foil after the extraction from the ion guide is about $\sim$0.01 %. Such rough numbers only illustrates the general picture and require more careful and systematic data analysis or even new measurements.

In comparison a typical total efficiency for proton induced fission ion guide is about 10 time larger. This is determined from the cumulative yield of mass separated ^{112}Rh, which is $\sim$12 mbarn in proton-induced fission of ^{nat}U. This production cross section can be taken from calculations [40] or estimated from the independent yields deduced from experimental isotopic yield distributions [118] and mass yields from [125].

5 Summary and outlook

5.1 Main results

The independent fission product yields in proton-induced fission of ^{232}Th at 25 MeV were measured employing a novel experimental method. These yields are important for the development of nuclear fission models as well as for conducting experiments at facilities such as IGISOL–4. Knowledge of the yields from different reactions helps to choose an appropriate combination of projectile particles and targets for particular experiments.

A comparison between experimentally determined independent yields in proton-induced fission of ^{238}U [118] and ^{232}Th [present work] at 25 MeV is given in figure 5.1. It shows that the uranium target is preferable for production of neutron-rich nuclides in the doubly magic tin region. A theoretical model [40] predicts an enhancement in the production of even more neutron-rich nuclei in neutron-induced fission.

To prove this hypothesis a neutron source (proton-neutron converter target) was designed, developed and characterised. Obtained neutron spectra were found to be in accordance with design simulations done with MCNPX. The conversion factor of protons to neutrons emitted in 1 steradian in the forward direction was observed as 200:1. The present setup produces an almost white spectrum and relatively high neutron energies. Some space is left for possible improvements and developments, for example, production of a quasi-monoenergetic neutron beam from a thin beryllium target.

A prototype of the neutron-induced fission ion guide was developed and tested in on-line experiments. The test was successful in the respect that fission of natural uranium target was induced with energetic neutrons. Fission products were stopped in the gas cell, extracted, accelerated and even mass separated by a dipole magnet. All of this proves the principle of the concept.

Yet a remaining issue is that the achieved beam intensity and ion guide efficiency were low. The maximum primary beam intensity during these tests was only one tenth of the intensity, which the neutron converter is designed to achieve. Also, the ion guide prototype contained only two uranium targets instead of six. The geometry of the gas cell was not optimised, it was modified as little as possible to be able to compare proton-and neutron-induced fission with only fewest possible assumptions. This kind of comparison, probably, does not favor the production of intense beams from neutron-induced fission.

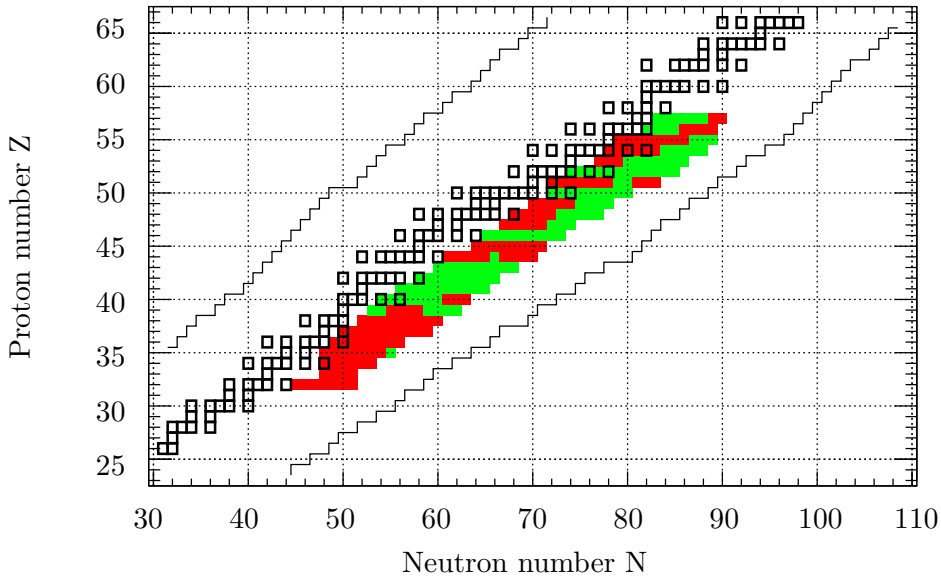

Figure 5.1: Difference between independent product yields of fission ^{238}U and ^{232}Th induced by 25 MeV protons. Red area shows where yields are higher for ^{232}Th, green area shows where yields are higher for ^{238}U.

There are many parameters, which can significantly improve the performances of the neutron-induced fission system. First and the most straightforward way is increasing the primary beam intensity and number of fissioning targets. From the tests it is also clear that the neutron-induced fission ion guide benefits from increasing of the helium gas pressure which was limited by the pumping capacity of the primary beam line. Other possibilities to improve the intensity of the radioactive beams produced in neutron-induced fission require proper technical developments.

5.2 Future perspectives

From the perspective of the independent fission yield measurements the method employed in this work can be applied to obtain an energy dependence of the independent fission yields of various fissile materials. The independent fission yields can be determined in reactions with another projectiles as well.

Nuclear fission at relatively low excitation energies is a process of many degrees of freedom strongly influenced by nuclear structure. Measurements of the independent

fission product yields allows to determine the role of the nuclear structure in the formation of fission products.

The development of a multireflection time-of-flight spectrometer (MR-TOF) at the IGISOL facility will give new possibilities for independent fission yield measurements. This instrumentation when compared to the Penning trap has several advantages such as shorter separation time and higher ion capacity, while the mass resolving power remains at the level of the Penning trap.

Concerning the neutron-induced fission significant improvement can be done in the design of the ion guide. Electrostatic and radiofrequency fields can effectively guide ions towards the extraction nozzle. The cryogenic gas catcher at FRS [59] and CARIBU [58] are real examples how such technical development can lead to an increased the ion stopping and extraction efficiency.

Appendix

Figures showing the independent fission yields of the proton-induced fission of ^{232}Th at 25 MeV. Experimental yields measured in this work (see details in sections 3.3–3.5) are compared with the theoretical predictions of the model [40].

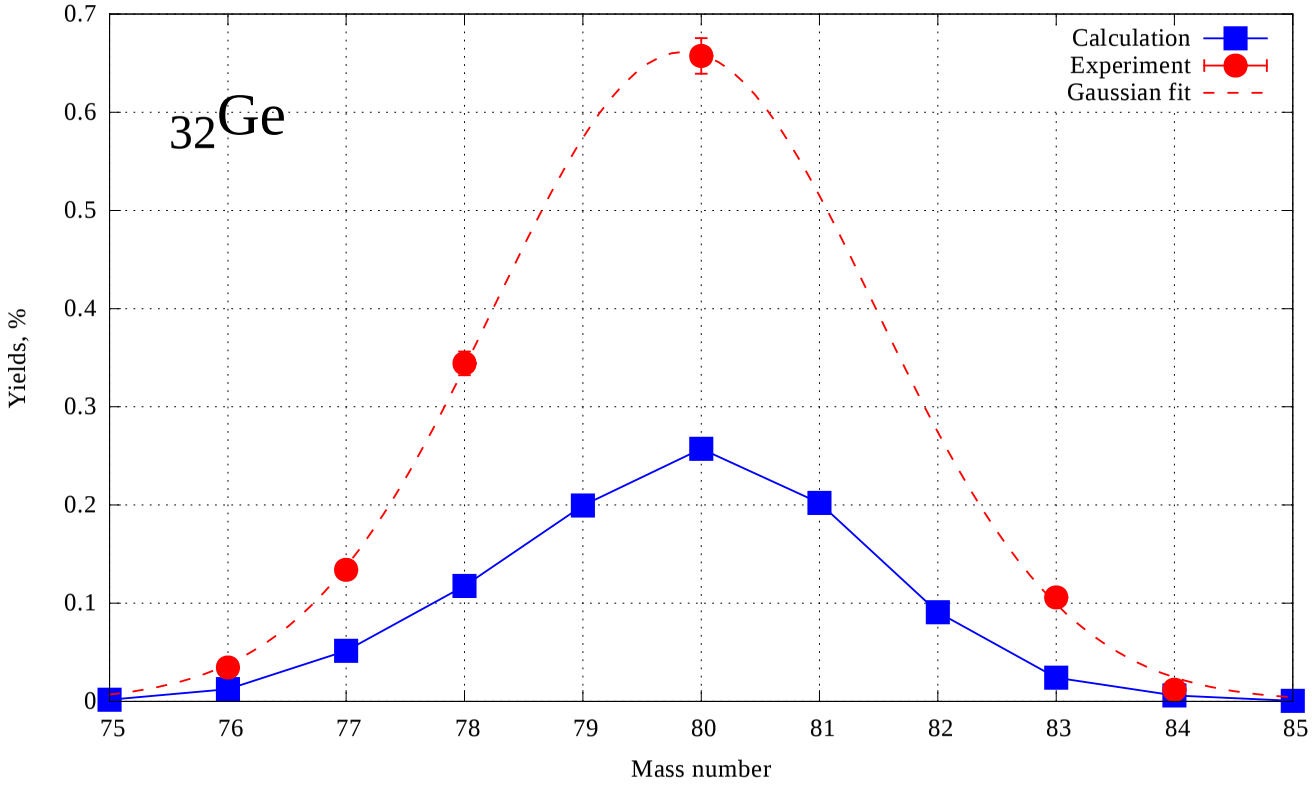

Figure 5.2: Independent yields of $_{32}$Ge.

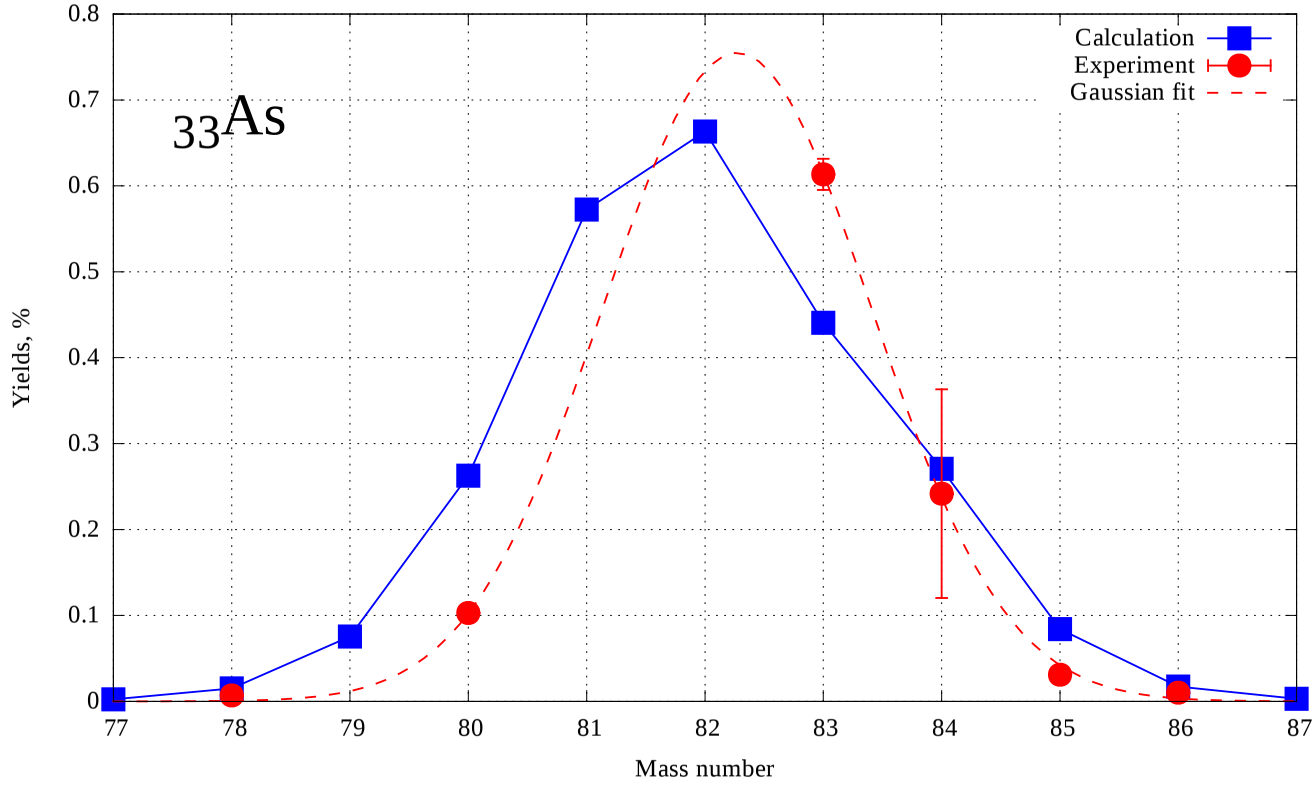

Figure 5.3: Independent yields of $_{33}$As.

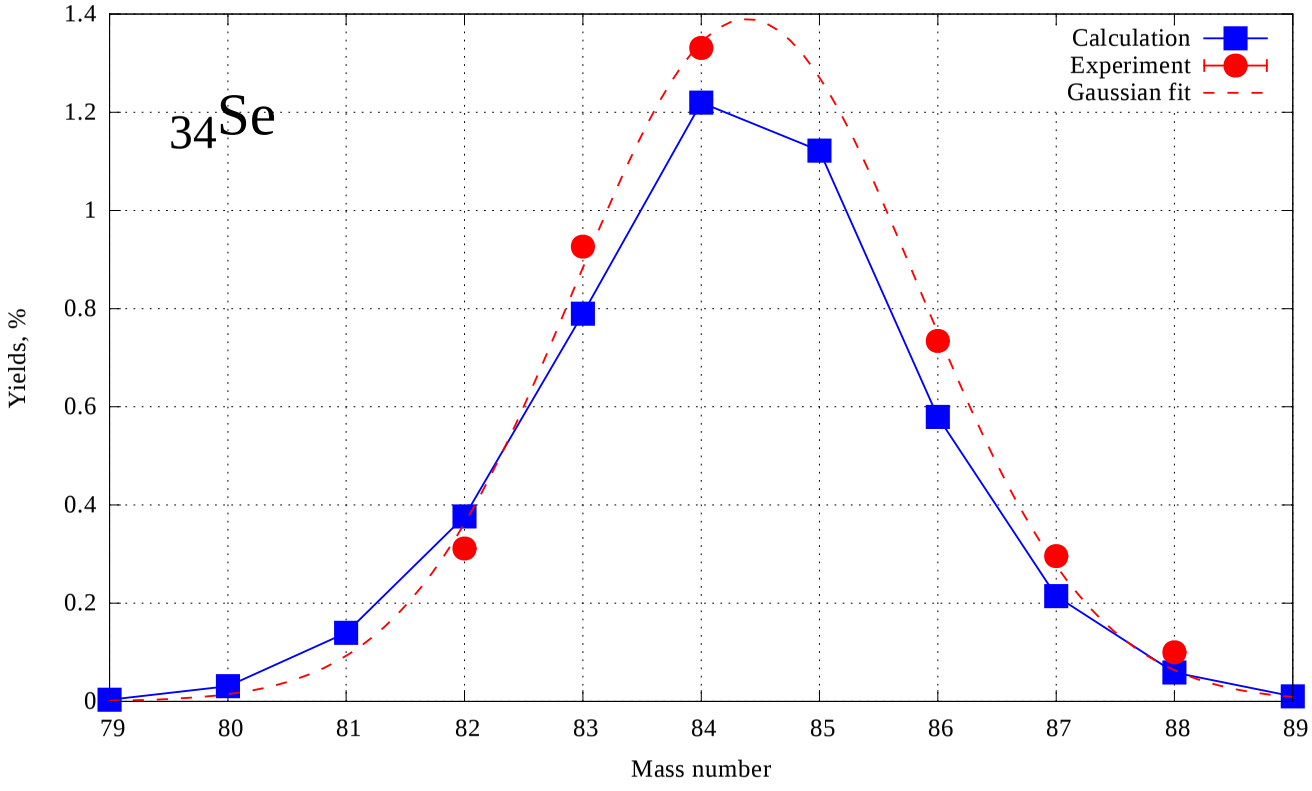

Figure 5.4: Independent yields of $_{34}$Se.

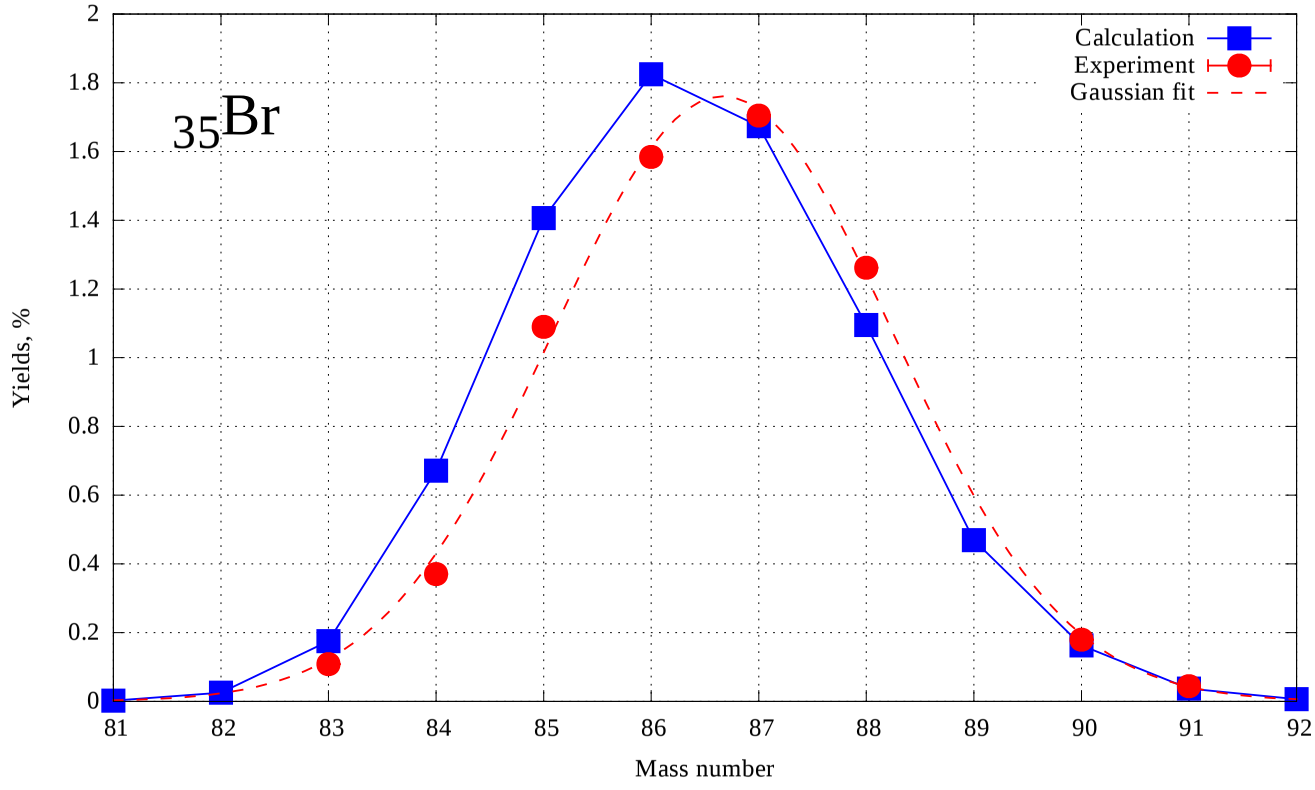

Figure 5.5: Independent yields of $_{35}$Br.

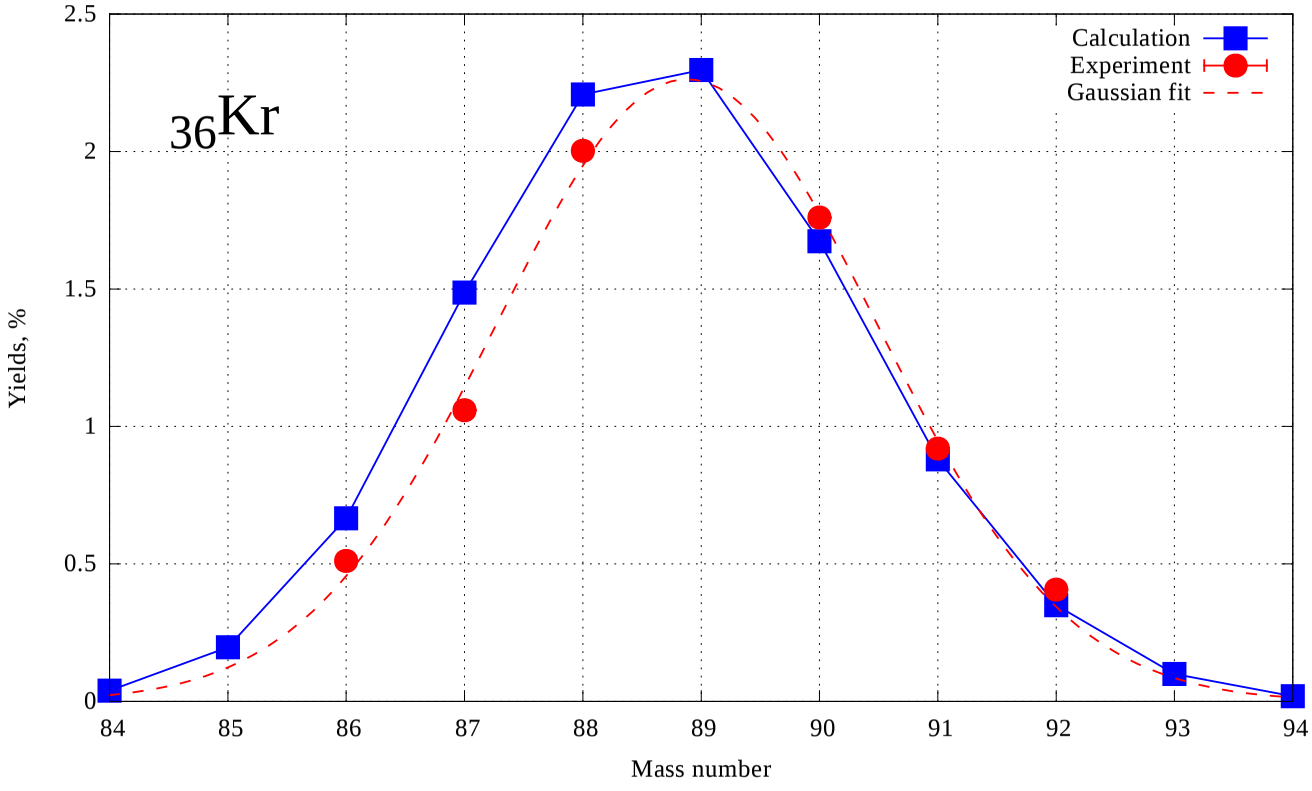

Figure 5.6: Independent yields of $_{36}$Kr.

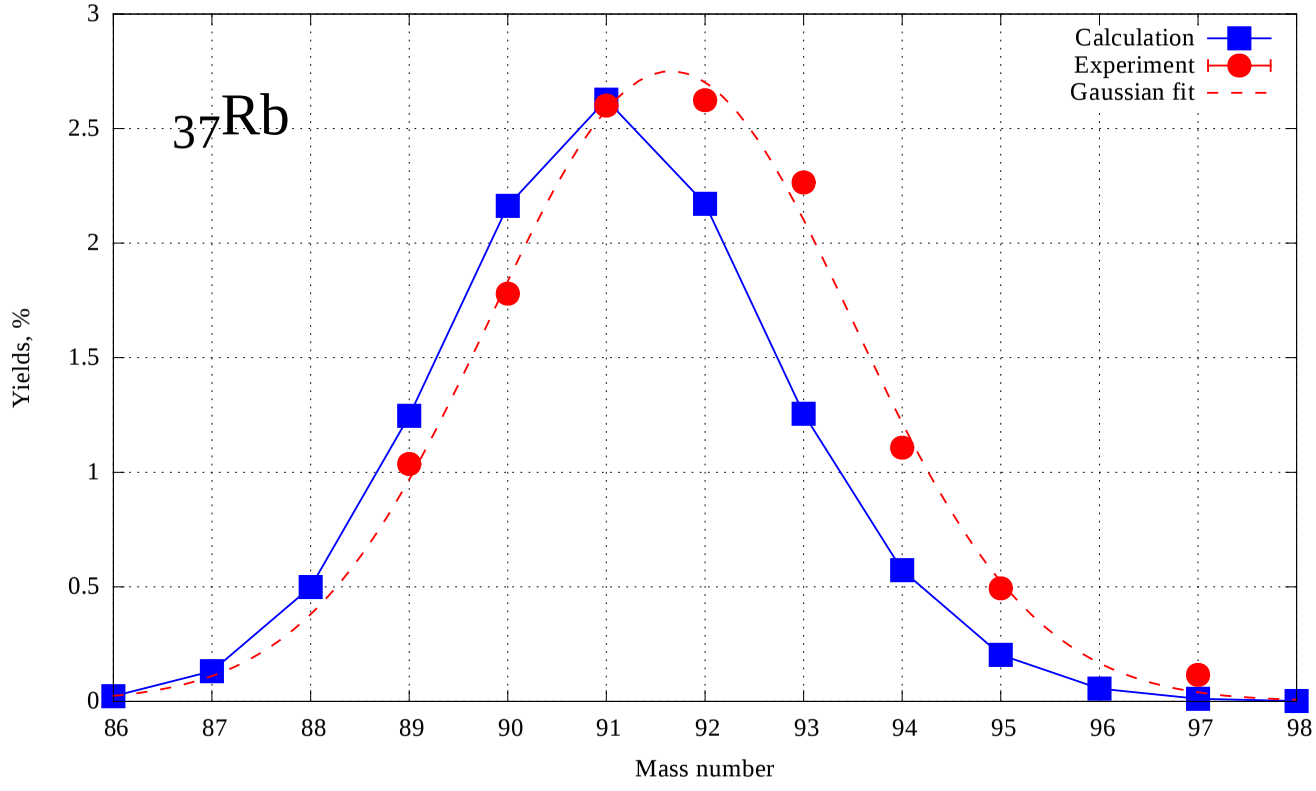

Figure 5.7: Independent yields of $_{37}$Rb.

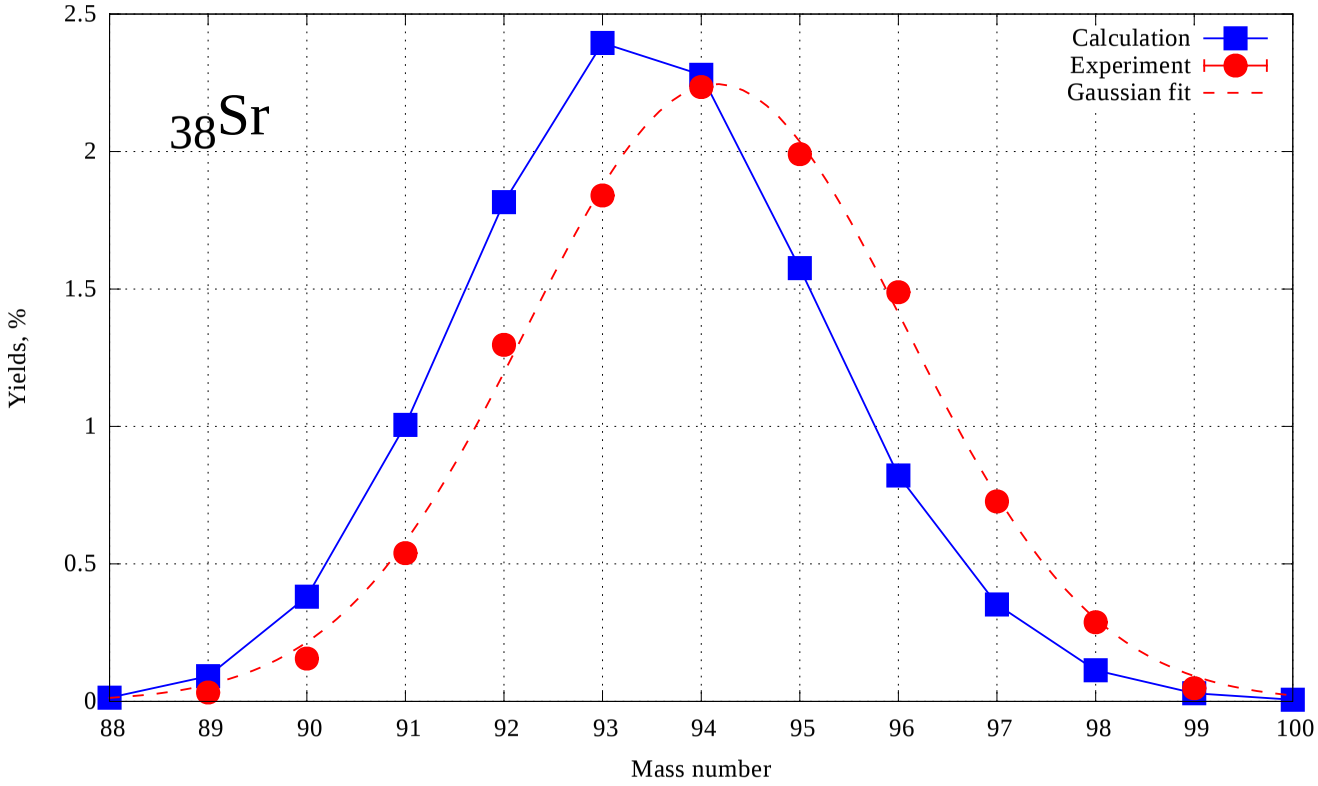

Figure 5.8: Independent yields of $_{38}$Sr.

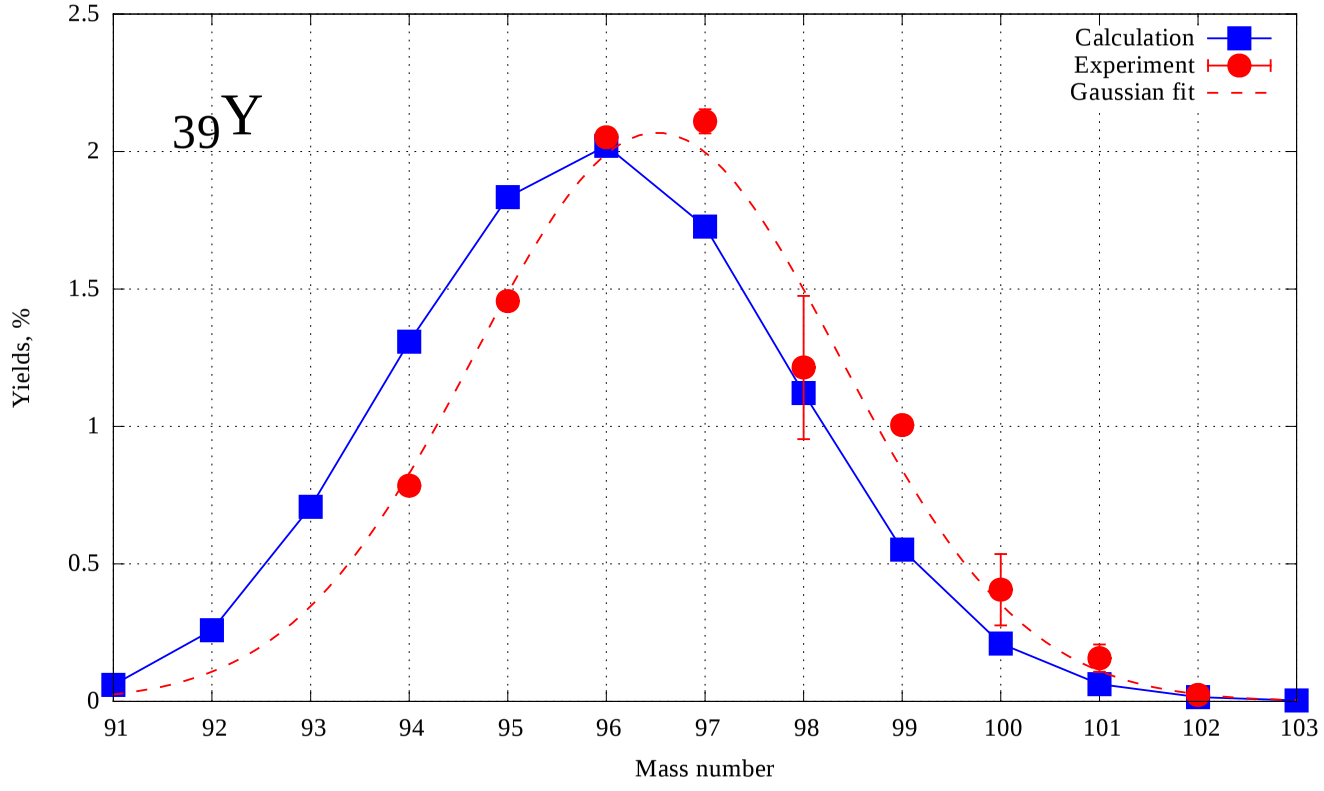

Figure 5.9: Independent yields of $_{39}$Y.

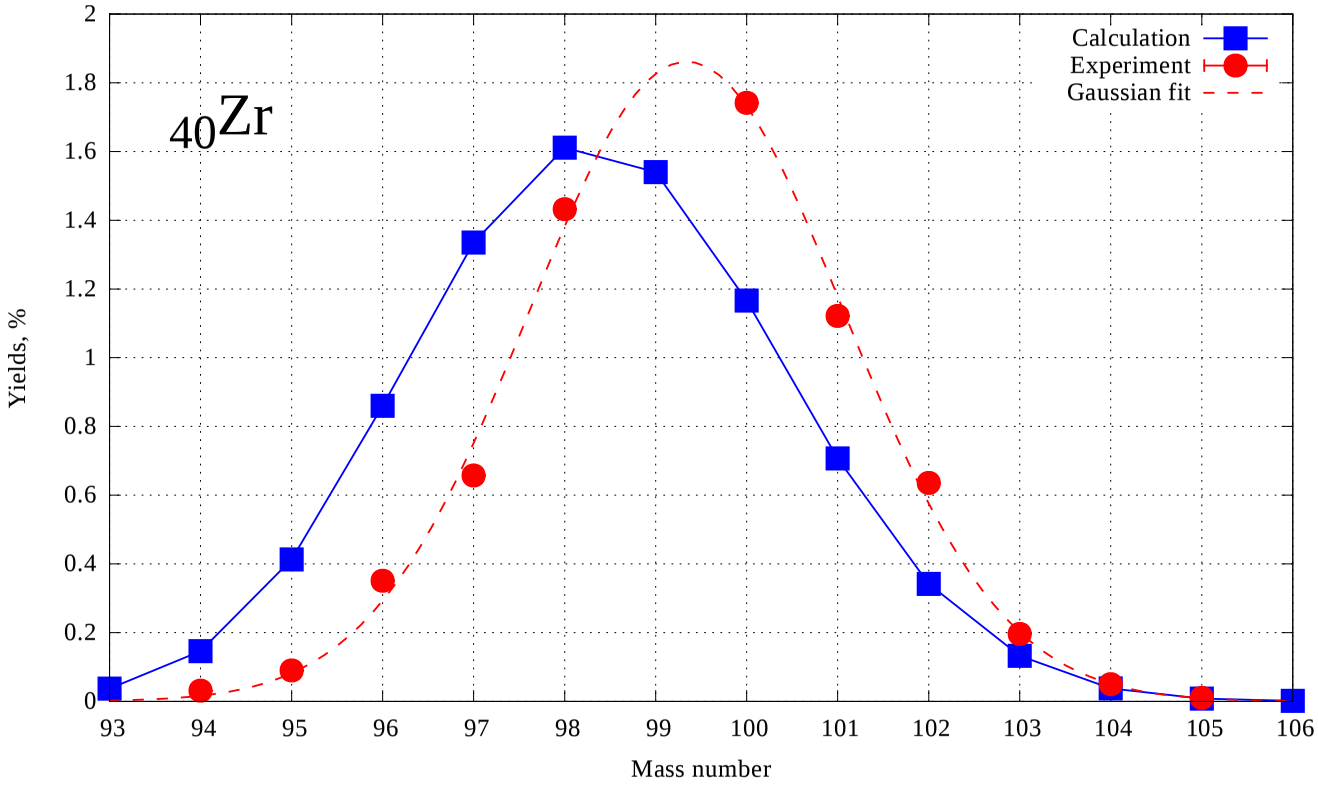

Figure 5.10: Independent yields of $_{40}$Zr.

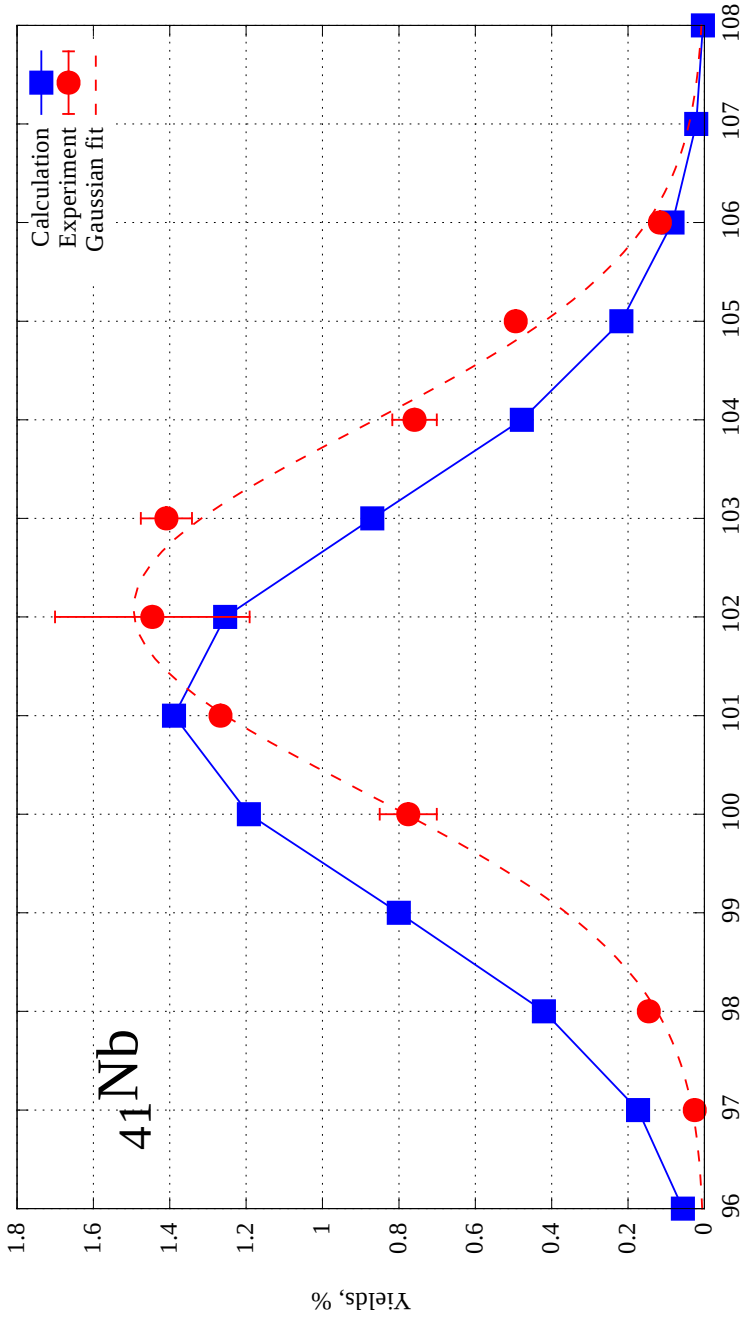

Figure 5.11: Independent yields of $_{41}$Nb.

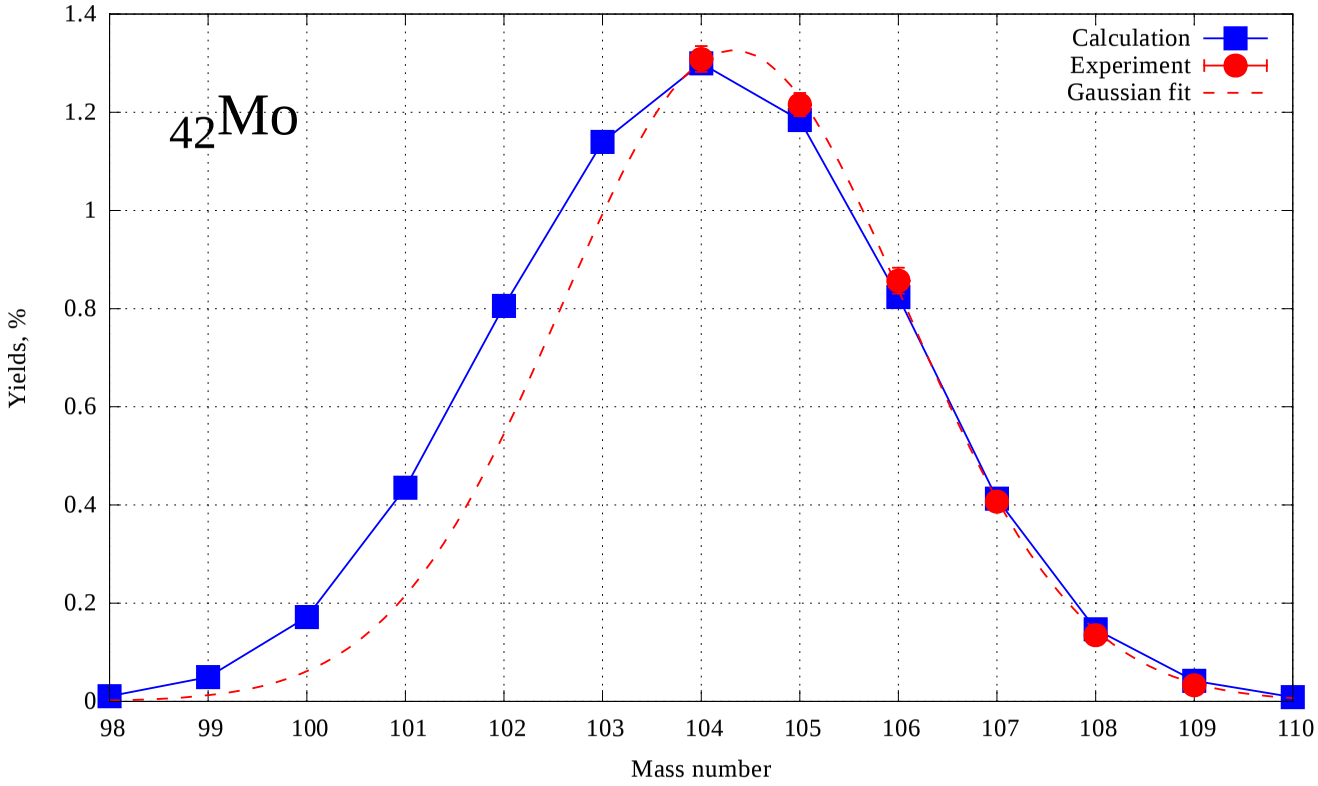

Figure 5.12: Independent yields of $_{42}$Mo.

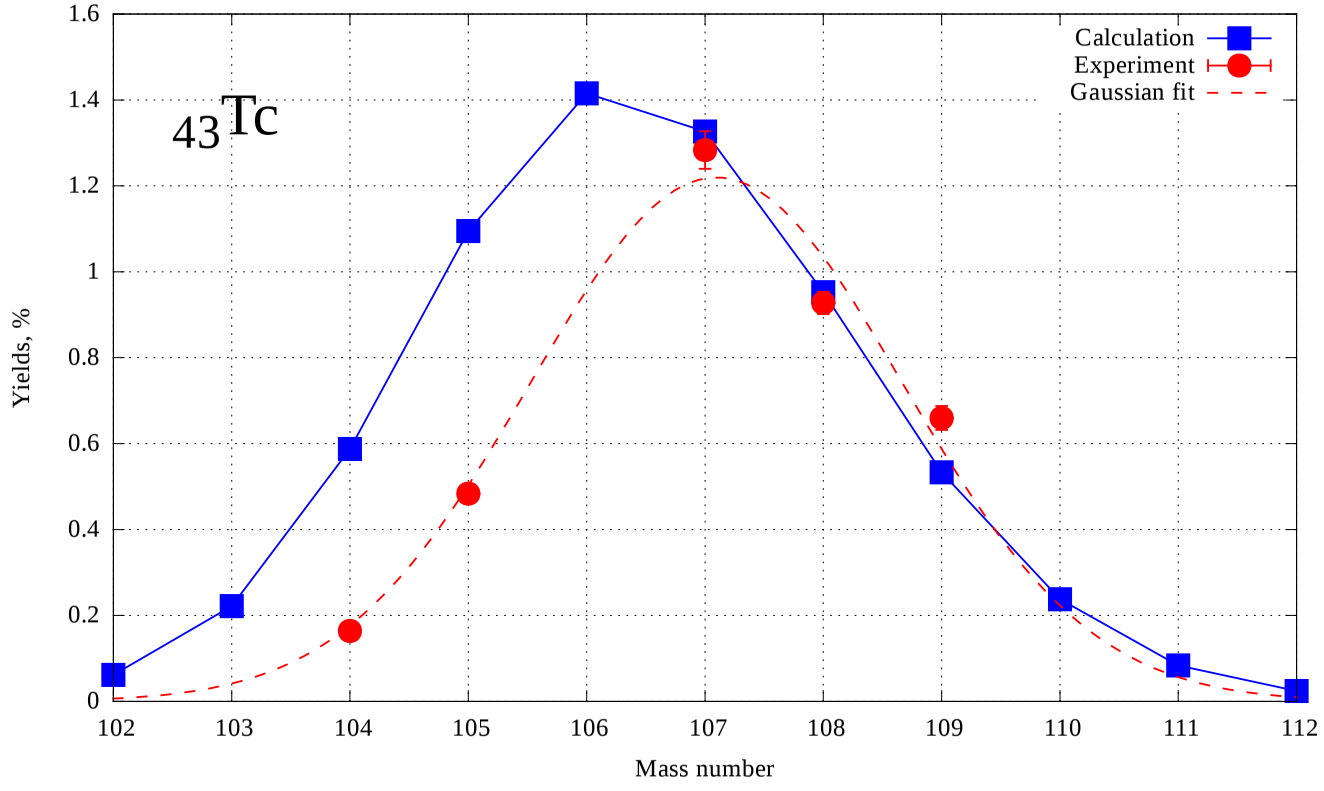

Figure 5.13: Independent yields of $_{43}$Tc.

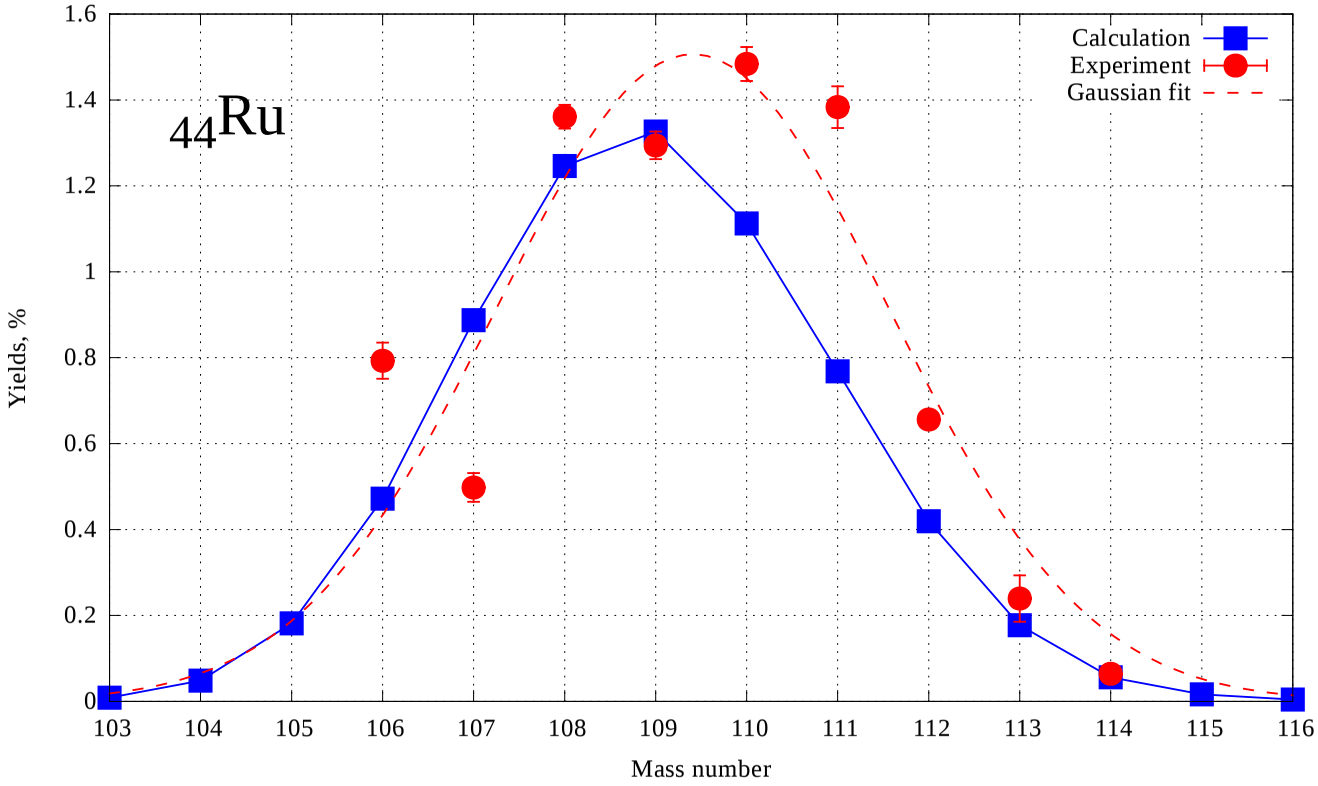

Figure 5.14: Independent yields of $_{44}$Ru.

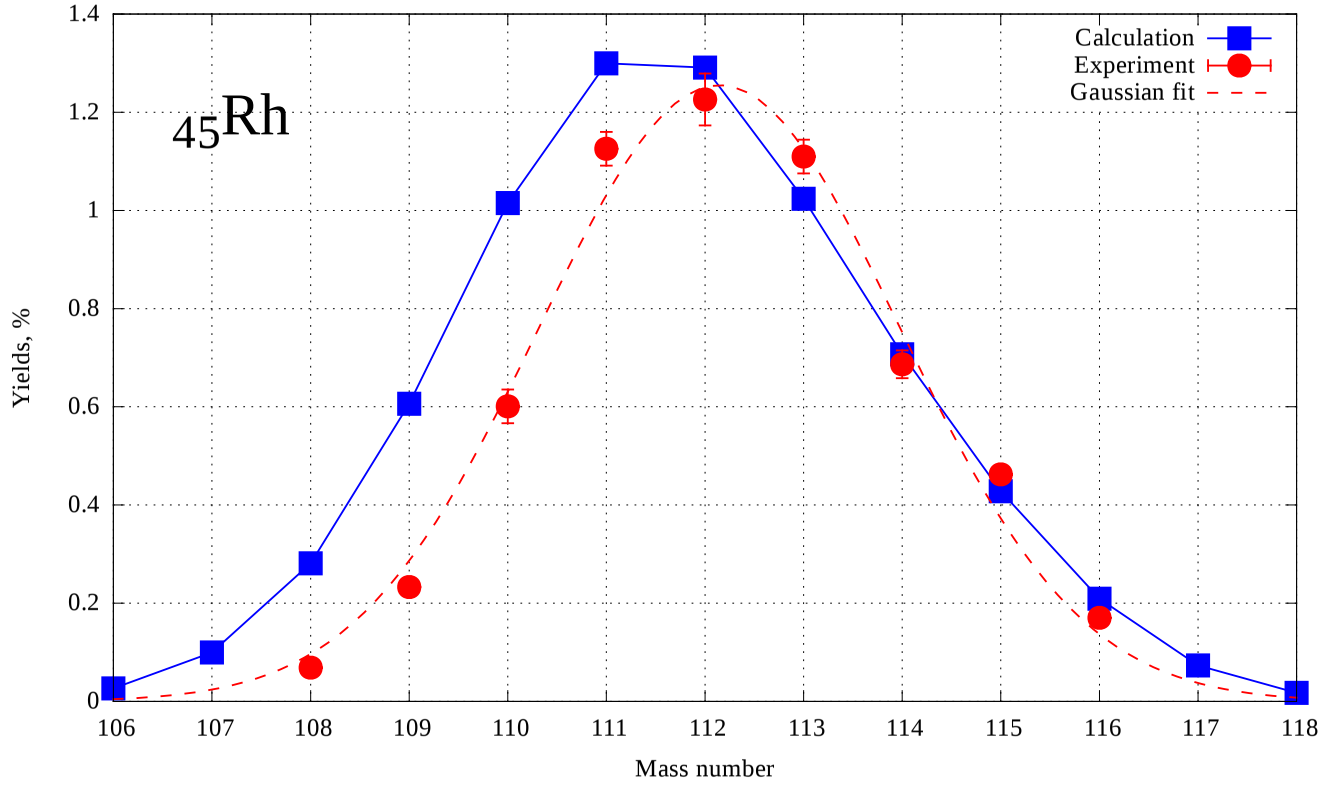

Figure 5.15: Independent yields of $_{45}$Rh.

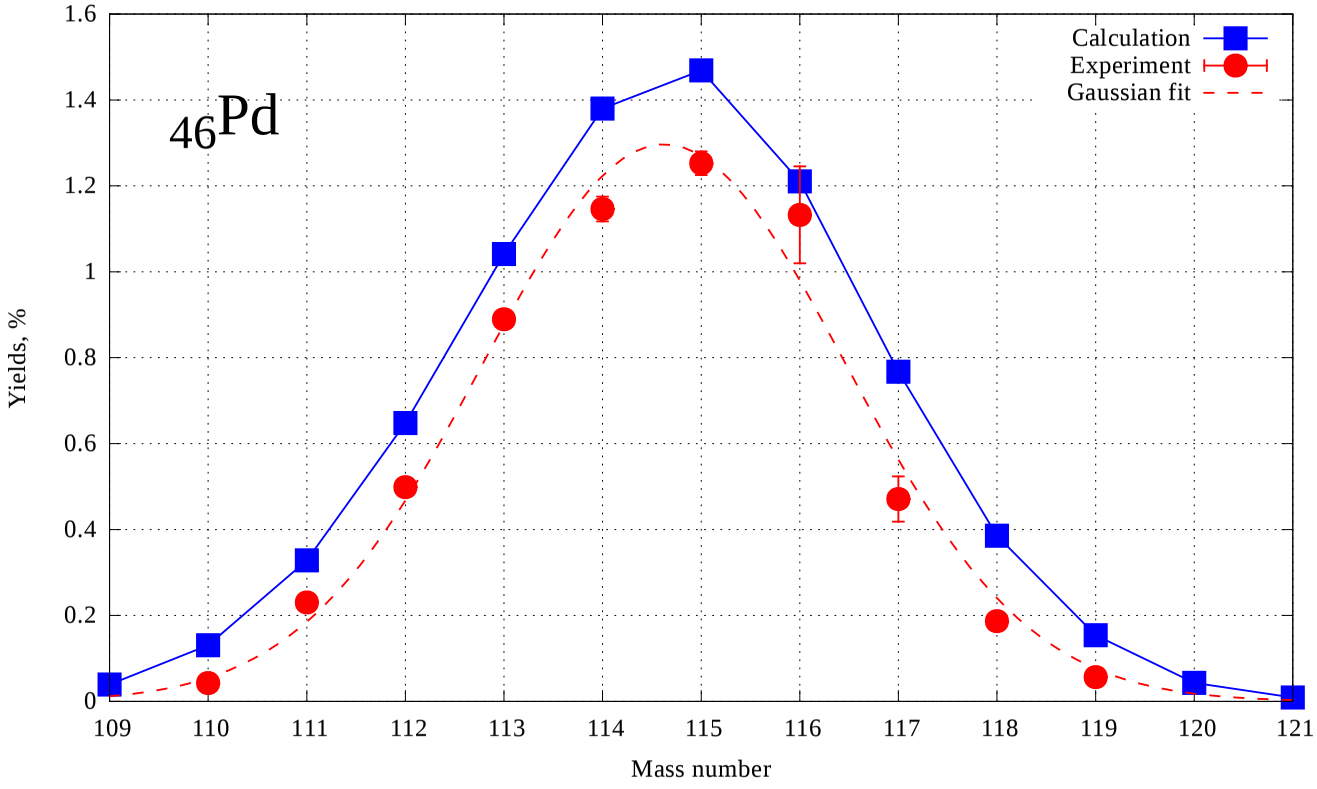

Figure 5.16: Independent yields of $_{46}$Pd.

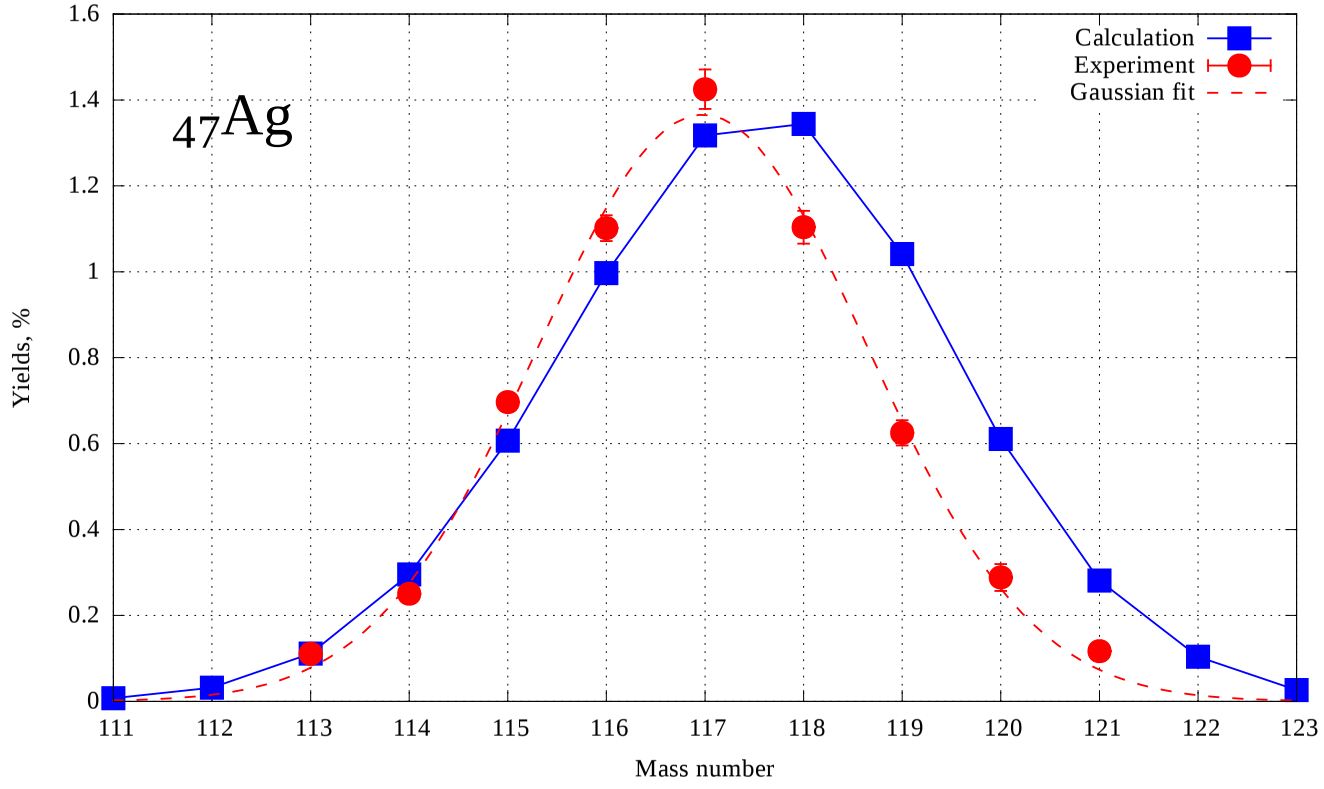

Figure 5.17: Independent yields of $_{47}$Ag.

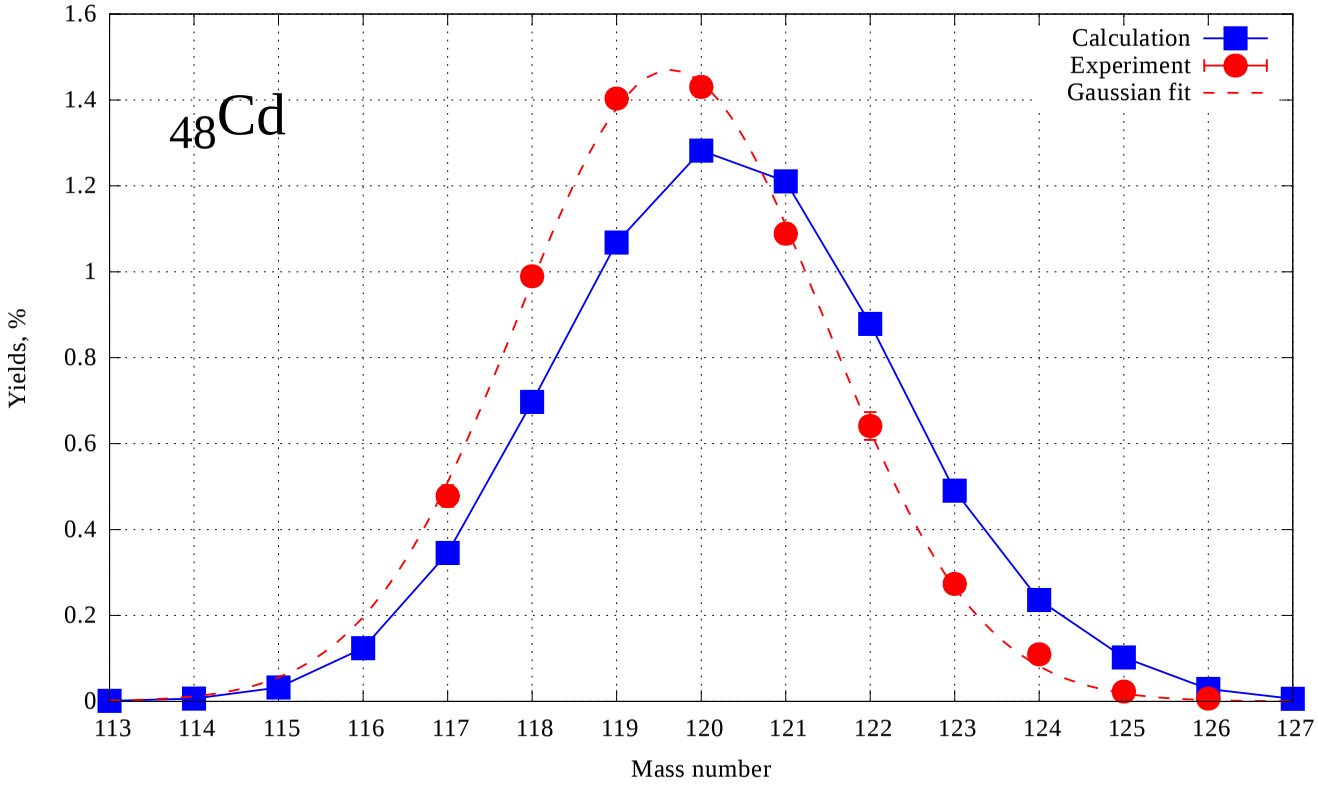

Figure 5.18: Independent yields of $_{48}$Cd.

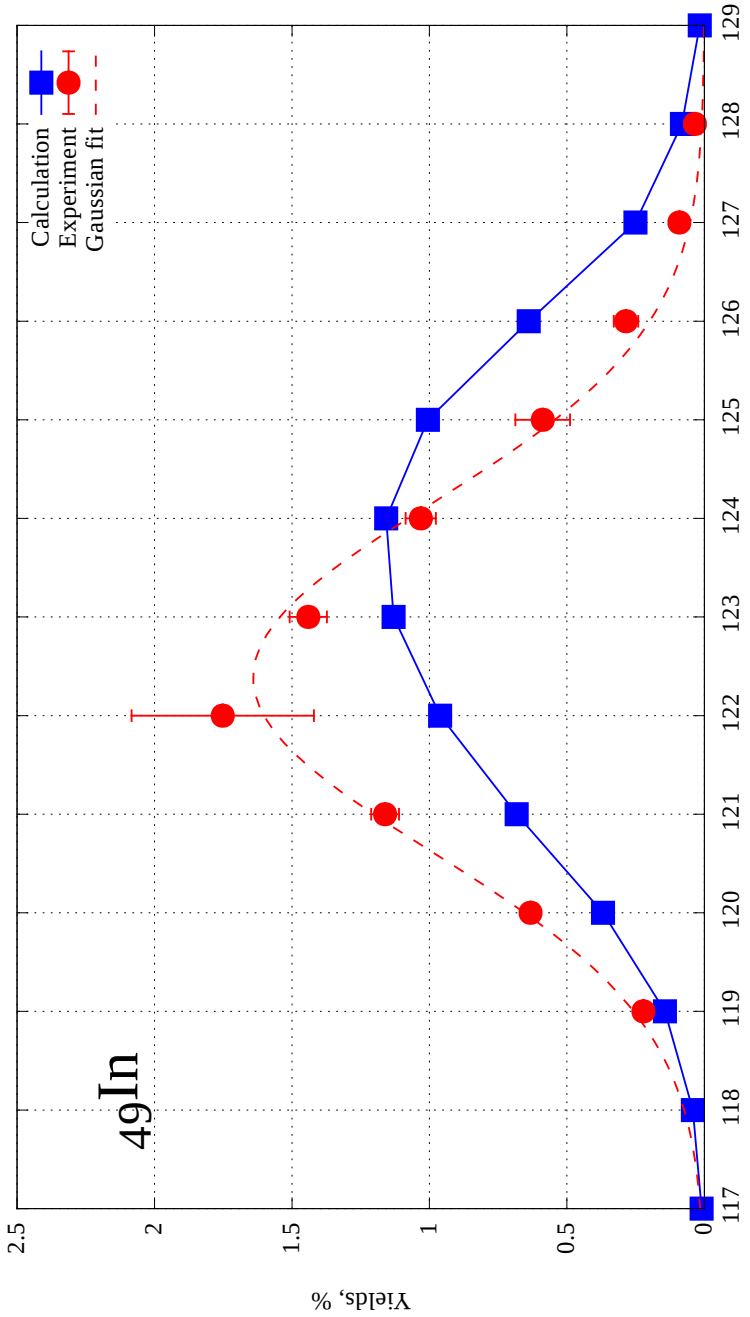

Figure 5.19: Independent yields of $_{49}$In.

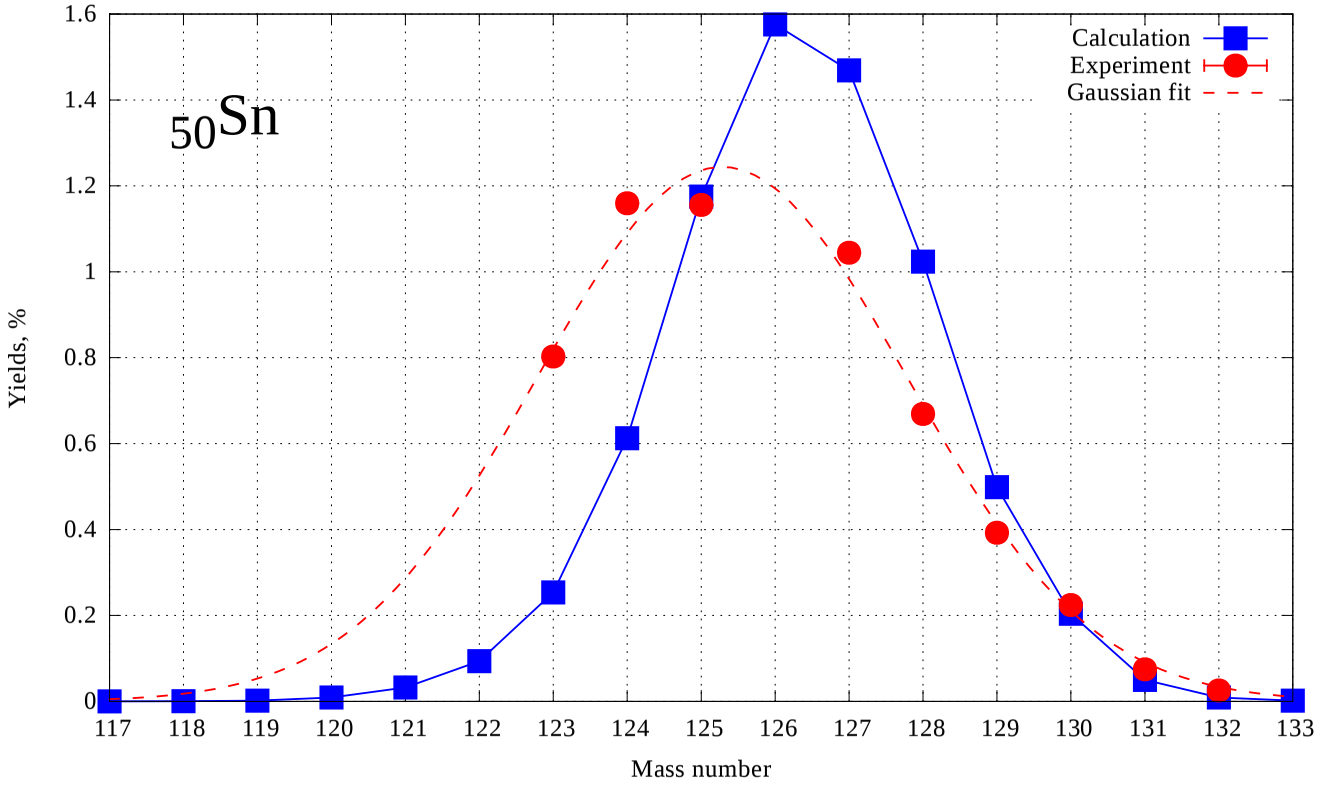

Figure 5.20: Independent yields of $_{50}$Sn.

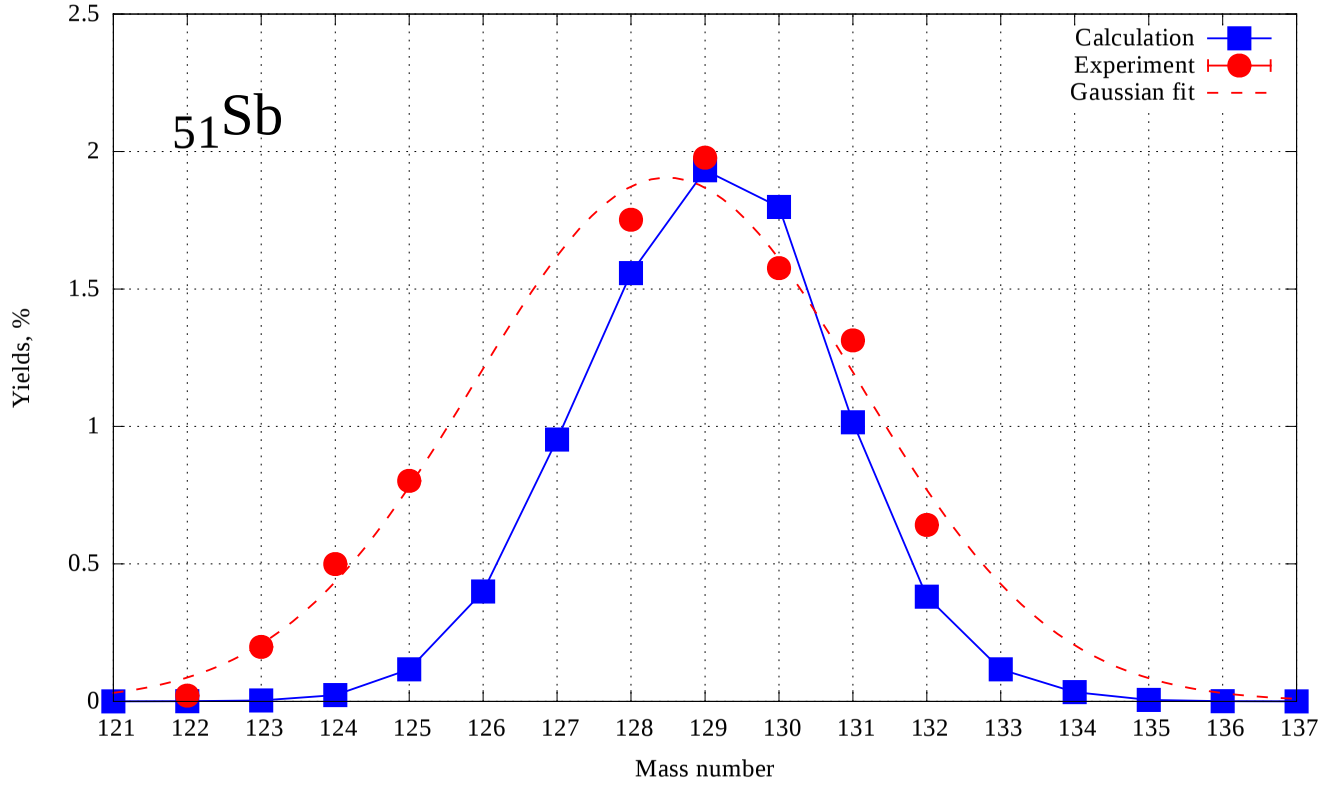

Figure 5.21: Independent yields of $_{51}$Sb.

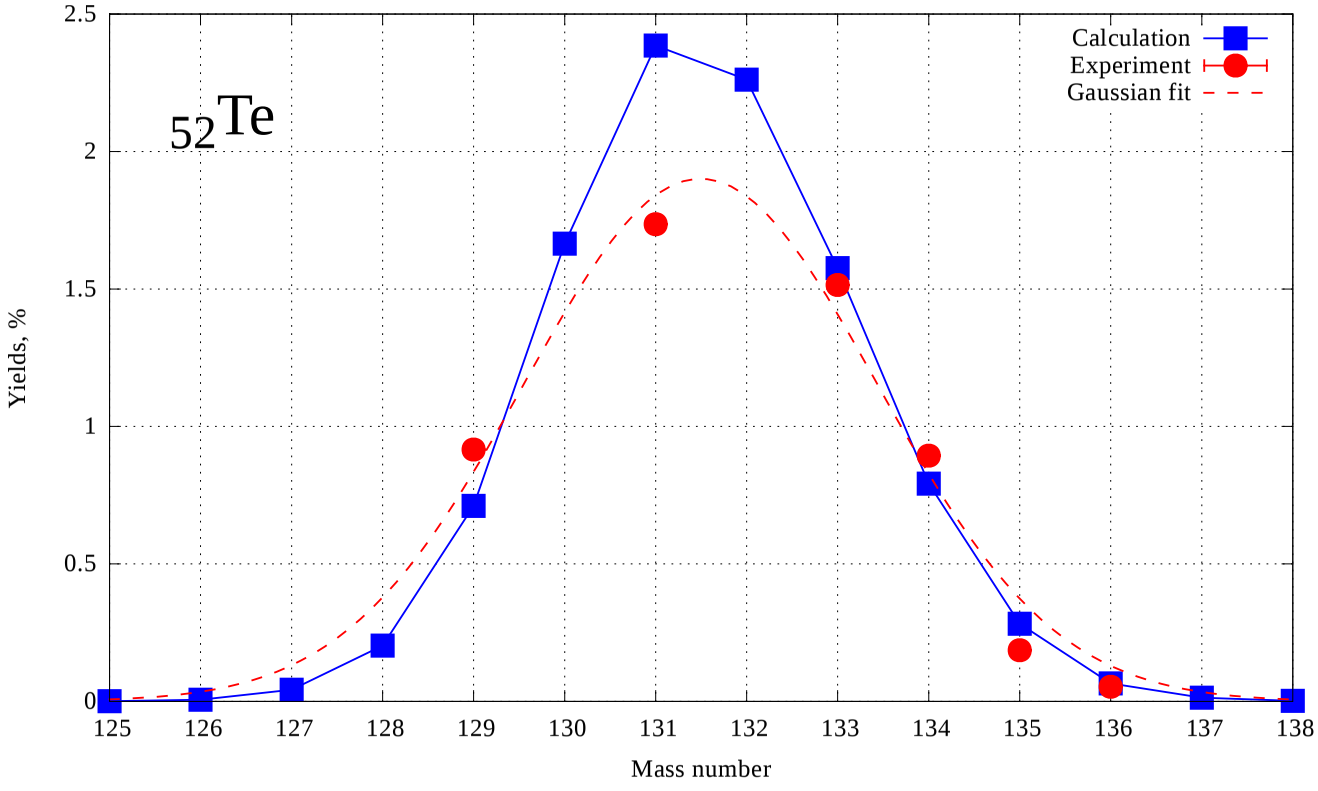

Figure 5.22: Independent yields of $_{52}$Te.

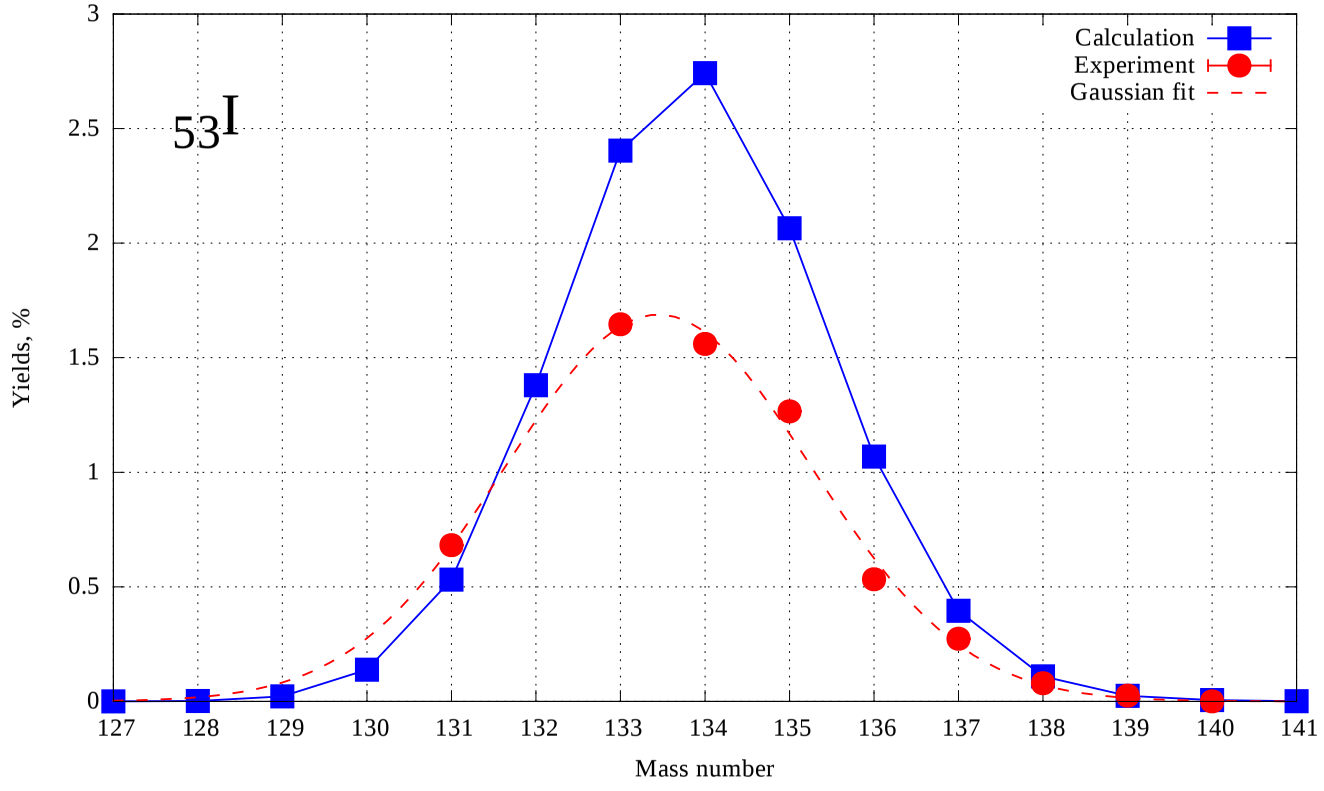

Figure 5.23: Independent yields of $_{53}$I.

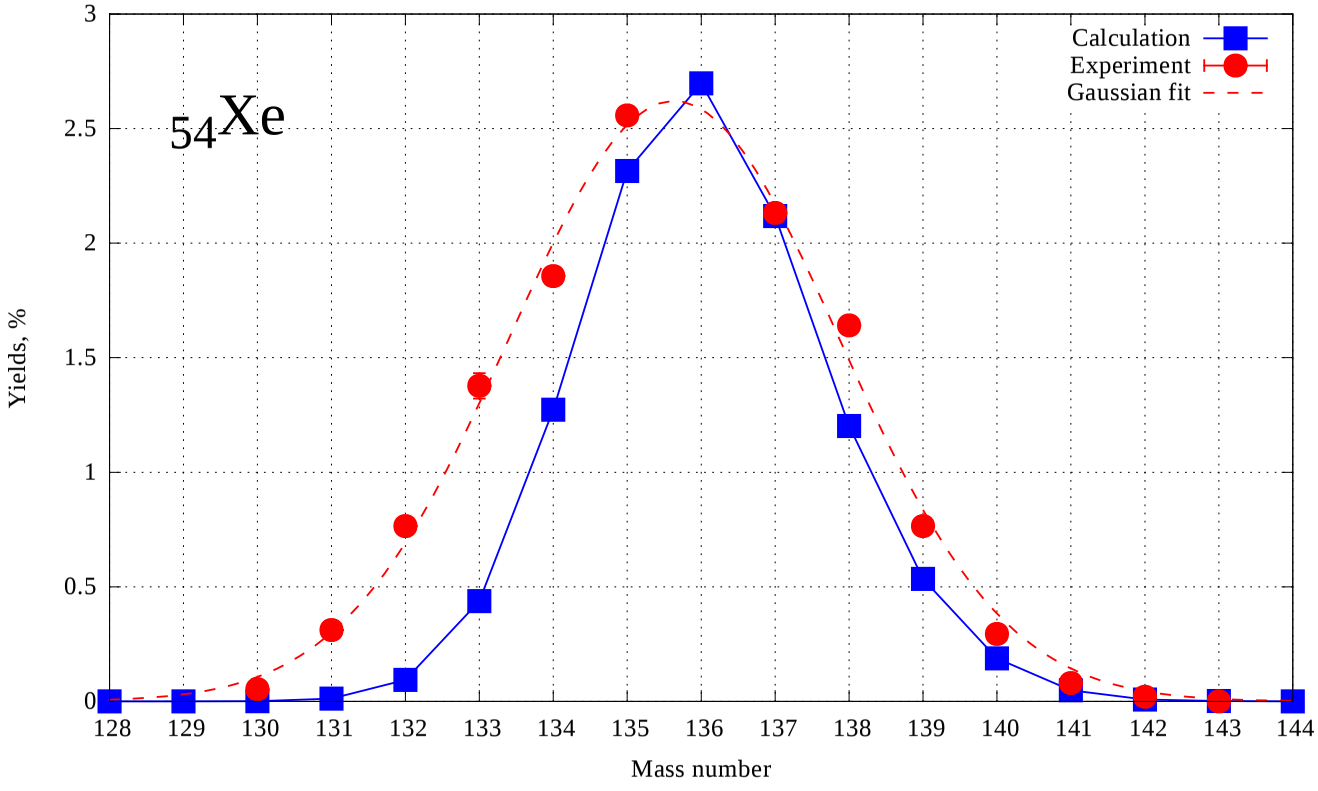

Figure 5.24: Independent yields of $_{54}$Xe.

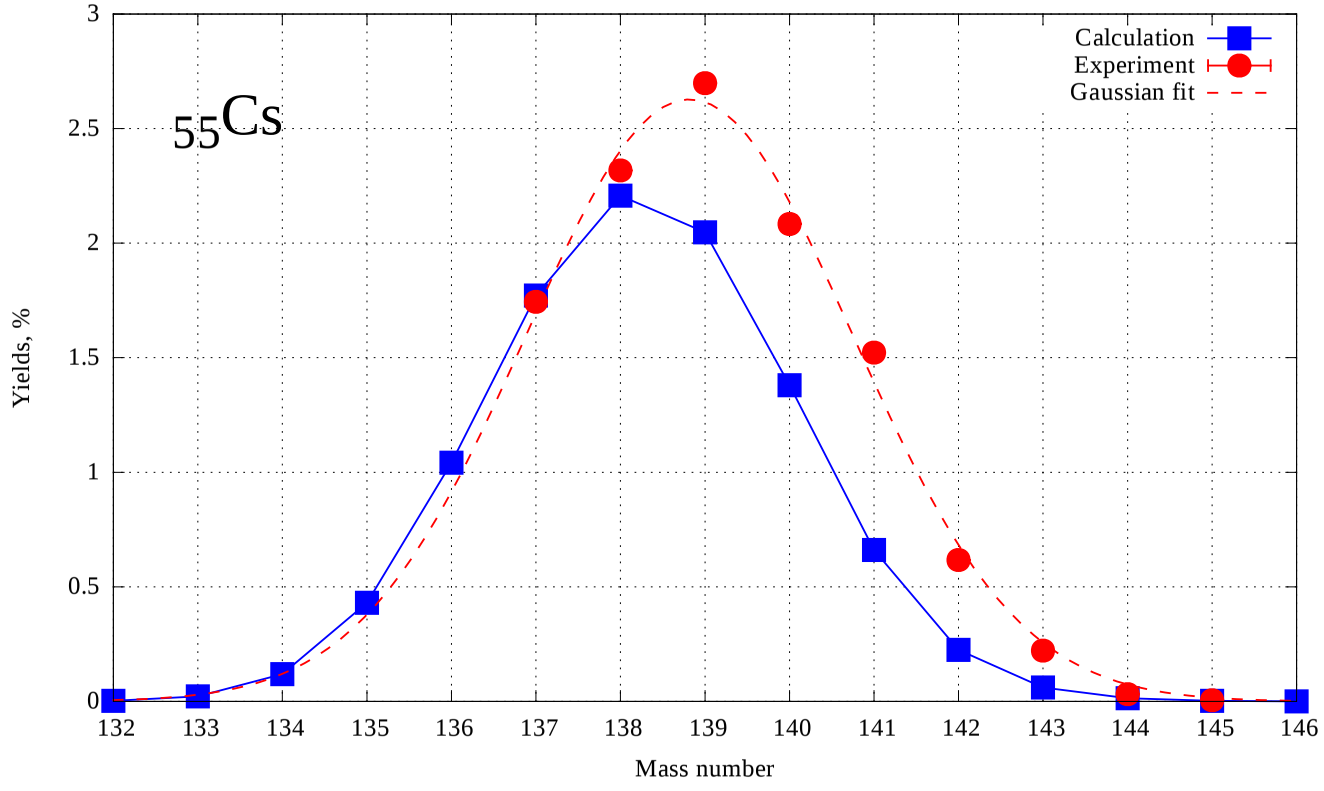

Figure 5.25: Independent yields of $_{55}$Cs.

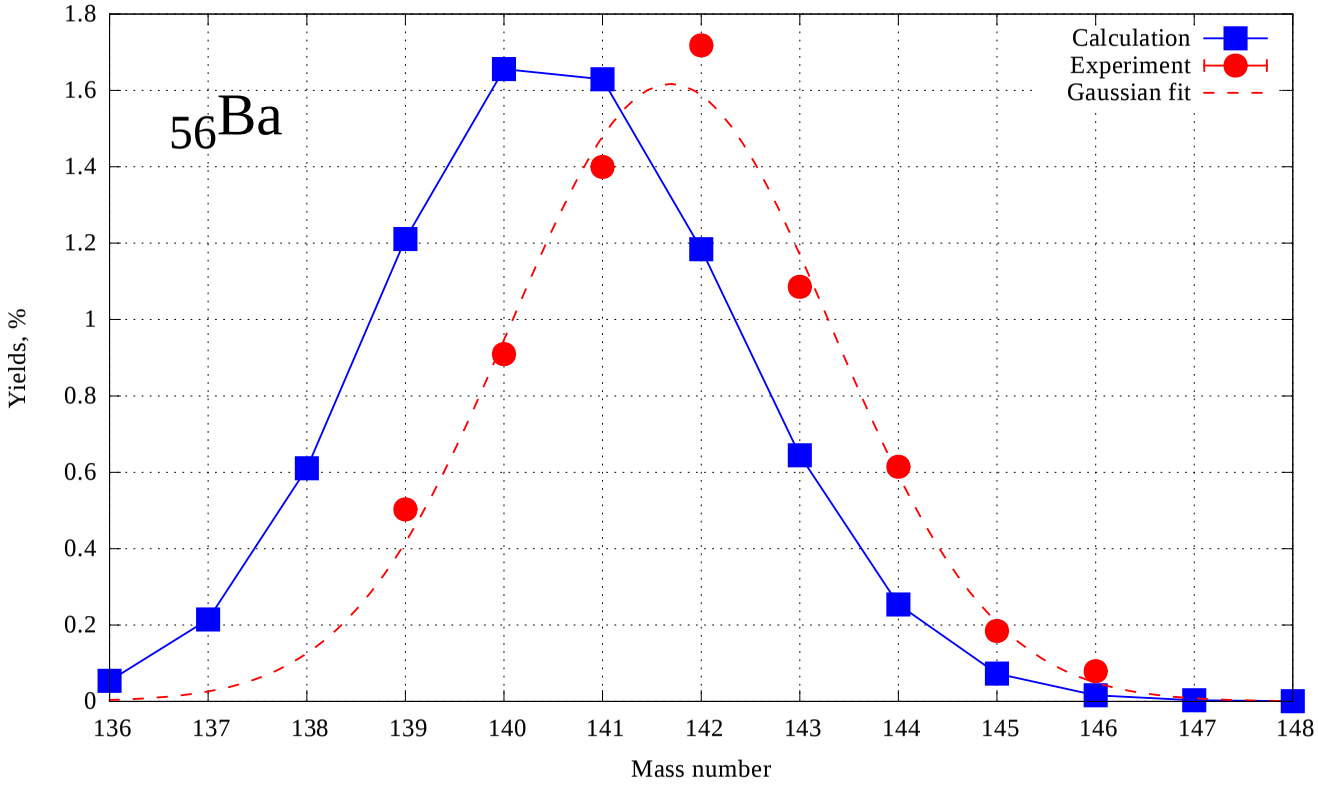

Figure 5.26: Independent yields of $_{56}$Ba.

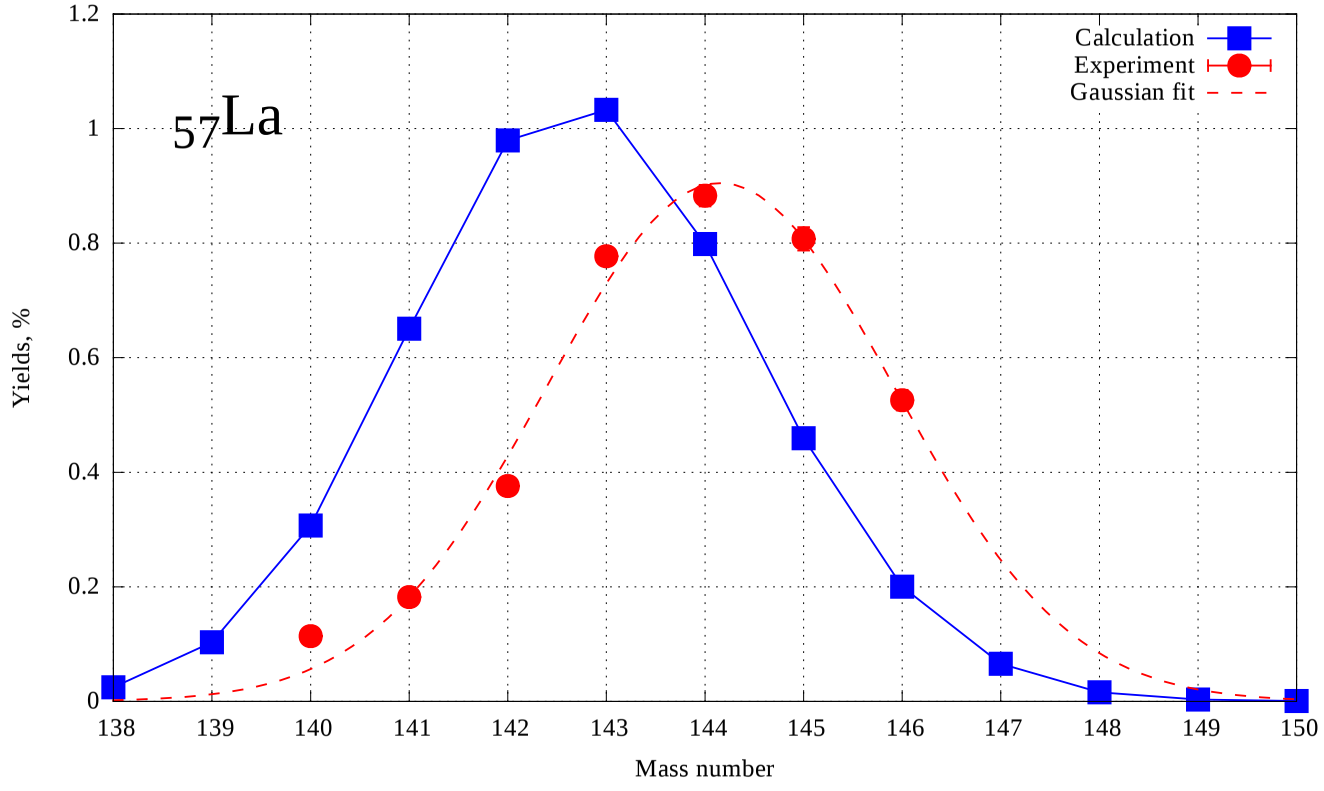

Figure 5.27: Independent yields of $_{57}$La.

Bibliography

[1] O. Hahn, F. Strassmann, Über den Nachweis und das Verhalten der bei der Bestrahlung des Urans mittels Neutronen entstehenden Erdalkalimetalle, Naturwissenschaften 27 (1939) 11. doi:10.1007/BF01488241.

[2] H. G. Graetzer, Discovery of Nuclear Fission, American Jounrnal of Physics 32 (1964) 9. doi:10.1119/1.1970127.

[3] Nobel Media AB 2014, The Nobel Prize in Chemistry 1944 [cited June 2015]. URL http://www.nobelprize.org/nobel_prizes/chemistry/laureates/1944/

[4] Rare Isotope Science Assessment Committee, National Research Council (Ed.), Scientific Opportunities with a RARE-ISOTOPE FACILITY in the United States, The National Academies Press, 500 Fifth Street, N. W., Washington, DC 20001, 2006.

[5] K. A. Petrzhak, G. N. Flerov, Spontaneous nuclear fission, Usp. Fiz. Nauk 73 (1961) 655–683. doi:10.3367/UFNr.0073.196104f.0655.

[6] I. V. Panov, E. Kolbe, B. Pfeiffer, T. Rauscher, K.-L. Kratz, F.-K. Thielemann, Calculations of fission rates for r-process nucleosynthesis, Nucl. Phys. A 747 (2005) 633–654. doi:10.1016/j.nuclphysa.2004.09.115.

[7] G. Martínez-Pinedo, D. Mocelj, N. T. Zinner, A. Kelić, K. Langanke, I. Panov, B. Pfeiffer, T. Rauscher, K.-H. Schmidt, F.-K. Thielemann, The role of fission in the r-process, Prog. in Part. and Nucl. Phys. 59 (2007) 199–205. doi:10.1016/j.ppnp.2007.01.018.

[8] S. Goriely, The fundamental role of fission during r-process nucleosynthesis in neutron stars mergers, Eur. Phys. J. A 51 (2015) 22. doi:10.1140/epja/i2015-15022-3.

[9] L. Meitner, O. R. Frisch, Disintegration of Uranium by Neutrons: a New Type of Nuclear Reaction, Nature 143 (1939) 239–240. doi:10.1038/143239a0.

[10] O. R. Frisch, Physical Evidence for the Division of Heavy Nuclei under Neutron Bombardment, Nature 143 (1939) 276. doi:10.1038/143276a0.

[11] J. Äystö, T. Eronen, A. Jokinen, A. Kankainen, I. D. Moore, H. Penttilä, An IGISOL portrait — Selected contributions, Eur. Phys. J. A 48 (2012) 42. doi:10.1140/epja/i2012-12042-5.

[12] J. Äystö, T. Eronen, A. Jokinen, A. Kankainen, I. D. Moore, H. Penttilä, An IGISOL portrait, Hyperfine Interact 223 (2014) 1–3. doi:10.1007/s10751-013-0872-z.

[13] J. Äystö, Development and applications of the IGISOL technique, Nucl. Phys. A 693 (2001) 477–494. doi:10.1016/S0375-9474(01)00923-X.

[14] I. D. Moore, P. Dendooven, J. Ärje, The IGISOL technique – three decades of developments, Hyper. Int. 223 (2014) 17–62. doi:10.1007/s10751-013-0871-0.

[15] H. Penttilä, J. Äystö, V.-V. Elomaa, T. Eronen, D. Gorelov, U. Hager, J. Hakala, A. Jokinen, A. Kankainen, P. Karvonen, T. Kessler, I. Moore, S. Rahaman, S. Rinta-Antila, V. Rubchenya, T. Sonoda, Independent fission yields with JYFLTRAP, Eur. Phys. J. Special Topics 150 (2007) 317–318. doi:10.1140/epjst/e2007-00335-0.

[16] N. Bohr, J.A.Wheeler, The Mechanism of Nuclear Fission, Phys. Rev. 56 (1939) 426–450. doi:10.1103/PhysRev.56.426.

[17] R. Vandenbosch, J.R.Huizenga, Nuclear Fission, Academic Press, 1973.

[18] C. Wagemans (Ed.), The Nuclear Fission Process, CRC Press, N. W., Boca Raton, Florida 33431, 1991.

[19] W. J. Swiatecki, Deformation Energy of a Charged Drop. II. Symmetric Saddle Point Shapes, Phys. Rev. 104 (1956) 993–1005. doi:10.1103/PhysRev.104.993.

[20] H. A. Bethe, R. F. Bacher, Nuclear Physics A. Stationary States of Nuclei, Rev. Mod. Phys. 8 (1936) 82. doi:10.1103/RevModPhys.8.82.

[21] C. F. v. Weizsacker, Zur Theorie der Kernmassen, Zeit. Phys. 96 (1935) 431–458. doi:10.1007/BF01337700.

[22] J. A. Northrop, R. H. Stokes, K. Boyer, Measurement of the Fission Thresholds of Pu^{239}, U^{233}, U^{235}, and U^{238} Using the (d, p) Reaction, Phys. Rev. 115 (1959) 1277–1286. doi:10.1103/PhysRev.115.1277.

[23] A. I. Obukhov, N. A. Perfilov, Nuclear Fission, Usp. Fiz. Nauk 92 (1967) 621–677.
URL http://ufn.ru/ru/articles/1967/8/c/

[24] K. A. Petrzhak, G. N. Flerov, Spontaneous fission of nuclei, Usp. Fiz. Nauk 25 (1941) 171–178.
URL http://ufn.ru/ru/articles/1941/2/f/

[25] V. M. Strutinsky, Shell Effects in Nuclear Masses and Deformation Energies, Nucl. Phys. A 95 (1967) 420–442. doi:10.1016/0375-9474(67)90510-6.

[26] S. M. Polikanov, V. Druin, V. Karnauhov, V. Mikheev, A. Pleve, N. Skobelev, V. Subbotin, G. Ter-Akopyan, V. Fomichev, Spontaneous Fission with an Anomalously Short Period. I, Sov. Phys. JETP 15 (1962) 1016–1021.

[27] V. P. Perelygin, S. P. Almazova, B. A. Gvozdev, Y. T. Chuburkov, Spontaneous Fission with an Anomalously Short Period. II, Sov. Phys. JETP 15 (1962) 1022–1023.

[28] H.-H. Knitter, U. Brosa, C. Budtz-Jørgensen, Neutron and Gamma Emission in Fission, in: C. Wagemans (Ed.), The Nuclear Fission Process, CRC Press, N. W., Boca Raton, Florida 33431, 1991, pp. 497–543.

[29] A. C. Wahl, Nuclear Charge Distribution in Fission, in: N. Metropolis, D. M. Kerr, G.-C. Rota (Eds.), New Directions in Physics, Academic Press, Orlando, Florida 32887, 1987, pp. 163–189.

[30] F. Gönnenwein, Mass, Charge and Kinetic Energy of Fission Fragments, in: C. Wagemans (Ed.), The Nuclear Fission Process, CRC Press, N. W., Boca Raton, Florida 33431, 1991, pp. 287–473.

[31] A. C. Wahl, R. L. Ferguson, D. R. Nethaway, D. E. Troutner, K. Wolfsberg, Nuclear-Charge Distribution in Low-Energy Fission, Phys. Rev. 126 (1962) 1112–1127. doi:10.1103/PhysRev.126.1112.

[32] E. Weisstein, Sheppard's Correction. From MathWorld–A Wolfram Web Resource. [cited Dec 2015].
URL http://mathworld.wolfram.com/SheppardsCorrection.html

[33] W. Reisdorf, M. de Saint-Simon, L. Remsberg, L. Lessard, C. Thibault, E. Roeckl, R. Klapisch, Analysis of isotopic yield distributions in ^{11}B- and ^{22}Ne-induced fission of ^{238}U, Phys. Rev. C 14 (1976) 2189–2195. doi:10.1103/PhysRevC.14.2189.

[34] S. S. Kapoor, R. Ramanna, P. N. R. Rao, Emission of Prompt Neutrons in the Thermal Neutron Fission of ^{235}U, Phys. Rev. 131 (1963) 283–296. doi:10.1103/PhysRev.131.283.

[35] K. Skavsvåg, K. Bergheim, Energy and Angular Distributions of Prompt Neutrons from Slow Neutron Fission of ^{235}U, Nucl. Phys. A 45 (1963) 72–97. doi:10.1016/0029-5582(63)90785-5.

[36] T. Ethvignot, M. Devlin, H. Duarte, T. Granier, R. C. Haight, B. Morillon, R. O. Nelson, J. M. O'Donnell, D. Rochman, Neutron Multiplicity in the Fission of ^{238}U and ^{235}U with neutrons up to 200 MeV, Phys. Rev. Lett. 94 (2005) 052701. doi:10.1103/PhysRevLett.94.052701.

[37] T. R. England, B. F. Rider, Evaluation and Compilation of Fission Product Yields, 1993. (ENDF-349), Report LA-UR-94-3106.

[38] K.-H. Schmidt, B. Jurado, Entropy Driven Excitation Energy Sorting in Superfluid Fission Dynamics, Phys. Rev. Lett 104 (2010) 212501. doi:10.1103/PhysRevLett.104.212501.

[39] V. A. Rubchenya, Prompt fission neutron emission in neutron and proton induced reactions at intermediate energies, Phys. Rev. C 75 (2007) 054601. doi:10.1103/PhysRevC.75.054601.

[40] V. A. Rubchenya, J. Äystö, Consistent theoretical model for the description of the neutron-rich fission product yields, Eur. Phys. J. A 48 (2012) 44. doi:10.1140/epja/i2012-12044-3.

[41] V. A. Rubchenya, A. V. Kuznetsov, W. H. Trzaska, D. N. Vakhtin, A. A. Alexandrov, I. D. Alkhazov, J. Äystö, S. V. Khlebnikov, V. G. Lyapin, O. I. Osetrov, Y. E. Penionzhkevich, Y. V. Pyatkov, G. P. Tiourin, Fission time scale and viscosity for compound nucleus ^{220}Th formed in reaction ^{40}Ar+^{180}Hf at E_{lab}=180, 190, 216 and 249 MeV, Phys. Rev. C 58 (1998) 1587–1593. doi:10.1103/PhysRevC.58.1587.

[42] M. F. James, R. W. Mills, D. R. Weaver, A new evaluation of fission product yields and the production of a new library (UKFY2) of independent and cumulative yields, Prog. Nucl. Energy 26 (1) (1991) 1–29. doi:10.1016/0149-1970(91)90030-S.

[43] R. W. Mills, Fission product yield evaluation, Ph.D. thesis, School of Physics and Space Research, University of Birmigham (1995).

[44] National Nuclear Data Center, ENDF-6 Formats Manual (October 2012). URL http://www.nndc.bnl.gov/endf/b7.1/endf-manual-vii.1.pdf

[45] N. Otuka, E. Dupont, V. Semkova, B. Pritychenko, A. I. Blokhin, M. Aikawa, S. Babykina, M. Bossant, G. Chen, S. Dunaeva, R. Forrest, T. Fukahori, N. Furutachi, S. Ganesan, Z. Ge, O. O. Gritzay, M. Herman, S. Hlava, K. Katö,

B. Lalremruata, Y. Lee, A. Makinaga, K. Matsumoto, M. Mikhaylyukova, G. Pikulina, V. Pronyaev, A. Saxena, O. Schwerer, S. P. Simakov, N. Soppera, R. Suzuki, S. Takcs, X. Tao, S. Taova, F. Trknyi, V. V. Varlamov, J. Wang, S. C. Yang, V. Zerkin, Y. Zhuang, Towards a More Complete and Accurate Experimental Nuclear Reaction Data Library (EXFOR): International Collaboration Between Nuclear Reaction Data Centres (NRDC), Nuclear Data Sheets 120 (2014) 272 – 276. doi:10.1016/j.nds.2014.07.065.
URL http://www-nds.iaea.org/exfor/

[46] M. Lammer, Compilation and evaluation of fission yield nuclear data, Final report of a co-ordinated research project 1991–1996, IAEA-TECDOC-1168.
URL http://www-pub.iaea.org/MTCD/Publications/PDF/te_1168_prn.pdf

[47] A. C. Wahl, Systematic Trends in Fission Yields, Fission product nuclear data Rep. NEA/NSC/DOC (92)9 (OECD) (1992) 334–345.
URL https://www.oecd-nea.org/science/docs/1992/nsc-doc92-9.pdf

[48] P. Van Duppen, Isotope Separation On Line and Post Acceleration, Lecture Notes in Physics 700 (2006) 37–77. doi:10.1007/3-540-33787-3_2.

[49] H. L. Ravn, B. W. Allardyce, On-Line Mass Separators, Treatise on Heavy-Ion Science 8 (1989) 363–439.

[50] G. R. Choppin, J. R. Meriwether, J. D. Fox, Low-Energy Charged-Particle-Induced Fission, Phys. Rev. 131 (1963) 2149–2152. doi:10.1103/PhysRev.131.2149.

[51] S. H. Freid, J. L. Anderson, G. R. Choppin, Charge Distribution in the Fission of ^{232}Th, J. Inorg. Nucl. Chem. 30 (1968) 3155. doi:10.1016/0022-1902(68)80107-1.

[52] D. G. Madland, J. R. Nix, New Calculation of Prompt Fission Neutron Spectra and Average Prompt Neutron Multiplicities, Nucl. Sci. Eng. 81 (1982) 213–271. doi:10.13182/NSE82-5.

[53] J. Hakala, et al., Precision Mass Measurements beyond ^{132}Sn: Anomalous Behavior of Odd–Even Staggering of Binding Energies, Phys. Rev. Lett. 109 (2012) 032501. doi:10.1103/PhysRevLett.109.032501.

[54] G. Audi, F. G. Kondev, M. Wang, B. Pfeiffer, X. Sun, J. Blackot, M. MacCormick, The Nubase2012 evaluation of nuclear properties, Chinese Phys. C 36 (2012) 1157 – 1286. doi:10.1088/1674-1137/36/12/001.

[55] G. Lhersonneau, P. Dendooven, G. Canchel, J. Huikari, P. Jardin, A. Jokinen, V. Kolhinen, C. Lau, L. Lebreton, A. C. Mueller, A. Nieminen, S. Nummela, H. Penttilä, K. Peräjärvi, Z. Radivojevic, V. Rubchenya, M.-G. Saint-Laurent, W. H. Trzaska, D. Vakhtin, J. Vervier, A. C. C. Villari, J. C. Wang, J. Äystö, Production of neutron–rich isotopes in fission of uranium induced by neutrons of 20 MeV average energy, Eur. Phys. J A 9 (2000) 385–396. doi:10.1007/s100500070023.

[56] A. Al-Adili, K. Jansson, M. Lantz, A. Solders, D. Gorelov, C. Gustavsson, A. Mattera, I. Moore, A. V. Prokofiev, V. Rakopoulos, H. Penttilä, D. Tarrio, S. Wiberg, M. Österlund, S. Pomp, Simulation of the fission–product stopping efficiency in the IGISOL ion guide, Eur. Phys. J. A 51 (2015) 59. doi:10.1140/epja/i2015-15059-2.

[57] Cyclotron MCC30/15 at JYFL [cited Jun 2015].
URL https://www.jyu.fi/fysiikka/en/research/accelerator/accelerator/index_html/mcc30

[58] G. Savard, S. Baker, C. Davids, A. F. Levand, E. F. Moore, R. C. Pardo, R. Vondrasek, B. J. Zabransky, G. Zinkann, Radioactive beams from gas catchers: The CARIBU facility, Nucl. Instr. and Meth. B 266 (2008) 4086–4091. doi:10.1016/j.nimb.2008.05.091.

[59] M. Ranjan, P. Dendooven, S. Purushothaman, T. Dickel, M. Reiter, S. Ayet, E. Haettner, I. Moore, N. Kalantar-Nayestanaki, H. Geissel, W. R. Plaß, D. Schäfer, C. Scheidenberger, F. Schreuder, H. Timersmaa, J. Van de Walle, H. Weick, Design, construction and cooling system performance of a prototype cryogenic stopping cell for the Super-FRS at FAIR, Nucl. Instr. and Meth. A 770 (2015) 87–97. doi:10.1016/j.nima.2014.09.075.

[60] H. Penttilä, P. Karvonen, T. Eronen, V.-V. Elomaa, U. Hager, J. Hakala, I. D. Moore, K. Peräjärvi, S. Rahaman, S. Rinta-Antila, V. Rubchenya, J. Äystö, Determining isotopic distributions of fission products with a penning trap, Eur. Phys. J. A 44 (2010) 147–168. doi:10.1140/epja/i2010-10936-8.

[61] H. Penttilä, V.-V. Elomaa, T. Eronen, J. Hakala, A. Jokinen, A. Kankainen, I. D. Moore, S. Rahaman, S. Rinta-Antila, J. Rissanen, V. Rubchenya, A. Saastamoinen, C. Weber, J. Äystö, Fission yield studies at the IGISOL facility, Eur. Phys. J. A 48 (2012) 43. doi:10.1140/epja/i2012-12043-4.

[62] H. Penttilä, D. Gorelov, P. Karvonen, V.-V. Elomaa, T. Eronen, J. Hakala, A. Jokinen, A. Kankainen, I. D. Moore, J. Parkkonen, S. Rahaman, S. Rinta-Antila, J. Rissanen, V. Rubchenya, T. Sonoda, J. Äystö, M. Lantz, A. Mattera, V. D. Simutkin, S. Pomp, I. Ryzhov, Independent Isotopic Product Yields in

25 MeV and 50 MeV Charged Particle Induced Fission of ^{238}U and ^{232}Th, Nuclear Data Sheets 119 (2014) 334–337. doi:10.1016/j.nds.2014.08.092.

[63] F. Gönnenwein, Recent Developments of Experimental Techniques, Nucl. Phys. A 502 (1989) 159–176. doi:10.1016/0375-9474(89)90660-X.

[64] H. Denschlag, Independent Fission Yield Measurements, Nucl. Sci. and Eng. 94 (1986) 337–352.
URL http://www.ans.org/pubs/journals/nse/a_18345

[65] H. Denschlag, Status of Independent Yield Measurements, J. Radioanal. and Nucl. Chem. 203 (1996) 319–329. doi:10.1007/BF02041515.

[66] G. Herrmann, H. O. Denschlag, Rapid chemical separations, Ann. Rev. Nucl. Sci. 19 (1969) 1–32. doi:10.1146/annurev.ns.19.120169.000245.

[67] G. Herrmann, N. Trautmann, Rapid chemical methods for identification and study of short-lived nuclides, Ann. Rev. Nucl. Part. Sci. 32 (1982) 117–147. doi:10.1146/annurev.ns.32.120182.001001.

[68] K. Rengan, R. A. Meyer, Ultrafast chemical separations, National Academies Press, Washington, DC 20001, 1993.

[69] E. Segre, R. S. Halford, G. T. Seaborg, Chemical Separation of Nuclear Isomers, Phys. Rev. 55 (1939) 321–322. doi:10.1103/PhysRev.55.321.

[70] B. Tracy, J. Chaumont, R. Klapisch, J. Nitschke, A. Poskanzer, E. Roeckl, C. Thibault, Rb and Cs Isotopic Cross Sections from 40–50-MeV-Proton Fission of ^{238}U, ^{232}Th and ^{235}U, Phys. Rev. C 5 (1972) 222–234.

[71] K. Chan, B. Pathak, L. Nikkinen, L. Lessard, I. Grant, Independent yields of indium and gallium in the proton induced fission of natural uranium, J. Inorg. and Nucl. Chem. 39 (1977) 1915–1919. doi:10.1016/0022-1902(77)80516-2.

[72] B. Fogelberg, M. Hellström, L. Jacobsson, D. Jerrestam, L. Spanier, G. Rudstam, Efficiency and delay of the integrated target-ion source of OSIRIS, Nucl. Instr. and Meth. B 70 (1) (1992) 137–141. doi:10.1016/0168-583X(92)95921-D.

[73] G. Rudstam, The determination of nuclear reaction yields by means of an isotope-separator-on-line (ISOL) system, Nucl. Instr. and Meth. A 256 (3) (1987) 465–483. doi:10.1016/0168-9002(87)90290-7.

[74] J. Galy, B. Fogelberg, F. Storrer, H. Mach, Yields of products from fast neutron-induced fission of ^{233}U measured by means of an Isotope Separator On-Line (ISOL) system, European Physical Journal A 8 (3) (2000) 331–354. doi:10.1007/s100500070086.

[75] G. Diiorio, B. Wehring, HIAWATHA, a fission-fragment recoil mass spectrometer, Nucl. Instr. and Meth. 147 (3) (1977) 487–499. doi:10.1016/0029-554X(77)90392-5.

[76] P. Armbruster, M. Asghar, J. Bocquet, R. Decker, H. Ewald, J. Greif, E. Moll, B. Pfeiffer, H. Schrader, F. Schussler, G. Siegert, H. Wollnik, The recoil separator Lohengrin: Performance and special features for experiments, Nucl. Instr. and Meth. 139 (1976) 213 – 222. doi:10.1016/0029-554X(76)90677-7.

[77] O. Serot, C. Amouroux, A. Bidaud, N. Capellan, S. Chabod, A. Ebran, H. Faust, G. Kessedjian, U. Kester, A. Letourneau, O. Litaize, F. Martin, T. Materna, L. Mathieu, S. Panebianco, J.-M. Regis, M. Rudigier, C. Sage, W. Urban, Recent Results from Lohengrin on Fission Yields and Related Decay Properties, Nuclear Data Sheets 119 (2014) 320–323. doi:10.1016/j.nds.2014.08.088.

[78] A. Oed, P. Geltenbort, R. Brissot, F. Göennenwein, P. Perrin, E. Aker, D. Engelhardt, Mass spectrometer for fission fragments based on time-of-flight and energy measurements, Nucl. Instr. and Meth. 219 (3) (1984) 569–574. doi:10.1016/0167-5087(84)90232-1.

[79] D. Dore, F. Farget, F.-R. Lecolley, G. Lehaut, T. Materna, J. Pancin, S. Panebianco, T. Papaevangelou, FALSTAFF: A new tool for fission studies, EPJ Web of Conferences 62 (2013) 05005. doi:10.1051/epjconf/20136205005.

[80] F. Tovesson, C. Arnold, R. Blakeley, A. Hecht, A. Laptev, D. Mader, K. Meierbachtol, L. Snyder, M. White, Spider: A new instrument for fission fragment research at the los alamos neutron science center, EPJ Web of Conferences 62 (2013) 05002. doi:10.1051/epjconf/20136205002.

[81] C. Arnold, F. Tovesson, K. Meierbachtol, T. Bredeweg, M. Jandel, H. Jorgenson, A. Laptev, G. Rusev, D. Shields, M. White, R. Blakeley, D. Mader, A. Hecht, Development of position-sensitive time-of-flight spectrometer for fission fragment research, Nucl. Instr. and Meth. A 764 (2014) 53–58. doi:10.1016/j.nima.2014.07.001.

[82] K. Meierbachtol, F. Tovesson, D. Shields, C. Arnold, R. Blakeley, T. Bredeweg, M. Devlin, A. Hecht, L. Heffern, J. Jorgenson, A. Laptev, D. Mader, J. ODonnell, A. Sierk, M. White, The {SPIDER} fission fragment spectrometer for fission product yield measurements, Nuclear Instruments and Methods in Physics Research Section A: Accelerators, Spectrometers, Detectors and Associated Equipment 788 (2015) 59 – 66. doi:10.1016/j.nima.2015.02.032.

[83] J. Matarraz, I. Tsekhanovich, A. Smith, J. Dare, L. Murray, A. Pollitt, T. Soldner, U. Koster, D. Biswas, A multiparameter nuclear-fission experiment: can all be obtained at once?, Phys. Proc. 47 (2013) 76–81. doi:10.1016/j.phpro.2013.06.012.

[84] M. Fregeau, S. Oberstedt, The Fission-Fragment Spectrometer VERDI, Phys. Proc. 64 (2015) 197–203. doi:10.1016/j.phpro.2015.04.027.

[85] K.-H. Schmidt, A. Heinz, H.-G. Clerc, B. Blank, T. Brohm, S. Czajkowski, C. Donzaud, H. Geissel, E. Hanelt, H. Irnich, M. Itkis, M. de Jong, A. Junghans, A. Magel, G. Münzenberg, F. Nickel, M. Pfützner, A. Piechaczek, C. Röhl, C. Scheidenberger, W. Schwab, S. Steinhäuser, K. Sümmerer, W. Trinder, B. Voss, S. Zhdanov, Low-energy fission studies of neutron-deficient projectile fragments of 238u, Physics Letters B 325 (34) (1994) 313–316. doi:10.1016/0370-2693(94)90017-5.

[86] K.-H. Schmidt, S. Steinhäuser, C. Böckstiegel, A. Grewe, A. Heinz, A. Junghans, J. Benlliure, H.-G. Clerc, M. de Jong, J. Müller, M. Pfützner, B. Voss, Relativistic radioactive beams: A new access to nuclear-fission studies, Nuclear Physics A 665 (34) (2000) 221–267. doi:10.1016/S0375-9474(99)00384-X.

[87] C. Böckstiegel, S. Steinhäuser, K.-H. Schmidt, H.-G. Clerc, A. Grewe, A. Heinz, M. de Jong, A. Junghans, J. Müller, B. Voss, Nuclear-fission studies with relativistic secondary beams: Analysis of fission channels, Nuclear Physics A 802 (1–4) (2008) 12–25. doi:10.1016/j.nuclphysa.2008.01.012.

[88] E. Pellereau, G. Belier, G. Boutoux, A. Chatillon, A. Ebran, T. Gorbinet, B. Laurent, J.-F. Martin, J. Taieb, L. Audouin, L. Tassan-Got, B. Jurado, H. Alvarez-Pol, Y. Ayyad, J. Benlliure, M. Caamaño, D. Cortina-Gil, B. Fernandez-Dominguez, C. Paradela, J. Rodriguez-Sanchez, J. Vargas, E. Casarejos, A. Heinz, A. Kelic-Heil, N. Kurz, C. Nociforo, S. Pietri, A. Prochazka, D. Rossi, K.-H. Schmidt, H. Simon, B. Voss, H. Weick, J. Winfield, SOFIA: An innovative setup to measure complete isotopic yield of fission fragments, EPJ Web of Conferences 62 (2013) 06005. doi:10.1051/epjconf/20136206005.

[89] J. Rodríguez-Sánchez, J. Benlliure, J. Taieb, H. Álvarez-Pol, L. Audouin, Y. Ayyad, G. Bélier, G. Boutoux, E. Casarejos, A. Chatillon, D. Cortina-Gil, T. Gorbinet, A. Heinz, A. Kelić-Heil, N. Kurz, B. Laurent, J.-F. Martin, C. Paradela, E. Pellereau, B. Pietras, A. Prochazka, D. Ramos, C. Rodríguez-Tajes, D. Rossi, H. Simon, L. Tassan-Got, J. Vargas, B. Voss, Fission of highly excited nuclei investigated in complete kinematic measurements, EPJ Web of Conferences 62 (2013) 07009. doi:10.1051/epjconf/20136207009.

[90] H. Savajols, VAMOS: A variable mode high acceptance spectrometer for identifying reaction products induced by SPIRAL beams, Nucl. Instr. and Meth. B 204 (2003) 146–153. doi:10.1016/So168-583X(02)01908-0.

[91] Y. Shimizu, T. Kobayashi, T. Kubo, N. Chiga, T. Isobe, T. Kawabata, Y. Kondo, K. Kusaka, Y. Matsuda, T. Motobayashi, T. Murakami, T. Nakamura, J. Ohnishi, T. Ohnishi, H. Okuno, H. Otsu, H. Sakurai, H. Sato, Y. Satou, K. Sekiguchi, Y. Togano, K. Yoneda, Samurai project at ribf, Journal of Physics: Conference Series 312 (5) (2011) 052022. doi:10.1088/1742-6596/312/5/052022.

[92] T. Kobayashi, N. Chiga, T. Isobe, Y. Kondo, T. Kubo, K. Kusaka, T. Motobayashi, T. Nakamura, J. Ohnishi, H. Okuno, H. Otsu, T. Sako, H. Sato, Y. Shimizu, K. Sekiguchi, K. Takahashi, R. Tanaka, K. Yoneda, {SAMURAI} spectrometer for {RI} beam experiments, Nucl. Instr. and Meth. B 317 (2013) 294–304. doi:10.1016/j.nimb.2013.05.089.

[93] M. Caamaño, O. Delaune, F. Farget, X. Derkx, K.-H. Schmidt, L. Audouin, C.-O. Bacri, G. Barreau, J. Benlliure, E. Casarejos, A. Chbihi, B. Fernández-Domínguez, L. Gaudefroy, C. Golabek, B. Jurado, A. Lemasson, A. Navin, M. Rejmund, T. Roger, A. Shrivastava, C. Schmitt, Isotopic yield distributions of transfer- and fusion-induced fission from ^{238}U + ^{12}C reactions in inverse kinematics, Phys. Rev. C 88 (2013) 024605. doi:10.1103/PhysRevC.88.024605.

[94] M. Leino, P. P. Jauho, J. Äystö, P. Decrock, P. Dendooven, K. Eskola, M. Huyse, A. Jokinen, J. M. Parmonen, H. Penttilä, G. Reusen, P. Taskinen, P. Van Duppen, J. Wauters, Independent and cumulative yields of very neutron-rich nuclei in 20 MeV p- and 18–41 MeV d-induced fission of ^{238}U, Phys. Rev. C 44 (1991) 336–344. doi:10.1103/PhysRevC.44.336.

[95] P. P. Jauho, A. Jokinen, M. Leino, J. M. Parmonen, H. Penttilä, K. Eskola, V. A. Rubchenya, J. Äystö, Isotopic product distributions in the near symmetric mass region in proton induced fission of ^{238}U, Phys. Rev. C 49 (1994) 2036–2044. doi:10.1103/PhysRevC.49.2036.

[96] M. Huhta, P. Dendooven, A. Honkanen, G. Lhersonneau, M. Oinonen, H. Penttilä, K. Peräjärvi, V. A. Rubchenya, J. Äystö, Independent yields of neutron-rich nuclei in charged-particle induced fission, Nucl Instr. and Meth. B 126 (1997) 201–204. doi:10.1016/S0168-583X(97)01098-7.

[97] M. Huhta, P. Dendooven, A. Honkanen, A. Jokinen, G. Lhersonneau, M. Oinonen, H. Penttilä, K. Peräjärvi, V. A. Rubchenya, J. Äystö, Superasymmetric fission at intermediate energy and production of neutron-rich nuclei with

$A < 80$, Phys. Lett. B 405 (1997) 230–235. doi:10.1016/S0370-2693(97)00610-2.

[98] V. A. Rubchenya, W. H. Trzaska, D. N. Vakhtin, J. Äystö, P. Dendooven, S. Hankonen, A. Jokinen, Z. Radivojevich, J. C. Wang, I. D. Alkhazov, A. V. Evsenin, S. V. Khlebnikov, A. V. Kuznetsov, V. G. Lyapin, O. I. Osetrov, G. P. Tiourin, A. A. Aleksandrov, Y. E. Penionzhkevich, Neutron and fragment yields in proton-induced fission of ^{238}U at intermediate energies, Nucl. Instr. and Meth. A 463 (2001) 653–662. doi:10.1016/S0168-9002(01)00176-0.

[99] S. Nummela, P. Dendooven, P. Heikkinen, J. Huikari, A. Nieminen, A. Jokinen, S. Rinta-Antila, V. A. Rubchenya, J. Äystö, Wien filter for cooled low-energy radioactive ion beams, Nucl. Instr. and Meth. A 481 (2002) 718–730. doi:10.1016/S0168-9002(01)01362-6.

[100] L. Stroe, G. Lhersonneau, A. Andrighetto, P. Dendooven, J. Huikari, H. Penttilä, K. Peräjärvi, Tecchio, Y. Wang, Production of neutron-rich nuclei in fission induced by neutrons generated by the p+^{13}C reaction at 55 MeV, Eur. Phys. J. A 17 (2003) 57–63. doi:10.1140/epja/i2002-10132-7.

[101] M. Tanikawa, H. Kudo, H. Sunaoshi, M. Wada, T. Shinozuka, M. Fujioka, Isomeric yield ratios of fission products in the system of 24 MeV proton-induced fission of ^{238}U, Z. Phys. A 347 (1993) 53–62. doi:10.1007/BF01301277.

[102] H. Kudo, M. Maruyama, M. Tanikawa, T. Shionzuka, M. Fujioka, Most probable charge of fission products in 24 MeV proton induced fission of ^{238}U, Phys. Rev. C 57 (1998) 178–188. doi:10.1103/PhysRevC.57.178.

[103] S. Goto, D. Kaji, H. Kudo, M. Fujita, T. Shinozuka, M. Fujioka, Isomeric yield ratios of fission products in proton-induced fission of ^{232}Th, J. Rad. and Nucl. Chem. 239 (1999) 109–112. doi:10.1007/BF02349539.

[104] Y. Kudryavtsev, T. E. Cocolios, J. Gentens, M. Huyse, O. Ivanov, D. Pawels, T. Sonoda, P. Van den Bergh, P. V. Duppen, Dual chamber laser ion source at LISOL, Nucl. Instr. and Meth B 267 (2009) 2908–2917. doi:10.1016/j.nimb.2009.06.013.

[105] P. Karvonen, Fission yield studies with SPIG-equipped IGISOL: A novel method for nuclear data measurements, Ph.D. thesis, Department of Physics, University of Jyväskylä (2010).
URL http://www.jyu.fi/static/fysiikka/vaitoskirjat/2010/pasi-karvonen.pdf

[106] H. Penttilä, The layout of the IGISOL 3 facility, Hyperfine Interactions 223 (1–3) (2014) 5–16. doi:10.1007/s10751-012-0607-6.

[107] P. Karvonen, I. D. Moore, T. Sonoda, T. Kessler, H. Penttilä, K. Peräjärvi, P. Ronkanen, J. Äjstö, A sextupole ion beam guide to improve the efficiency and beam quality at IGISOL, Nucl. Instr. and Meth. B. 266 (2008) 4794–4807. doi:10.1016/j.nimb.2008.05.135.

[108] A. Nieminen, J. Huikari, A. Jokinen, J. Äystö, P. Campbell, E. Cochrane, Beam cooler for low-energy radioactive ions, Nucl. Instr. and Meth. A 469 (2) (2001) 244–253. doi:10.1016/S0168-9002(00)00750-6.

[109] V. Kolhinen, Penning trap for isobaric purification of radioactive beams at IGISOL, Ph.D. thesis, Faculty of Mathematics and Science, University of Jyväskyä (2003).

[110] T. Eronen, V. Kolhinen, V.-V. Elomaa, D. Gorelov, U. Hager, J. Hakala, A. Jokinen, A. Kankainen, P. Karvonen, S. Kopecky, I. Moore, H. Penttilä, S. Rahaman, S. Rinta-Antila, J. Rissanen, A. Saastamoinen, J. Szerypo, C. Weber, J. Äystö, JYFLTRAP: a Penning trap for precision mass spectroscopy and isobaric purification, Eur. Phys. J. A 48 (2012) 46. doi:10.1140/epja/i2012-12046-1.

[111] V. Kolhinen, T. Eronen, D. Gorelov, J. Hakala, A. Jokinen, K. Jokiranta, A. Kankainen, M. Koikkalainen, J. Koponen, H. Kulmala, M. Lantz, A. Mattera, I. Moore, H. Penttilä, T. Pikkarainen, I. Pohjalainen, M. Reponen, S. Rahaman, S. Rinta-Antila, J. Rissanen, C. Rodríguez Triguero, K. Rytkönen, A. Saastamoinen, A. Solders, V. Sonnenschein, J. Äystö, Recommissioning of JYFLTRAP at the new IGISOL–4 facility, Nucl. Instr. and Meth. B 317 (2013) 506–509. doi:10.1016/j.nimb.2013.07.050.

[112] L. Brown, G. Gabrielse, Precision spectroscopy of a charged particle in an imperfect Penning trap, Phys. Rev. A 25 (1982) 2423–2425. doi:10.1103/PhysRevA.25.2423.

[113] G. Gabrielse, The true cyclotron frequency for particles and ions in a Penning trap, Int. Jour. of Mass Spec. 279 (2009) 107–112. doi:10.1016/j.ijms.2008.10.015.

[114] G. Savard, S. Becker, H.-J. Kluge, R. Moore, T. Otto, L. Schweikhard, H. Stolzenberg, U. Wiess, A new cooling technique for heavy ions in a Penning trap, Phys. Lett. A 158 (1991) 247–252. doi:10.1016/0375-9601(91)91008-2.

[115] V. Kolhinen, T. Eronen, J. Hakala, A. Jokinen, S. Kopecky, S. Rinta-Antila, J. Szerypo, J. Äystö, Penning trap for isobaric mass separation at IGISOL, Nucl. Instr. and Meth. B 204 (2003) 502–506. doi:10.1016/S0168-583X(02)02121-3.

[116] V. Kolhinen, S. Kopecky, T. Eronen, U. Hager, J. Hakala, J. Huikari, A. Jokinen, A. Nieminen, S. Rinta-Antila, J. Szerypo, J. Äystö, JYFLTRAP: a cylindrical Penning trap for isobaric beam purification at IGISOL, Nucl. Instr. and Meth. A 528 (2004) 776–787. doi:10.1016/j.nima.2004.05.029.

[117] T. Eronen, V.-V. Elomaa, U. Hager, J. Hakala, A. Jokinen, A. Kankainen, S. Rahaman, J. Rissanen, C. Weber, J. Äystö, Preparing isomerically pure beams of short-lived nuclei at JYFLTRAP, Nucl. Instr. and Meth. B 266 (2008) 4527–4531. doi:10.1016/j.nimb.2008.05.076.

[118] H. Penttilä, D. Gorelov, V.-V. Elomaa, T. Eronen, U. Hager, J. Hakala, A. Jokinen, A. Kankainen, P. Karvonen, I. Moore, J. Parkkonen, K. Peräjärvi, S. Rahaman, S. Rinta-Antila, J. Rissanen, V. Rubchenya, A. Saastamoinen, T. Sonoda, C. Weber, J. Äystö, Independent isotopic yields in 25 MeV and 50 MeV proton induced fission of ^{nat}U, submitted to Eur. Phys. J. A.

[119] D. Abriola, A. Sonzogni, Nuclear Data Sheets for A = 96, Nuclear Data Sheets 109 (2008) 2501–2655. doi:10.1016/j.nds.2008.10.002.

[120] J. Blachot, Nuclear Data Sheets for A = 113, Nuclear Data Sheets 111 (6) (2010) 1471–1618. doi:10.1016/j.nds.2010.05.001.

[121] Z. Elekes, J. Timar, Nuclear Data Sheets for A = 128, Nuclear Data Sheets 129 (2015) 191–436. doi:10.1016/j.nds.2015.09.002.

[122] J. Timar, Z. Elekes, B. Singh, Nuclear Data Sheets for A = 129, Nuclear Data Sheets 121 (2014) 143–394. doi:10.1016/j.nds.2014.09.002.

[123] Programme code PYF [cited Dec 2015].
URL http://www.inp.kz/laboratoryrus/lpdpyf.php

[124] D. Gorodisskiy, S. Mulgin, A. Rusanov, S. Zhdanov, Modal approach to the description of fragment mass yields in neutron and proton induced fission of actinides at incident particle energies from 5 to 200 Mev, in: C. Wagemans (Ed.), Fission Product Yield Data for the Transmutation of Minor Actinide Nuclear Waste, International Atomic Energy Agency, Wagramer Strasse 5, P.O. Box 100, 1400 Vienna, Austria, 2008, pp. 183–209.
URL https://www.iaea.org/books/

[125] S. Mulgin, S. Zhdanov, N. Kondratiev, K. Kovalchuk, A. Rusanov, The modal structure of fragment mass and energy yields from the 10.3–30.0 MeV proton induced fission of ^{232}Th and ^{235}U, Nucl. Phys. A 824 (2009) 1–23. doi:10.1016/j.nuclphysa.2009.03.013.

[126] R. Brun, F. Rademakers, ROOT An object oriented data analysis framework, Nucl. Instr. and Meth.A 389 (1–2) (1997) 81–86. doi:10.1016/S0168-9002(97)00048-X.
URL https://root.cern.ch/

[127] I. Antcheva, M. Ballintijn, B. Bellenot, M. Biskup, R. Brun, N. Buncic, P. Canal, D. Casadei, O. Couet, V. Fine, L. Franco, G. Ganis, A. Gheata, D. G. Maline, M. Goto, J. Iwaszkiewicz, A. Kreshuk, D. M. Segura, R. Maunder, L. Moneta, A. Naumann, E. Offermann, V. Onuchin, S. Panacek, F. Rademakers, P. Russo, M. Tadel, ROOT—A C++ framework for petabyte data storage, statistical analysis and visualization, Computer Physics Communications 182 (6) (2011) 1384–1385. doi:10.1016/j.cpc.2011.02.008.

[128] I. D. Moore, T. Eronen, D. Gorelov, J. Hakala, A. Kankainen, V. S. Kolhinen, H. Penttilä, I. Pohjalainen, M. Reponen, J. Rissanen, A. Saastamoinen, S. Rinta-Antila, V. Sonnenschein, J. Äjstö, Towards commissioning the new IGISOL–4 facility, Nucl. Instr. and Meth. B. 317 (2013) 208–213. doi:10.1016/j.nimb.2013.06.036.

[129] J. Chadwick, The Existence of a Neutron, Proc. Roy. Soc. Lond. A. 136 (1932) 692–708. doi:10.1098/rspa.1932.0112.

[130] A. T. Yue, M. S. Dewey, D. M. Gilliam, G. L. Greene, A. B. Laptev, J. S. Nico, W. M. Snow, F. E. Wietfeldt, Improved Determination of the Neutron Lifetime, Phys. Rev. Lett. 111 (2013) 222501. doi:10.1103/PhysRevLett.111.222501.

[131] P. Grand, A. N. Goland, An Intense Neutron Source Based Upon The Deuteron-Stripping Reaction, Nucl. Instr. Meth. 145 (1977) 49–76. doi:10.1016/0029-554X(77)90557-2.

[132] T. Rinckel, D. V. Baxter, J. Doskow, H. Kaiser, R. Pynn, P. E. Sokol, T. Todd, LENS Operating Experience, Phys. Proc. 26 (2012) 161–167. doi:10.1016/j.phpro.2012.03.021.

[133] T. Rinckel, D. V. Baxter, J. Doskow, P. E. Sokol, T. Todd, Target Performance at the Low Energy Neutron Source, Phys. Proc. 26 (2012) 168–177. doi:10.1016/j.phpro.2012.03.022.

[134] J. F. Ziegler, The Stopping and Ranges of Ions in Matter (SRIM) [cited Jun 2015].
URL http://www.srim.org/

[135] M. Matzke, Unfolding Procedures, Rad. Prot. Dos. 107 (2003) 155–174.

[136] M. Matzke, Propagation of Uncertainties in Unfolding Procedures, Nucl. Instr. Meth. A. 476 (2002) 230–241. doi:10.1016/S0168-9002(01)01438-3.

[137] M. A. Lone, C. Bigham, J. Fraser, H. Schneider, T. Alexander, A. Ferguson, A. McDonald, Thick Target Neutron Yields and Spectral Distributions from the ^{7}Li($^{d}_{p}$, n) and ^{9}Be($^{d}_{p}$, n) Reactions, Nucl. Instr. Meth. 143 (1977) 331–344. doi:10.1016/0029-554X(77)90616-4.

[138] M. A. Lone, A. J. Ferguson, B. C. Robertson, Characteristics of Neutrons from Be Target Bombarded with Protons, Deuterons and Alpha Particles, Nucl. Instr. Meth. 189 (1981) 515–523. doi:10.1016/0029-554X(81)90438-9.

[139] University of Jyväskylä, Department of Physics, Accelerators, K130 [cited June 2015].
URL https://www.jyu.fi/fysiikka/en/research/accelerator/accelerator/index_html/accelerator/accelerator/k130/